NOVEL COAXIAL CATHETERS IN PHOTOACOUSTIC ENDOSCOPY

LIN RIQIANG

PhD

The Hong Kong Polytechnic University

2024

The Hong Kong Polytechnic University

Department of Electrical and Electronic Engineering

Novel Coaxial Catheters in Photoacoustic Endoscopy

Lin Riqiang

A thesis submitted in partial fulfilment of the
requirements for the degree of
Doctor of Philosophy

August 2023

CERTIFICATE OF ORIGINALITY

I hereby declare that this thesis is my own work and that, to the best of my knowledge and belief, it reproduces no material previously published or written, nor material that has been accepted for the award of any other degree or diploma, except where due acknowledgement has been made in the text.

_____ _____ (Signed)

Lin Riqiang (Name of student)

Dedication

To my loved

Parents

Lin Huanran & Xu Qiongying

Wife

Yang Danyan

Son

Lin Shengyang

Abstract

Photoacoustic endoscopy (PAE) provides high sensitivity and spatial resolution of morphological information for intravascular (IV) and gastrointestinal (GI) applications. The IVPA catheter can detect the vulnerable plaque, intralipid and inflammation cells in the cardiac vessels; and the GIPA catheter is capable of imaging the vasculature of the rectum and its hemoglobin oxygen saturation. It is significant to improve the imaging efficiency of PAE. This study aims to expand the imaging range of PAE catheters and improve the efficiency of PA imaging, offering novel coaxial designs on both IV and GI endoscopic imaging.

A PZT based ultrasound transducer (UST) is successfully developed with a high center frequency of 35 MHz, a dimension of 0.6 mm × 0.6 mm × 0.4 mm and a center orifice of 0.18 mm. This ring-shaped UST is a key element in the coaxial design, which enables a multimode fiber to get through, forming a long coaxial optical-acoustic overlapped area. Using the proposed coaxial setup, a novel miniature IV-PAE catheter is successfully fabricated with an outer diameter of 0.9 mm. The performance of the ring-shaped UST is tested by the pulse-echo experiment. The resolution of the new design is evaluated by the graphite rods. The IV-PAE catheter is demonstrated by imaging the nano particles in the *ex-vivo* tissue.

To further explore the coaxial design in PAE catheters, transparent piezoelectric

material is applied for developing a transparent ultrasound transducer (TUST). A 2 mm × 2 mm × 0.075 mm lithium niobate (LN) single crystal wafer is used in a miniature PA probe, whose dimension was smaller than the previous LN-based TUSTs in the reported work. A Gradient-index (GRIN) lens is applied as the backing layer of the TUST, effectively shrinking the entire probe size. The proposed probe exhibits a high center frequency of 46.9 MHz and a -6 dB bandwidth of 29.4%. Experiments are further performed on the phantoms to demonstrate the multi-functions of the miniature probe on fluid flow sensing and imaging.

Using the transparent piezoelectric material, a coaxial GI-PAE catheter is developed with a Bessel beam. The diameter of the catheter is 3.5 mm, which is compatible with the 3.7-mm instrumental channel of a conventional clinical optical endoscope. The Bessel beam is formed by a GRIN lens and an axicon, making a long depth of field. The Bessel beam patten is tested by a Charge Coupled Device (CCD) camera. The resolution of the proposed catheter is evaluated by the blade-edge method at different depths, showing its long DOF of ~4.5 mm. The phantom imaging is conducted at different depths to demonstrate the performance of the GI-PAE catheter in a large imaging range.

In short, two novel coaxial PAE catheters are successfully designed and fabricated, both of which provide a large imaging range than the previous works with miniature dimensions. The imaging results successfully support the research goal. The

improvements of imaging range brought by the coaxial configuration greatly enhance the PA imaging efficiency. This research suggests a bright future for both plaque evaluation and GI tumor detection.

List of Publications

SCI journal articles:

1. **Lin, Riqiang**[#]; Lv, Shengmiao[#]; Lou, Wenjing; Wang, Xiatian; Xie, Zhihua; Zeng, Silue; Chen, Rui; Gao, Wen; Jiang, Tianan; Cheng, Eric, Ka Wai; Lam, Kwok-ho* and Gong, Xiaojing*. "*In-vivo* assessment of a rat rectal tumor using optical-resolution photoacoustic endoscopy". *Biomedical Optics Express.* 2024, 15, 2251-2261. (This work involved the preparation of animal model, refering to the future work in Chapter 4.)
2. **Lin, Riqiang**; Zhang, Qi; Lv, Shengmiao; Zhang, Jiaming; Wang, Xiatian; Shi, Dongliang; Gong, Xiaojing* and Lam, Kwok-ho*. "Miniature intravascular photoacoustic endoscopy with coaxial excitation and detection". *Journal of Biophotonics*, 2023, 16(4): e202200269. (Journal Cover Art)

   (This work refers to Chapter 2.)
3. **Lin, Riqiang**; Zhang, Jiaming; Gao, Wen; Wang, Xiatian; Lv, Shengmiao; Lam, Kwok-ho* and Gong, Xiaojing*. "A miniature multi-functional photoacoustic probe". *Micromachines*. 2023, 14, 1269.

   (This work refers to Chapter 3.)
4. Shi, Lu; Li, Ying; Xing, Yi; **Lin, Riqiang**; Cheng, Guanggui; Ding, jianning; Lam, Kwok-ho*. "SiO_x microparticles embedded into 3D wrinkled N, S co-doped multilayer graphene sheets as a high-performance anode for long-life full lithium-ion batteries". *Electrochimica Acta*, 2021, 390: 138841.

5. Zhang, Jiaming; Bao, Guocui; Gao, Wen; **Lin, Riqiang**; Yang, Fan; Kwok-Ho, Lam*. "Miniature ultrasound transducer incorporating Sm-PMN-PT 1-3 composite". *Journal of Composites Science*, 2024,8, 80.
6. Zhang, Jiaming; Long, Xing; Zhang, Guangjie; Ma, Zhongtian; Li, Wenzhao; Wang, Yibing; Yang, Fan; **Lin, Riqiang**; Li, Changhui*; Lam, Kwok-ho*. "Broadband transparent ultrasound transducer with polymethyl methacrylate as matching layer for in vivo photoacoustic microscopy". *Photoacoustics*, 2023, 100548.
7. **Lin, Riqiang**; Xie, Zhihua; Wang, Xiatian; Gao, Wen, Cheng, Eric, Ka Wai; Lam, Kwok-ho* and Gong, Xiaojing*. "Optical-resolution photoacoustic endoscopy based on Bessel beam and transparent ultrasound transducer". (*Journal of Biophotonics*, In preparation)

   (This work refers to Chapter 4.)

   *Corresponding authors. #Equral contribution.

Patents:

1. Lam, Kwok-ho, **Lin, Riqiang** and Shi, Dongliang "Transparent ultrasound transducer with light beam shaping and the method for assembling the same". U.S. Patent No. U.S. 11609326, Mar 2023: H.K. Patent No. 40079040A.
2. Lam, Kwok-ho and **Lin, Riqiang.** "超声换能器组件、探头、系统和制造方法 (Ultrasound transducer assembly, probe, endoscopy system and manufacturing method)". China Patent. No. ZL 202011176786.4.g.

3. Lam, Kwok-ho and **Lin, Riqiang.** "Ultrasound transducer assembly, probe, endoscopy system and manufacturing method". U.S Patent. Application No. U.S. 0133262 A1. May 2022.

International conference presentations:

1. **Lin, Riqiang**; Lv, Shengmiao; Lam, Kwok-ho; Gong, Xiaojing. "Optical-resolution photoacoustic endoscopy on in vivo rat rectum tumor", *2023 The 16th International Conference on Photonics and Imaging in Biology and Medicine* (Oral. Haikou, China)
2. **Lin, Riqiang**; Gong, Xiaojing; Lam, Kwok-ho. "Optical resolution photoacoustic endoscopy on rat rectal tumor in vivo", *2023 IEEE International Ultrasonics Symposium* (Poster. Montreal, Canada)
3. **Lin, Riqiang**; Zhang, Jiaming; Wang, Xiatian; Gong, Xiaojing; Lam, Kwok-ho. "Compact optical-resolution photoacoustic microscopy using transparent ultrasound transducer", *2022 IEEE International Ultrasonics Symposium* (Oral. Venice, Italy)
4. **Lin, Riqiang**; Gong, Xiaojing; Lam, Kwok-ho. "Intravascular photoacoustic endoscopy with coaxial excitation and detection", *2021 IEEE International Ultrasonics Symposium* (Poster. Online)
5. **Lin, Riqiang**; Gong, Xiaojing; Lam, Kwok-ho. "A miniature coaxial catheter for intravascular photoacoustic endoscopy", *2021 The 15th International Conference on Photonics and Imaging in Biology and Medicine* (Oral. Haikou, China)

Acknowledgements

I would also like to express my sincere gratitude to my supervisors Professor Lam Kwok-Ho and Professor Cheng Eric Ka-Wai for their support, guidance and mentoring during my Ph.D. study at the Hong Kong Polytechnic University. I learned a lot from them not only their expertise but also the good academic attitude. Doing research in campus is the most pleasant experience in my memory. I am lucky to be one of the members in the research lab.

I am heartily thankful to Professor Gong Xiaojing, who is my project supervisor in collaboration. Without Professor Gong's support and suggestion, I would not able to finish the study.

I would like to thank all my colleagues and friends in the lab, especially Dr. Zhang Qi, who taught me the methods of ultrasound transducer fabrication when I was a green hand in the lab. Special thanks to Dr. Shi Dongliang, Dr. Xie Zhihua, Mr. Wang Xiatian, Mr. Zhang Jiaming and Mr. Lv Shengmiao, who helped me a lot on conducting imaging experiments. I thank Dr. Li Ying, Mr. Zhang Xingyu, Mr. Yang Fan and Miss Bao Guocui. It was a great pleasure to study with them.

Last but not least, I would like to express my deepest gratitude to my parents, my wife and my son, who are always giving me the most unconditional love and support.

Table of contents

List of Figure Captions

List of Table Captions

List of Abbreviations

3D	**Three-Dimensional**
ANSI	**American National Standards Institute**
ATLOs	**Adventitial Tertiary Lymphatic Organs**
AR-PAM	**Acoustic Resolution Photoacoustic Microscopy**
BW	**Bandwidth**
CCD	**Charge Coupled Device**
CuS	**Copper Sulfide**
CTC	**Circulating Tumor Cells**
CTO	**Chronic Total Occlusion**
DAQ	**Data Acquisition**
DOF	**Depth-of-Field**
ESF	**Edge Spread Function**
EUS	**Endoscopic Ultrasound**
FDA	**Food and Drug Administration**
FFT	**Fast Fourier Transform**
FWHM	**Full Width at Half Maximum**

GI	**Gastrointestinal**
GRIN	**Gradient-index**
ICG	**Indocyanine Green**
IV	**Intravascular**
ITO	**Indium Tin Oxide**
LN	**Lithium Niobate**
LSF	**Line Spread Function**
MAP	**Maximal Amplitude Projection**
NA	**Numerical Aperture**
NIR	**Near Infrared**
OCT	**Optical Coherence Tomograph**
OR-PAM	**Optical Resolution Photoacoustic Microscopy**
PACT	**Photoacoustic Computed Tomography**
PAE	**Photoacoustic Endoscopy/Endoscopic**
PAI	**Photoacoustic Imaging**
PAM	**Photoacoustic Microscopy**
PE	**Polyethylene**
PMN-PT	**Lead Indium Niobate-Lead Magnesium Niobate-Lead**

	Titanate
PZT	**Lead Zirconate Titanate**
SNR	**Signal-to-Noise Ratio**
TUST	**Transparent Ultrasonic Transducer**
US	**Ultrasound**
UST	**Ultrasonic Transducer**
USI	**Ultrasound Imaging**

List of SI Units

cm	**centimeter**
°C	**Celsius degree**
dB	**decibel**
g	**gram**
Hz	**hertz**
L/g·cm^{-1}	**liter per gram per centimeter**
J/cm^2	**joule per square centimeter**
m	**meter**
MHz	**megahertz**
mL	**milliliter**
mJ/cm^2	**millijoule per square centimeter**
mm	**millimeter**
mV	**milli-volt**
nm	**nanometer**
Ω	**ohm**
Pa	**pascal**

s	**second**
µg/mL	**microgram per milliliter**
µm	**micrometer**
V	**volt**

List of Symbols

Symbol	Description	SI Unit
c	Sound speed	m/s
d	Piezoelectric strain coefficient	C/N
d_{33}	Piezoelectric strain constant	C/N
F	Local optical fluence	J/cm^2
f	Frequency	Hz
f_a	Anti-resonant frequency	MHz
f_r	Resonant frequency	MHz
k_{eff}	Effective electromechanical coupling coefficient	---
k_t	Electromechanical coupling coefficient	---
p_0	Acoustic pressure	Pa
T_c	Cuire Temperature	℃
T_0	Temperature	℃
Γ	Grueneisen	---
η_{th}	Percentage of absorbed optical energy	---
μ_a	Absorption coefficient	cm^{-1}

C_{v}	Coefficient of variation	---
σ	Standard deviation	---
μ	Average number	---
Z	Acoustic impedance	MRayl

Chapter 1 Introduction

1.1 Research Background

As a non-invasive or minimally invasive imaging tool, endoscopy[1-3] is capable of entering the human body and imaging the ill tissues closely, offering detailed morphological and functional information superior to *in-intro* imaging. There are a number of imaging modalities of clinical endoscopy, such as white light[4], narrow band[5], fluorescence[6], optical coherence tomography (OCT)[7] and ultrasound (US)[3, 8]. Different imaging modalities provide specific information of the human body. White light endoscopy functions as a camera[4], imaging superficial morphology of the tissue. Narrow band imaging[5] enhances visualization of tissue vasculature. Fluorescence imaging[6] has a very high sensitivity to image the targeted probe. OCT[7] achieves micrometer-level imaging resolution, while US imaging offers centimeter-level imaging depth for observing vessel[3], organ[9] or tumor[8] structures.

As the human tissue is complicated in terms of composition and geometry, a single imaging modality is not sufficient for comprehensive clinical diagnosis[10, 11]. Optical imaging excels in high resolution but lacks depth penetration, while US imaging provides good depth but suffers from poor contrast[12]. Thus, a growing trend involves combining multiple modalities into a single endoscopic catheter, offering various tissue parameters across various dimensions.

Photoacoustic endoscopy[13] (PAE) represents a cutting-edge technology developed in recent decades, integrating the strengths of both optical and US imaging methods. The innovative technology offers much more information compared to conventional imaging tools, whether applied in cardiovascular vessels[14-16] or the gastrointestinal (GI) tract[17, 18]. For example, the intravascular PAE (IV-PAE) catheter can see lipid of atheromatous plaque without the need for contrast agent[15], while the GI-PAE catheter facilitates the visualization of 3D rectal vasculature with a 10-μm resolution, alongside the ability to determine blood oxygen saturation[18, 19].

However, the performance of the PAE catheter is affected by the size limitation in accommodating miniature optical or acoustic elements. Most of the catheters were designed with non-coaxial configurations, featuring oblique illumination and side-view detection [11, 20], or oblique detection and side-illumination[21]. To minimize the size of the catheter, these designs aligned all the optical and acoustic elements in a line but the catheters result in a limited overlap area for imaging. To solve the issue, the PAE catheter with coaxial excitation and detection is developed, which not only simply reduces the dimensions, but also enhances the application potential by offering more comprehensive and useful information for clinical research.

1.2 Photoacoustic Imaging

1.2.1 Principles and Applications

Photoacoustic imaging[22, 23] (PAI) is an emerging technology based on the photoacoustic effect, in which short-pulsed laser light is used to irradiate the tissue. Upon absorption of laser, the biological tissue undergoes a small temperature rise, inducing a transient thermoelastic expansion and generating wideband ultrasound waves[24]. Based on the principle, the ultrasound waves, termed photoacoustic waves, are detected by a ultrasonic transducer (UST) and used to map the optical absorption distribution of targets. The PAI features high optical contrast and low acoustic scattering, naturally integrating with existing US imaging modalities[25].

With the advanced features, the PAI has been incorporated into various systems tailored to specific applications[26-28]. Its biomedical applications span from cellular[26] to organ-level imaging[29]. With using specific laser wavelengths, PAI enables the imaging and quantitively analysis of corresponding targets[30]. For example, hemoglobin has high absorption at visible wavelengths[24], while lipids have two absorption peaks at the wavelengths of ~1210 nm[31] and ~1720 nm[32], prompting the application of corresponding laser wavelengths for specific target imaging. In addition, employing two laser wavelengths to excite blood vessels allows for the calculation of blood oxygen saturation based on the intensity of the photoacoustic signal[33]. The PAI has demonstrated great potential in biomedical studies. Nevertheless, further improving the

imaging efficiency is desired to acquire much useful information for research and clinical uses.

1.2.2 Methods for Improving the Photoacoustic Imaging (PAI) Efficiency

State-of-the-art methods for the improvement of PAI efficiency generally involve optical irradiation[34], acoustic detection[35] and nanoprobes[28] (Figure 1.1). The photoacoustic signal, also known as the acoustic wave, is generated by the optical absorption of tissue. Its initial acoustic pressure amplitude is expressed as[24]:

$$p_0 = \Gamma \eta_{th} \mu_a F \tag{1.1}$$

where Γ is the Grueneisen parameter[36] that is associated with tissue temperature, η_{th} is the percentage of absorbed optical energy converted into heat through non-radiative relaxation and μ_a is the absorption coefficient, both pertinent to the imaging target, and F is the local optical fluence. Based on the equation, optical enhancement of the PA signal can be achieved by increasing the tissue temperature[37] and/or optical fluence[38]. From the perspective of acoustic detection, more PA signal can be detected by upgrading the UST performance[39] or extending detection range[27, 35]. Furthermore, employing exogenous agent such as nanoprobe[28] can significantly improve the imaging sensitivity.

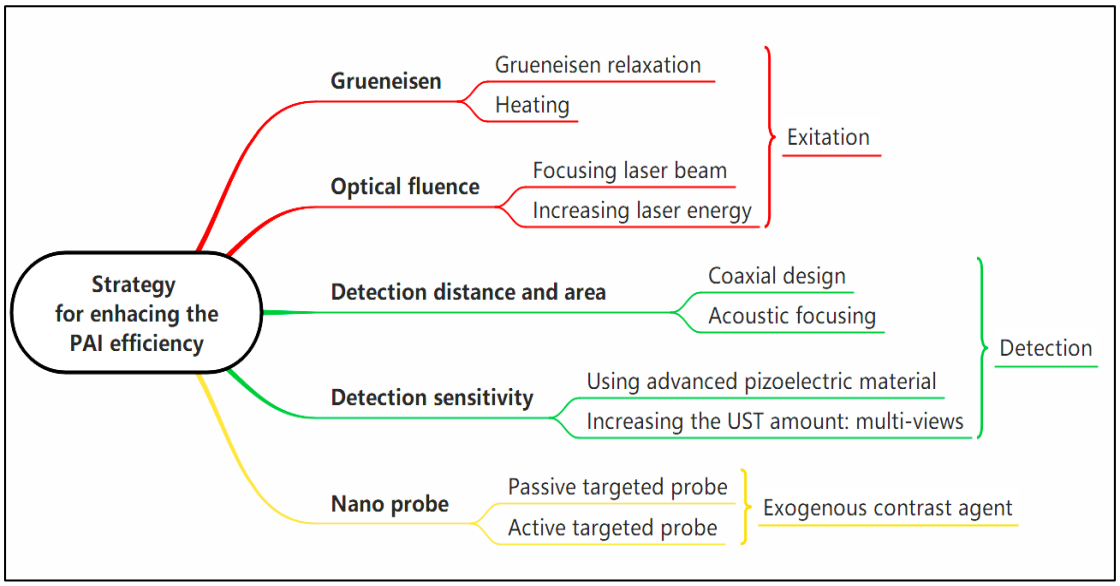

Figure 1.1 Methods for improving the PAI efficiency.

While promising strategies have been reported, many of them are not appropriate for PAI systems especially the PAE one. For example, simply raising the tissue temperature to increase Γ is not an effective method. In water and diluted aqueous solutions, Γ can be estimated by the following empirical formula[40]:

$$\Gamma(T_0) = 0.0043 + 0.0053\,T_0 \tag{1.2}$$

where T_0 is the temperature in degrees Celsius. For the human body, $\Gamma(37\,℃) = 0.2$ so that the efficiency remains low even the body can tolerate the heat of 45 ℃, where $\Gamma(45\,℃) = 0.24$.

The direct increment of optical fluence is a common approach to improve imaging efficiency. According to ANSI standards, the laser energy should be limited within a safe range. Thus, to avoid tissue damage, it is not allowed to arbitrarily increase the optical fluence by increasing the laser energy. Employing an optical lens to focus the laser beam is a popular way, but achieving a small laser spot requires a big numerical

aperture (NA). Such lenses with a big NA usually have bulky dimensions, posing challenges for endoscopy applications.

Improving acoustic detection is an essential way to improve the efficiency of PAI. To collect more PA signals, shortening detection distance and expanding detection angle are common strategies. Specific approaches including coaxial design and acoustic focusing, easily implemented in PAM[41] and PACT[42], but are difficult to achieve in PAE due to the opaque UST and limited space.

Upgrading the UST performance can fundamentally enhance the PAI quality. While PZT ceramics[43] have traditionally been used in PAI systems, recent advancements include the development of PMN-PT single crystal[44] and its 1-3 composite[39] for UST, which show higher sensitivity and wider bandwidth compared to the PZT transducer. Using state-of-the-art piezoelectric materials offers an effective mean to elevate the PA detection sensitivity, but it is not prevalent due to complicated fabrication processes. Another practical way is to increase the number of USTs to cover more irradiated areas[45]. A typical practice is seen in the PACT system[46], employing a bulky US array.

Nanoprobes[47], as an exogenous contrast agent, can target specific cells[48] *in vivo* and significantly improve the PA signal intensity, which have been widely used in PAI. Passive targeted probes, like ICG[49] and Prussian blue[50] – approved by the FDA (USA) - easily accumulate in vessels or tumors due to the lower metabolic rate. Conversely,

active targeted probes are typically designed to meet specific requirements[51], capable of pinpointing the targeted cells. CuS[52] and some gold nanoparticles[53] are commonly used as decorated probes. With ongoing design and synthesis, nanoprobes are playing an important role in advancing PAI.

1.2.3 Coaxial Design in Photoacoustic Imaging (PAI)

As mentioned above, coaxial design stands out as an effective method to improve PAI efficiency. Although Duan et al.[54] recently revealed that when the PA system detects tissue with weak optical absorption (<10 cm^{-1}), coaxial design may not be optimal due to limitations in detection bandwidth and view. In GI-PAE, where the imaging target is blood vessels[55] (hemoglobin) exhibiting strong optical absorption[56, 57] in visible wavelengths, coaxial detection proves ideal. While in IV-PAE, vulnerable plaque[15], featuring intralipid and inflammation cells[58], is the imaging target. The intralipid has an absorption peak (~10 cm^{-1}) at 1720 nm[59, 60](shown in Figure 1.2), while inflammation cells are imaged using the targeted probes. Therefore, coaxial design is applicable in PAE catheters for effective collection of PA signals.

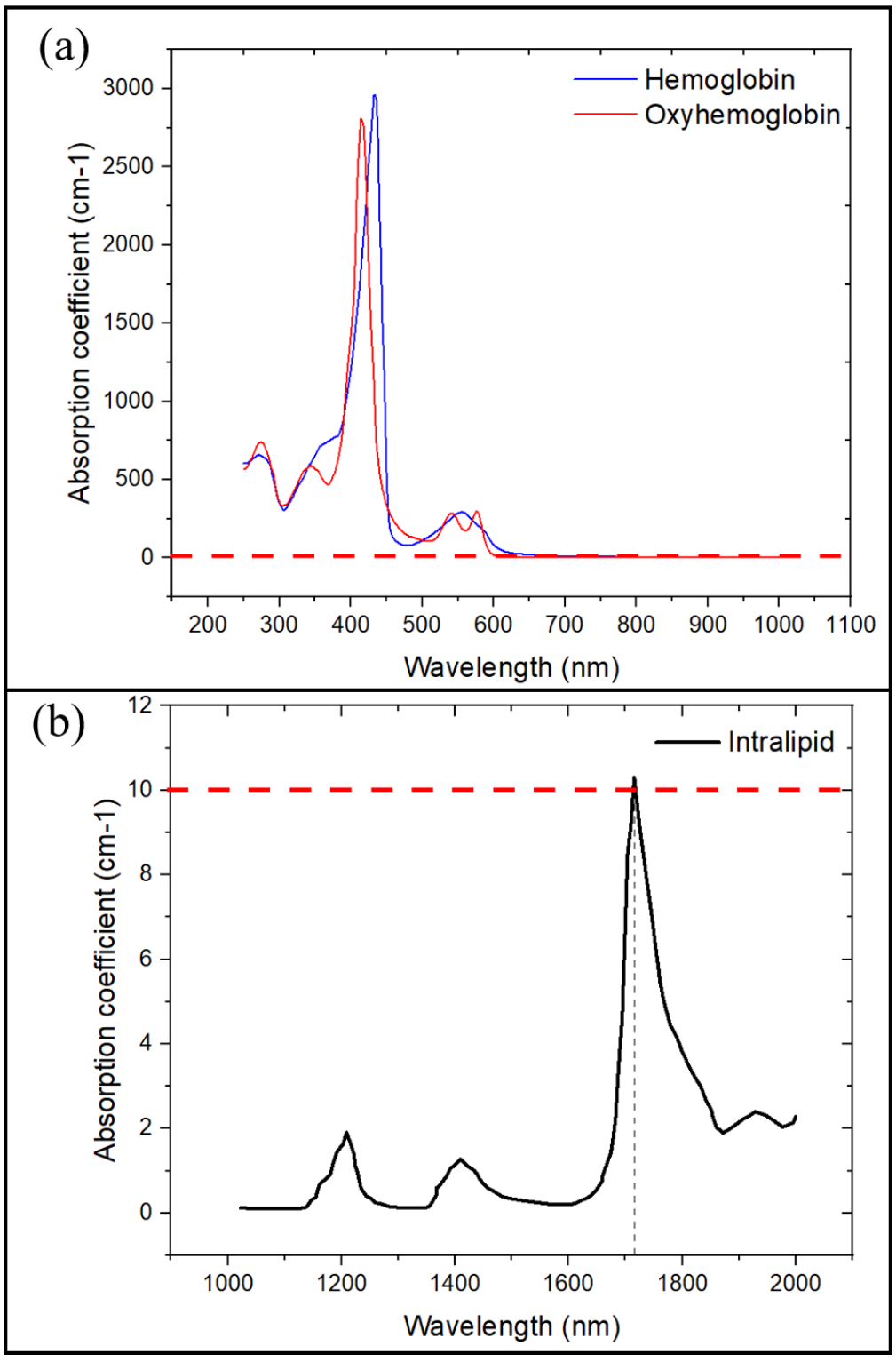

Figure 1.2 Optical absorption spectra of (a) oxyhemoglobin and (b) intralipid. The red dashed lines indicate the absorption coefficient at 10 cm^{-1}.

The coaxial design aligns the center axes of the laser beam and UST in a line, maximizing the overlap between optical and acoustic fields. However, the conventional

USTs fabricated by PZT are optically opaque, hindering light delivery. Previous efforts focused on designing complicated lens groups, such as the cone lens in acoustic-resolution photoacoustic microscopy (AR-PAM)[61] and the prism combiner in optical-resolution photoacoustic microscopy (OR-PAM)[34, 62]. Nevertheless, these lenses lead to bulky probes and longer working distances, which are not applicable in PAE. It is necessary to develop novel USTs compatible with coaxial design for PAE applications.

1.3 Photoacoustic Endoscopic (PAE) Catheter

To allow the device to enter the body, PAI is integrated into miniature catheters, typically consists of light delivery and PA signal detection. IV-PAE and GI-PAE represent two common designs[13], both demonstrating great potential in the studies of atheromatous plaque[14] and tumors[11, 63]. An imaging system is evaluated by resolution, sensitivity, speed, range and depth, but not all the parameters can be simultaneously improved by a new design. Whether in IV-PAE or GI-PAE, the development of new imaging catheter designs should prioritize clinical needs.

1.3.1 Intravascular Photoacoustic Endoscopy (IV-PAE)

1.3.1.1 Significance of Developing Intravascular Photoacoustic Endoscopy (IV-PAE)

Most of acute cardiovascular events are associated with atherosclerosis[64], which is a

chronic inflammatory disease[65]. Atherosclerosis features plaques and inflammation developed inside the arterial wall[66]. To prevent acute coronary syndromes, it is crucial to detect and identify vulnerable plaque at the early stage[67-69].

Previously, most research attention was directed towards PAI of artery intima, where plaque and inflammation generate[14]. However, recent studies discovered the significance of inflammatory cell information in the adventitia, which correlates with the severity of atherosclerotic plaques[70]. It has been proven that the formation of artery tertiary lymphoid organs (ATLOs), well-organized structures comprising B cells, T cells, and antigen-presenting cells, associated with atherosclerosis in mice[71, 72]. These ATLOs can establish an artery-brain circuit, potentially slowing down atherosclerosis progression and enhancing plaque stability[73]. Therefore, the information from the adventitia is significant for the diagnosis and remedy of atherosclerosis.

1.3.1.2 Current Design and Research Gap of Intravascular Photoacoustic Endoscopy (IV-PAE)

Various designs of IV-PAE catheters have been developed in the reported work[29, 74, 75]. Most of them feature a non-coaxial structure, i.e., oblique detection and side-illumination[16] or oblique illumination and side-view detection[21], leading to a limited overlap area for imaging. Although these catheters effectively image the lipids of the plaque, they lack the ability to detect inflammation over a long imaging range in the

adventitia. In some cases, imaging revealed the lipids in the pre-adventitia,[14-16] achieving with a large fiber core for tissue irradiation, demanding higher energy input and causing lower optical fluence.

The coaxial design can offer a longer imaging range than the conventional PA catheter[31, 76, 77]. In 2011, Wei et al.[76] developed the first coaxial PAE probe based on a hollow UST, which was with an outer diameter of 2.2 mm. In 2014, Wang et al.[31] reported another coaxial probe with a 2.9 mm-diameter transducer for a high-speed PAE. In 2016, Xiao et al.[77] developed a hollow structured lens-focused transducer with an outer diameter of 7 mm. All aforementioned PAE catheters demonstrated good performance in PAI. However, their bulky design renders them unsuitable for application in miniature cardio vessels.

In 2016, Cheng et al.[78, 79] developed a 400-μm-diameter multimode fiber with a 45° polished distal end for laser irradiation and photoacoustic signal reflection. The diameter of this catheter was down to 1 mm, but the PA signal collection depended on the surface of the fiber tip. The limited aperture of the fiber could not fully cover the aperture of UST, leading to weak detection and low signal-to-noise ratio (SNR).

The research gap in IV-PAE lies in the limited imaging range of miniature catheters. The coaxial design in IV-PAE is highly desired, which has the potential to extend the optical-acoustic area to provide more information in the adventitia.

1.3.2 Gastrointestinal photoacoustic endoscopy (GI-PAE)

1.3.2.1 Significance of Developing GI-PAE

GI endoscopy is a primary effective measure[80] for early detection and treatment guidance for GI tumors, contributing to improved five-year survival rate for patients[81]. The current clinical endoscopic methods, such as white-light imaging, narrow-band imaging, and fluorescence imaging, offer high-resolution visualization of superficial tissue and enhance the imaging contrast of vasculature. On the contrary, endoscopic ultrasound (EUS) delivers highly accurate assessments of tumor infiltration depth[82]. However, these methods cannot provide depth-resolved images of the vessel network that is associated with tumor angiogenesis.

When tumor cells grow, they consume nutrients and oxygen nearby, gradually triggering the formation of irregular nourishing blood vessels, known as angiogenesis[83]. Angiogenesis is an important characteristic of tumors that affects their growth and metastasis, and an accurate identification aids clinical diagnosis. Therefore, the development of GI-PAE catheters is of great significance in improving the sensitivity and specificity of early GI cancer diagnosis.

1.3.2.2 Current Study on GI-PAE and Its Research Gap

As a novel imaging tool, GI-PAE enables imaging of the vascular network in the GI

tract with high sensitivity and spatial resolution, providing both morphological and functional information. Various designs of miniature GI-PAE catheters have been developed for GI imaging. Among these studies, Yang et al. reported the first optical-resolution (OR) GI-PAE imaging on an *in-vivo* rat colorectum in 2015[18], achieving a 3D vasculature image with a high resolution of 9.2 μm. However, this catheter had a limited imaging range of 270 degrees, resulting in a blind area. Besides, its long rigid length (~40 mm) and large outer diameter (~3.8 mm) rendered it unsuitable for clinical GI endoscopy. Since then, a number of novel GI-PAE catheters have been developed to overcome challenges in *in-vivo* imaging. Yang et al. reported a series of GI-PAE catheters[84-89] to adapt irregular GI tract imaging with a 360° field of view. Guo et al.[90] utilized an optomechanical design to realize the focus adjustment in a flexible miniature GI-PAE probe. In the other group, a high-speed GI-PAE probe was introduced based on microelectromechanical systems (MEMS) scanning mirror[91].

Previous efforts focused on enhancing the imaging capability of catheters, aiming for adaptability and high imaging speed. Recently, Kim et al. presented a novel GI-PAE system featuring with a 3.38-mm diameter catheter[19]. This system conducted the GI imaging via the instrument channel of a clinical video endoscope, boosting the clinical translation of GI-PAE.

While most reported GI-PAE catheters were applicable in animal imaging, the dimensions of the human GI tract are much bigger. A research gap exists that the

reported GI-PAE catheters typically have a short depth-of-field (DOF), which cannot adapt to high-resolution imaging in the human GI tract while maintaining a miniature diameter (< 3.8 mm) simultaneously.

The irregular surfaces of folds, polyp, and swelling tumor in the GI tract require a large imaging DOF. Nevertheless, the imaging range of non-coaxial catheter structures is limited. Besides, the laser beam, usually with a Gauss-like distribution, has a short DOF hindering high-resolution imaging over long ranges. Thus, the development of a novel miniature coaxial GI-PAE catheter capable of high-resolution imaging in the human GI tract is significant to meet the need of clinical research.

1.4 Research Objectives

The study aims to develop novel PAE coaxial catheters for clinical research. Two kinds of catheters are fabricated and tested to show their performance in the proposed application. The coaxial IV-PAE catheter significantly extends the imaging range when compared to the conventional counterparts, while the coaxial GI-PAE catheter provides a longer focus length than the reported work.

The development of miniature USTs is a linchpin in this study. For the IV-PAE, a ring-shaped UST is investigated and fabricated, and the catheter structure is designed accordingly. The performance of the proposed catheter is evaluated by phantom and *ex-*

vivo experiments.

However, the miniature center orifice of the ring-shaped UST poses challenges in adapting to the big optical aperture. To further shrink the dimensions of the catheter, it is necessary to explore novel USTs for PA catheters. Transparent UST (TUST), utilizing transparent piezoelectric materials, is an emerging tool in PAI, offering potential for shrinking the probe structure and enhancing the optical efficiency. To verify the performance, a TUST based on LN and GRIN lens backing is studied and fabricated. The functions of flow sensing and PAI of probes are evaluated.

Finally, a coaxial GI-PAE catheter with a Bessel beam is investigated and fabricated. The Bessel beam, generated by a group of lenses, is tested by a CCD camera. The resolution of the proposed catheter is evaluated using blade-edge, demonstrating high resolution even over a long distance. The large DOF of the designed catheter is proven through imaging a phantom at different depths.

1.5 Overview

The thesis includes five chapters. The relationship of each Chapter is exhibited in Figure 1.3. Chapter 1 introduces the research background, covering fundamental knowledge of PAI, significance of PAE, and an overview of previous work along with identifying research gaps. The research objectives are outlined as well.

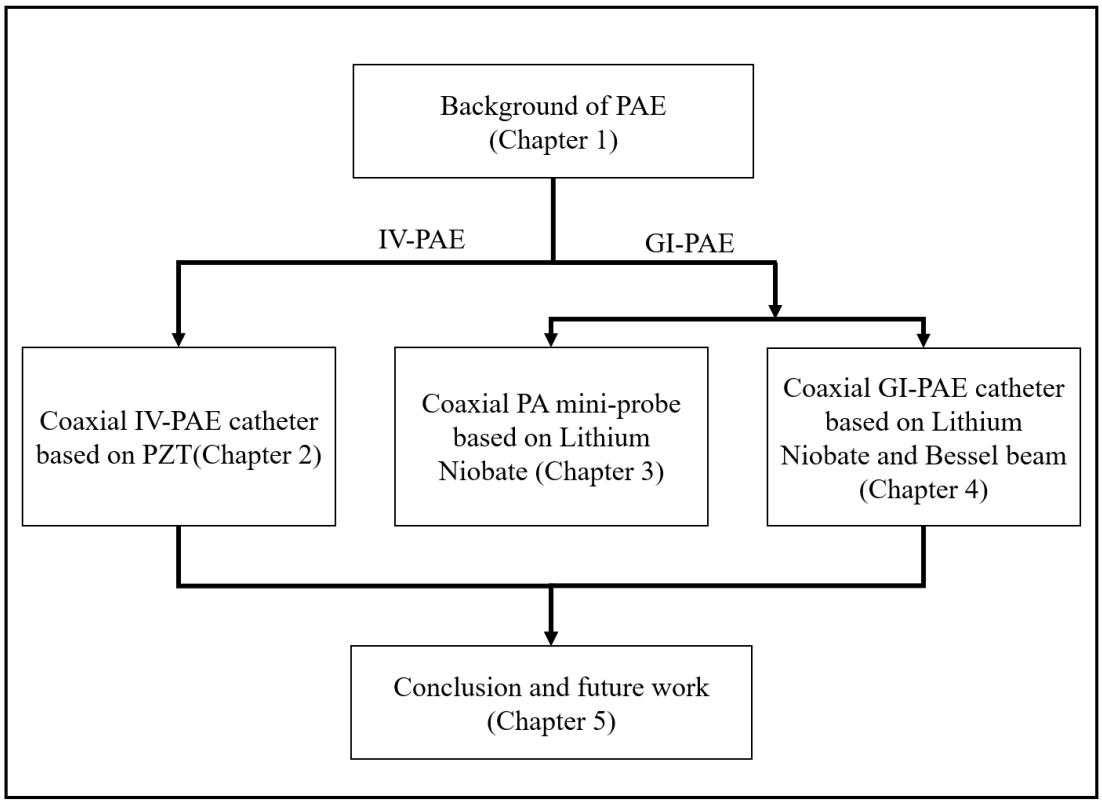

Figure 1.3 Flow chart of the content in this thesis.

Chapter 2 presents the coaxial design of a miniature IV-PAE catheter, including optical simulation, fabrication of the ring-shaped UST, performance test of the catheter and *ex-vivo* imaging results.

Chapter 3 studies the coaxial PAI probe for functional imaging, fabricated using a transparent single-crystal material (LN). The methodology of the proposed probe is detailed, and resolution and imaging results are presented. The results indicate the potential application of the TUST in the PAE catheter.

Chapter 4 presents the coaxial GI-PAE catheter using a Bessel beam, including evaluations of optical simulation and Bessel beam testing, the description of catheter fabrication method, and demonstration of the catheter performance through imaging

results such as the imaging range and the resolution.

Finally, Chapter 5 concludes the discussion on all the coaxial designs and outlines future directions for research.

Chapter 2 Coaxial IV-PAE

A PA catheter generally consists of acoustic and optical elements. The UST plays a critical role in this study, operating at frequencies ranging from 20 to 45 MHz. Given that the diameter of human coronary arteries falls within the range of 1.5 - 5.6 mm[92], the diameter of targeted catheter of ~0.9 mm is required to access these coronary arteries. This catheter should feature an ultrasound frequency of 30 – 35 MHz and a bandwidth of 40%. To achieve the coaxial configuration, it is necessary to develop a miniature ring-shaped UST.

2.1 Fabrication of Miniature Ring-shaped Ultrasound Transducer (UST)

2.1.1 Fabrication of Ring-shaped Ultrasound Transducer (UST)

An acoustic stack based on PZT-5H ceramics (CTS Corporation, USA) was prepared with dimensions of 10 mm × 10 mm and a center frequency of 30-MHz (shown in Figure 2.1a). The aperture of the ring-shaped stack correlates with the UST performance, needing to be big enough for fiber insertion yet small enough to fit within the miniature housing. The center orifice of the UST, set as 180 μm, facilities light delivery, enabling the multimode-fiber core to pass through. Laser micromachining was applied to process the center orifice for the fabrication of ring-shaped UST. To adapt the 0.9 mm-diameter housing of the catheter, a 0.6 mm × 0.6 mm × 0.4 mm hollow acoustic stack (Figure 2.1b) was cut from the proposed stack using a dicing saw (ZHZZ-SD4800, DISCO

Corporation, Japan).

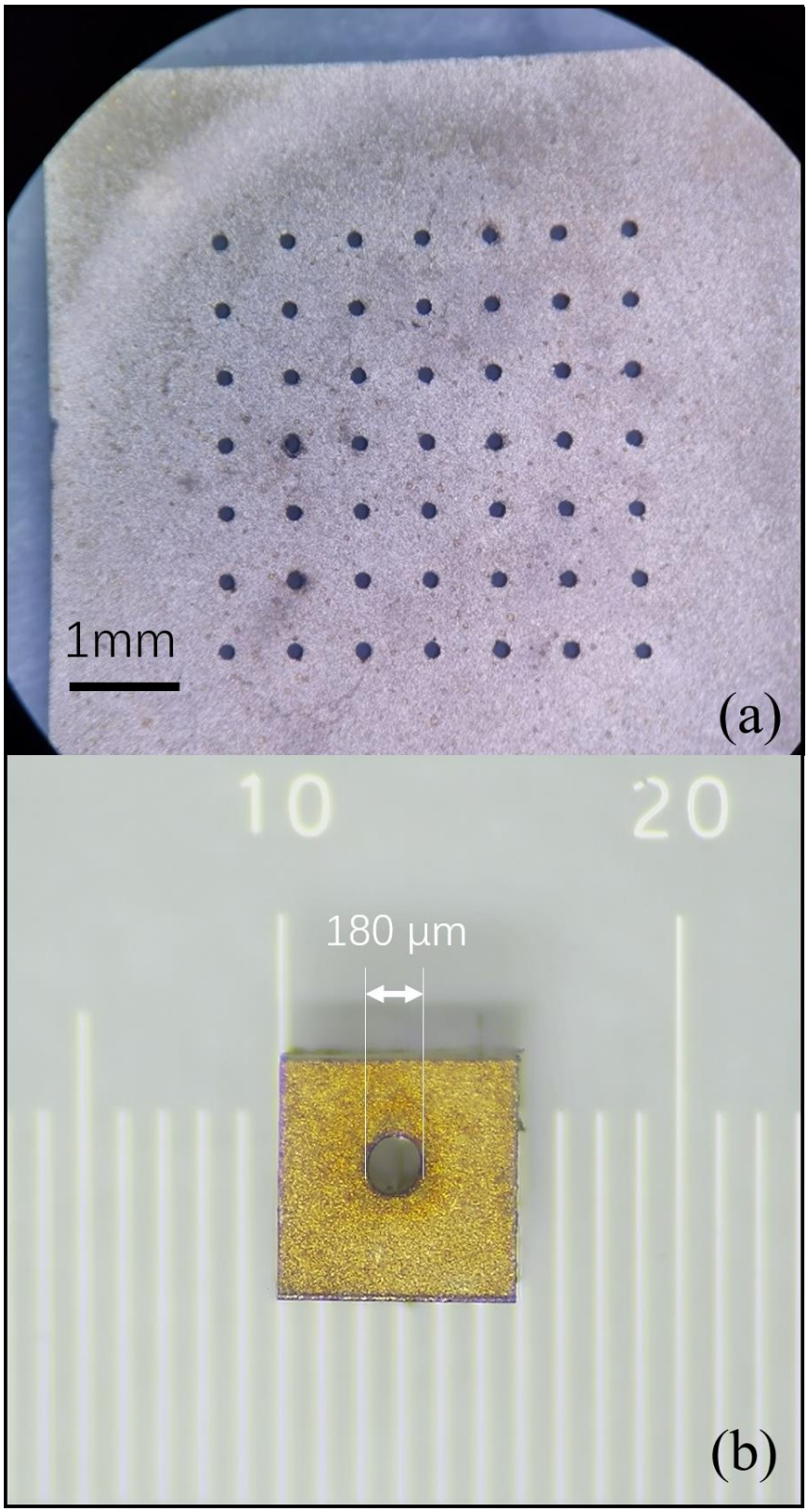

Figure 2.1 a. Photo of a home-made acoustic stack with dimensions of 10 mm × 10 mm and 49 orifices; b. Photo of a ring-shaped acoustic stack with dimensions of 0.6 mm × 0.6 mm × 0.4 mm and a ~0.18 mm-diameter central orifice.

The thickness plays a critical role in the UST design. While a thick stack may facilitate electric wire connection and IV-PAE catheter fabrication, it could result in less accuracy in the orifice diameter. This is because the focused laser beam used for micromachining, with a large NA, may cause size deviation between the front and back surfaces, which is more obvious in thicker stacks.

To present the effect of laser micromachining on the UST performance, a square stack with the same dimensions but without a center orifice was prepared (referred as the homemade square stack). Besides, a commercial PZT-5H-based UST (Insight Lifetech Co., Ltd., China) with the same dimensions was purchased (referred to as the commercial square stack) for performance comparison.

2.1.2 Performance Test of Ring-shaped Ultrasound Transducer (UST)

To evaluate the UST performance, pulse-echo tests were conducted on the proposed transducers using the aforementioned acoustic stacks. As shown in Figure 2.2, the center frequency of UST fabricated using the commercial square stack was ~34 MHz (Figure 2.2a), which was slightly higher than that of the homemade square one (30 MHz). Its peak-peak echo amplitude was ~3.5V, showing better sensitivity when compared to the homemade UST (Figures 2.2b and c), possibly due to the variations in terms of UST stack design, fabrication, and materials. Piezoelectric performance may not be affected by laser micromachining on center orifices, but the acoustic detection

area was reduced such that the ring-shaped UST would exhibit lower sensitivity but wider bandwidth than the UST fabricated using the homemade square stack as shown in Figure 2.2c. The UST properties including center frequency, bandwidth, and echo amplitude, are summarized in Table 2.1.

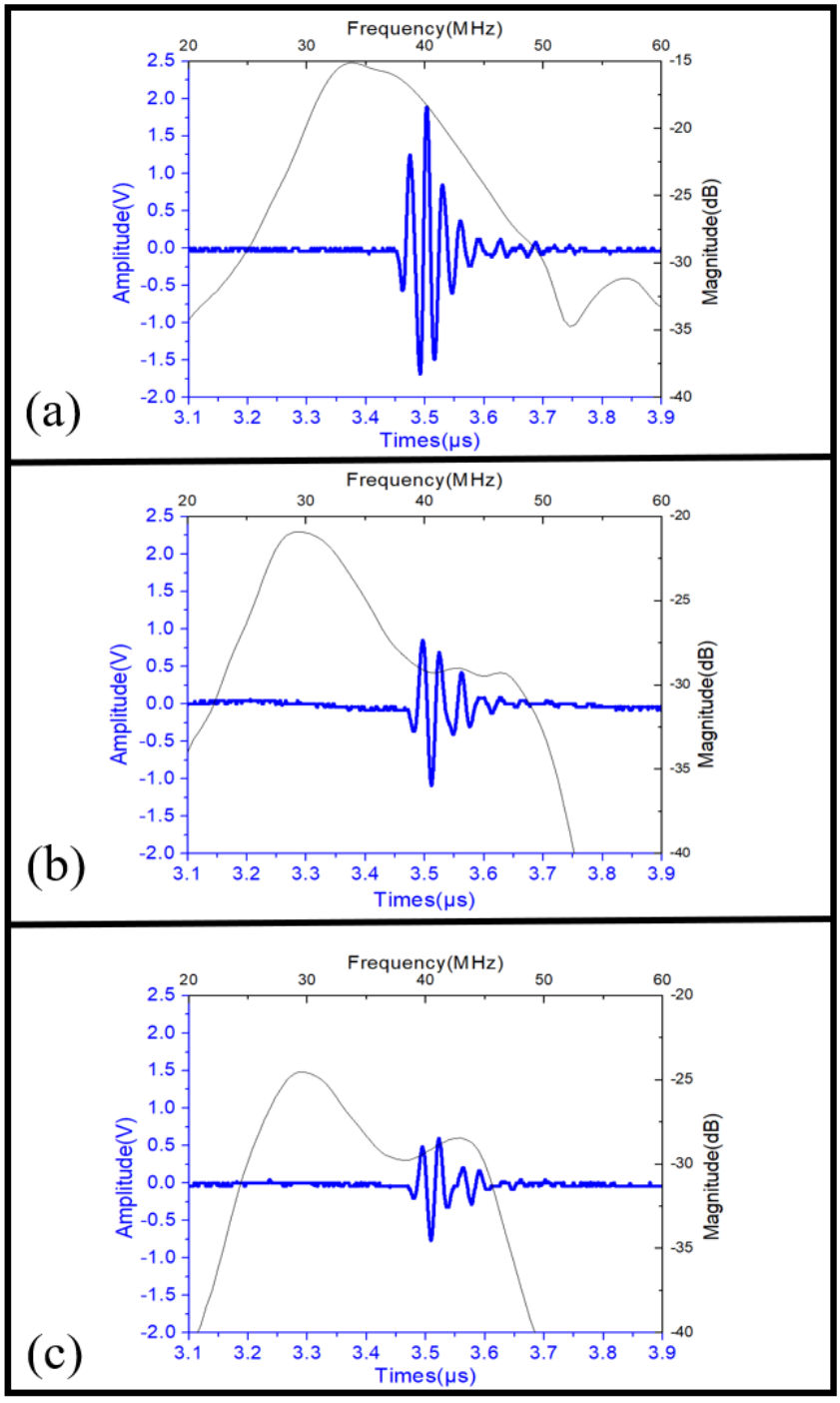

Figure 2.2 Pulse-echo waveforms of USTs fabricated using different acoustic stacks. (a) commercial square stack, (b) homemade square stack, and (c) hollow stack.

Table 2. 1 Properties of transducers fabricated using different acoustic stacks.

	Frequency (MHz)	*-6 dB Bandwidth (%)*	*Peak-to-peak echo voltage (V)*
Commercial square stack	34	40%	3.54
Homemade square stack	30	40%	1.94
Hollow stack	35	60%	1.36

2.2 Fabrication of Intravascular Photoacoustic Endoscopic (IV-PAE) Catheter

2.2.1 Optical Simulation

The laser energy from the IV-PAE catheter should be limited to a safe range to avoid tissue burns. To calculate the optical fluence in different designs, simulations of laser beams were conducted. Figure 2.3 presents the schematics of the configuration of the non-coaxial and the coaxial catheter designs. The profiles of the laser beam were simulated in the ZEMAX software (shown in Figure 2.4). As shown in Table 2.2, the diameters of laser spots from different catheter designs along with the imaging distance were calculated.

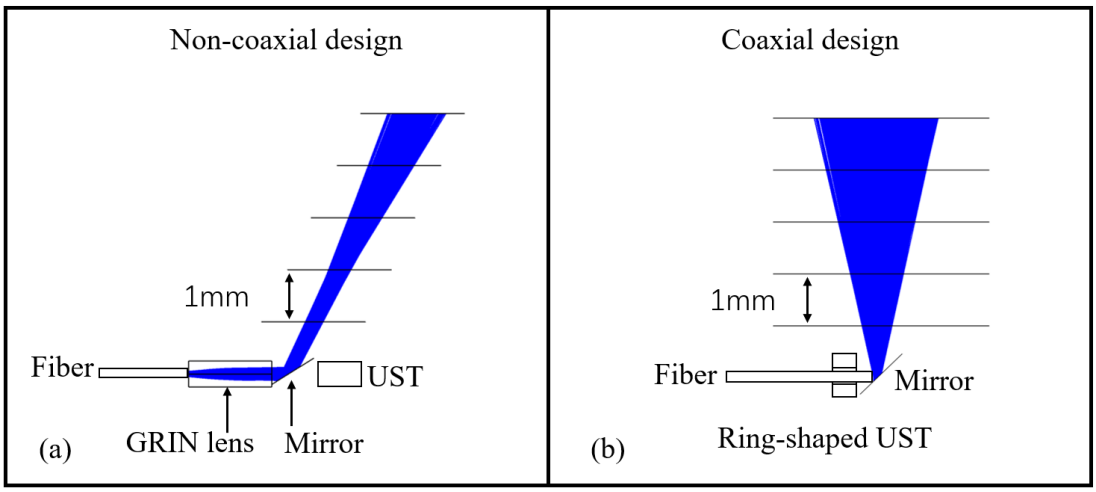

Figure 2. 3 Schematics of optical irradiating from different catheter designs. a. Configuration of non-coaxial design; b. Configuration of coaxial design.

Figure 2.4 presents the variance of optical fluence from coaxial and non-coaxial designs distributed along the imaging distance. The results were calculated based on the simulated data of spot diameter (shown in Table 2.2). In this work, the laser energy from the tip of both catheters was ~20 μJ. While the irradiation area of coaxial design at the depth of 1 mm was ~440 μm, resulting in the optical fluence of ~6.22 mJ/cm^2. The optical fluence meets the ANSI standard.

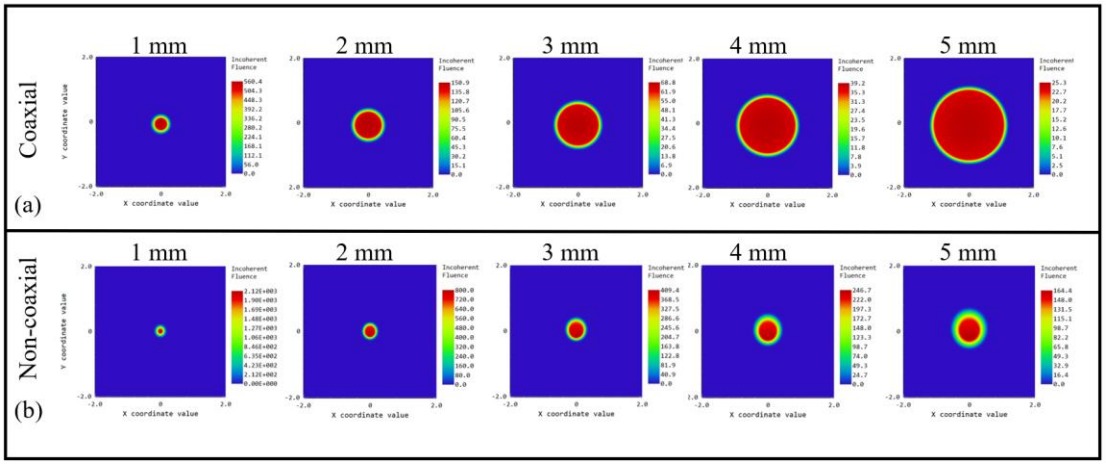

Figure 2.4 Laser spot results of two designs at different distances.

Table 2.2 Diameters of the laser beam obtained from different catheter designs along with the imaging distance.

Imaging distance (mm)	1	2	3	4	5
Laser spot diameter (μm)					
Non-coaxial design	440	540	774	1036	1312
Coaxial design	640	1100	1560	2000	2400

As shown in Figure 2.5, the optical fluence of the non-coaxial catheter was about 13.15 mJ/cm^2 at the depth of 1 mm, which was double that the coaxial one. The difference in value got smaller along with the increasing distance, but the optical fluence of the non-coaxial design was about triple that of the coaxial one at the depth of 5 mm.

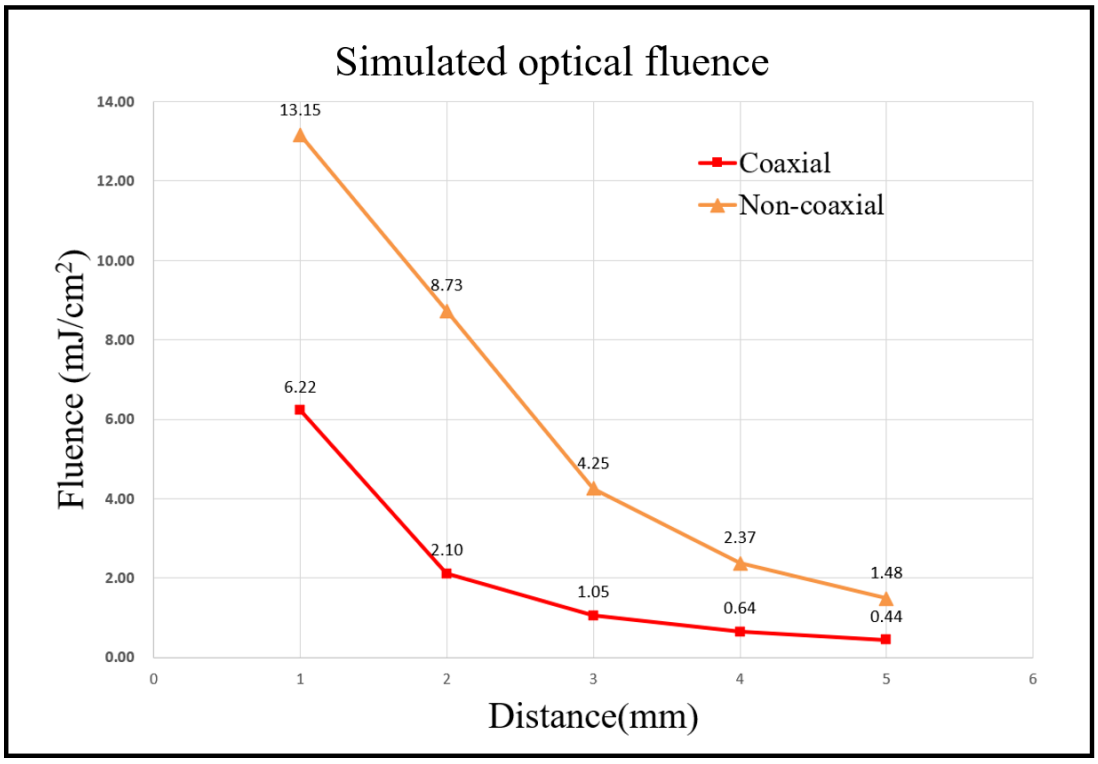

Figure 2. 5 Simulated optical fluence based on the spot diameter.

2.2.2 Catheter Structure

The miniature IV-PAE catheter was developed as exhibited in Figure 2.6. The UST with a center orifice was applied to detect the PA and US signals reflected from the rod mirror. To avoid electrical disconnection between the housing, matching layer and backing layer, the ring-shaped acoustic stack cannot be placed directly on the inner wall of the housing. Here are the assembling steps: (1) The positive electrode of the wire should be connected to the backing layer of the ring-shaped stack using the electrically conductive silver adhesive (E-solder 3022, Von Roll, Switzerland), while the negative electrode of the wire was pressed on the inner wall of catheter housing by the ring-shaped stack. (2) The E-solder was applied to ensure the electrical connection between

the catheter housing, negative electrode, and matching layer of the stack. (3) When the wire connection was finished, the Parylene C powder was deposited as the waterproofing layer and the second matching layer of the ring-shaped UST. (4) A bare multimode fiber (FG105LCA, Thorlabs, Newton, NJ, USA) a core diameter of 105 μm was inserted into the center orifice of the UST. (5) A custom-made 0.78 mm-diameter silver rod mirror with a 45° angle was positioned at the tip of the catheter housing for reflecting the laser beam and PA/US signals. (6) A customed torsion coil (0.88 mm-outer diameter, Asahi, Japan) was inserted into the housing, facilitating the rotation scanning. (7) All the optical and acoustic components were fixed using the electrically insulating epoxy (301, Epoxy Technology Inc., Billerica, MA, USA).

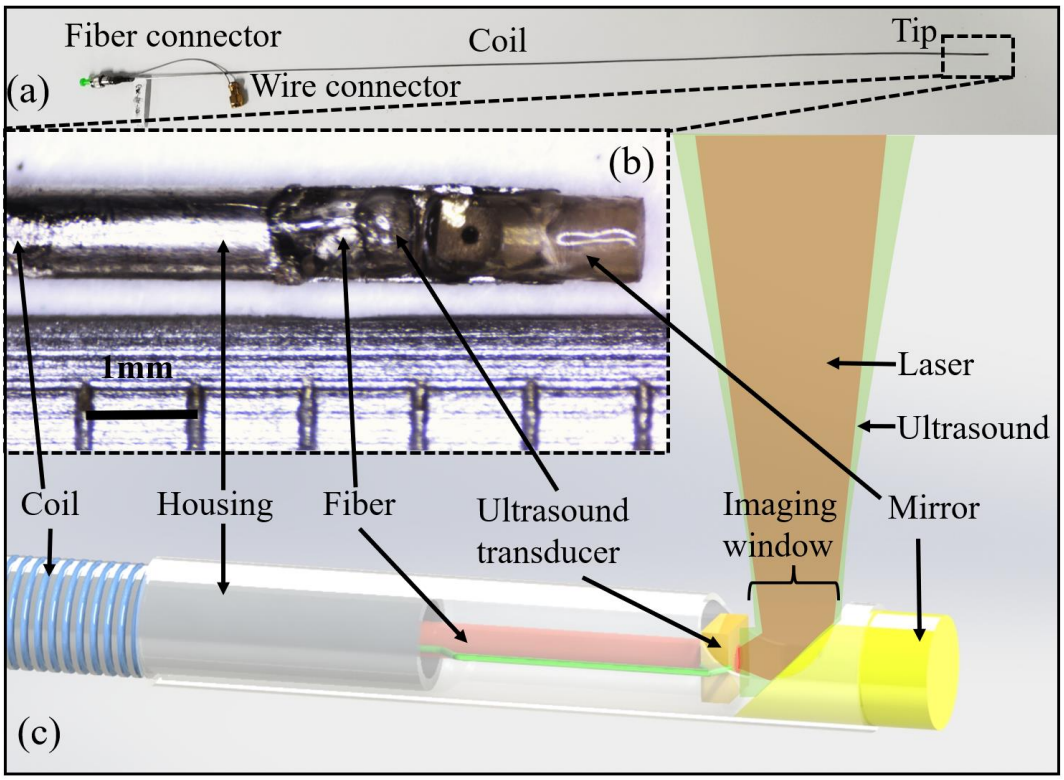

Figure 2.6 Photos and schematic of the coaxial intravascular photoacoustic catheter. (a) Photo of the whole catheter; (b) Zoom-in photo of the tip of the catheter; (c) Schematic of a 3D model of the catheter.

To verify the significance of coaxial design, a non-coaxial IV-PAE catheter with the same configurations (see Figure 2.3a) was fabricated using the commercial square stack for performance comparison.

2.2.3 Photoacoustic Endoscopic (PAE) System

A PAE system was fabricated for PA/US imaging using the proposed catheters. The schematic of the system is displayed in Figure 2.7. The signal from the pulsed laser source was applied to trigger the synchronization of a data acquisition (DAQ) board (ATS9350, Alazar Tech, Canada) and control the translation and rotation of the catheter. Simultaneously, the trigger signal was sent to a custom-made delay module to provide a 5-μs delayed trigger signal for a US pluser/receiver (5073PR, Olympus, Japan) to form a PA image. A pulsed Nd:YAG laser (1064 nm, Medical Technology (Shenzhen) Co., Ltd, China) was used for photoacoustic excitation. Laser energy was delivered through a multi-mode fiber (FG105LCA, Thorlabs, Newton, NJ, USA) with a 0.22 NA, which transmitted through a slip-ring (Shenzhen CENO Electronics Technology Co., Ltd, China) into the catheter. The detection of PA/US signals from the biological tissue was performed using the ring-shaped UST. Both PA/US signals were amplified (39 dB) in the pulser/receiver and then digitized with the DAQ board.

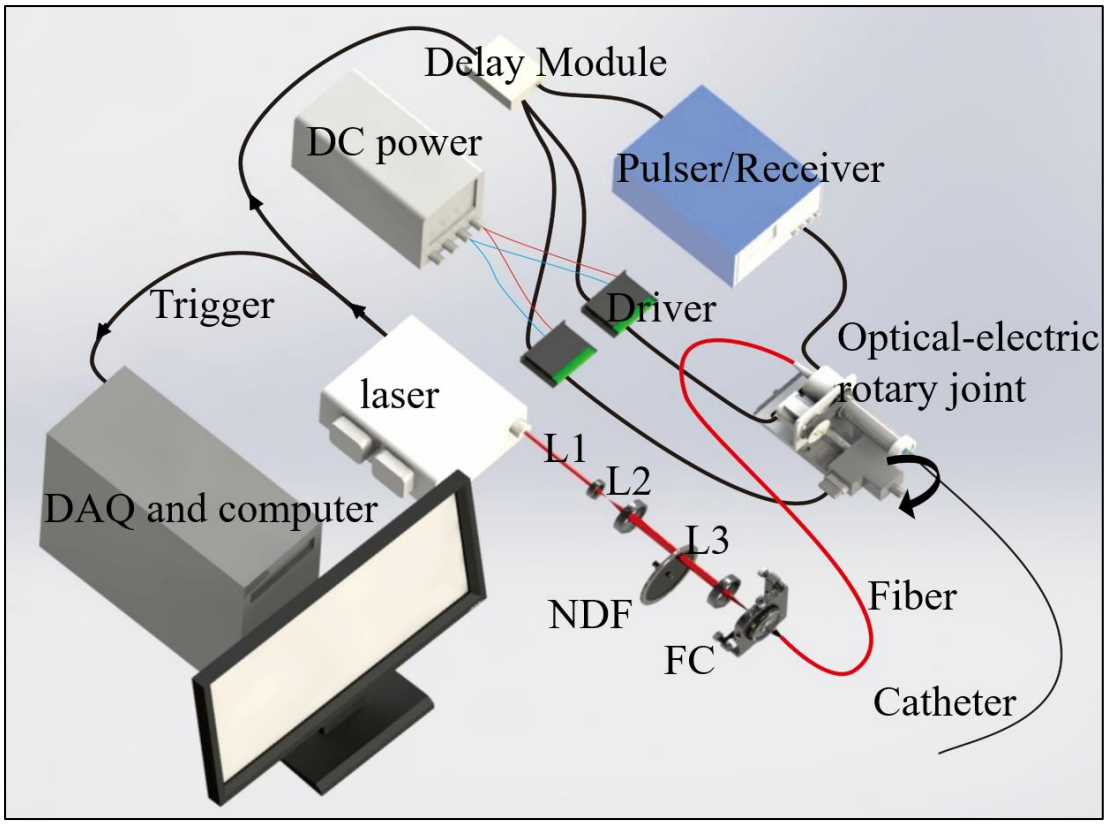

Figure 2.7 Illustration of the coaxial intravascular photoacoustic system. The optical-electric rotary joint includes a slip ring and step motor, which drives the catheter to rotate continually and enables the laser beam (red line) to perform 360° scanning. DC, direct current L1-3, condenser lens 1-3; NDF, neutral density filter; FC, fiber coupler.

2.2.4 Phantom Preparation

To evaluate the imaging performance of the catheters with the coaxial and non-coaxial designs, a phantom was developed using 50 μm-diameter tungsten wires. The tungsten wires were distributed vertically with a 0.5-mm gap on a 3D-printed model, as shown in Figure 2.8. During the imaging experiment, the catheters moved horizontally (shown by the black arrow in Figure 2.8(a) to scan the tungsten wires in a water tank.

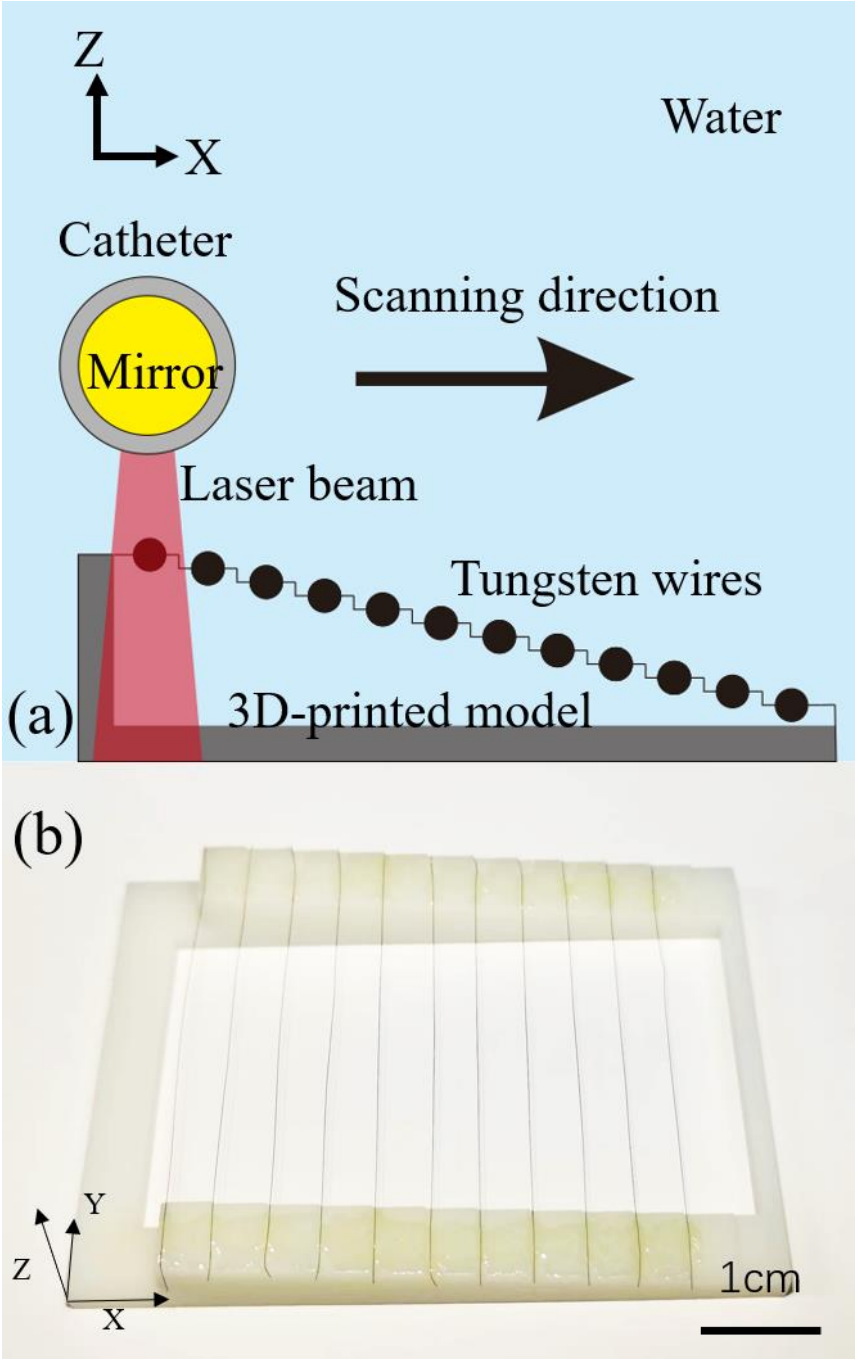

Figure 2.8 (a) Schematic and (b) photo of a wire phantom comprising tungsten wires at different depths.

2.3 Performance Test of Coaxial Catheter

2.3.1 Resolution Test

Figure 2.9 shows the PA/US imaging results acquired from the coaxial and non-coaxial

catheters. Figures 2.9(a) and (b) are the PA/US images acquired from the coaxial catheter, in which both imaging depths were over 5.5 mm. The non-coaxial design provided higher amplitude signals due to the better sensitivity of the commercial acoustic stack, but its PAI depth was shorter than 2.5 mm as shown in Figures 2.9(c). The results demonstrate that the coaxial catheter configuration could offer a larger imaging range than the non-coaxial one. Although the detection sensitivity was affected by the reduction of stack aperture size, the ring-shaped UST showed the potential of having sufficient sensitivity for imaging the inner structure of the vessel.

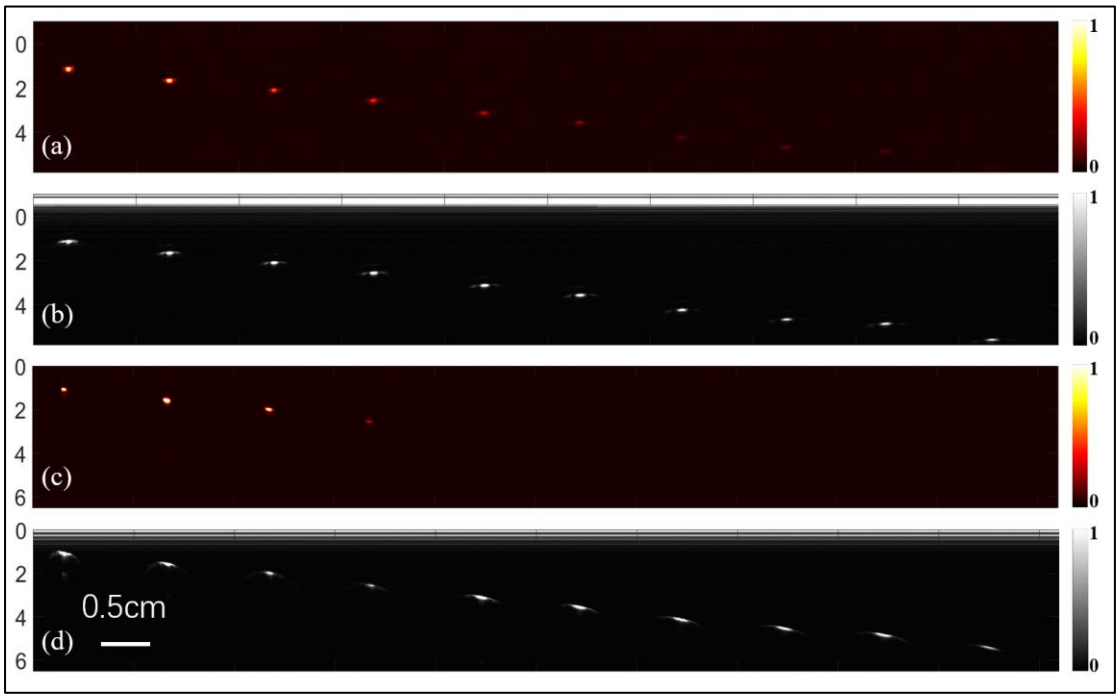

Figure 2.9 PA/US images of tungsten wire phantom acquired using the coaxial and non-coaxial catheter. (a) PA image from the coaxial catheter; (b) US image from coaxial catheter; (c) PA image from the non-coaxial catheter; (d) US image from non-coaxial catheter. The PA/US images are displayed with the same normalized range, respectively

It is worth noting that the imaging started from -1 mm using the coaxial design as shown in Figures 2.9a and b, which was the measured distance between the ring-shaped UST and the mirror center (~1 mm). On the other hand, in the non-coaxial catheter, the UST

usually aligned with the axis of the housing, facing the imaging window. However, the side-view detection and oblique illumination in the traditional non-coaxial design often led to signal loss within the region of the high-amplitude initial excitation signal. When compared to the non-coaxial catheter, the coaxial catheter offered advantages by eliminating interference caused by the initial excitation signals, which proved particularly beneficial for imaging targets positioned in close proximity.

2.3.2 Imaging Signal-to-noise Ratio (SNR) and Resolution

Figure 2.10 shows the measured results of SNR in PA/US imaging acquired from two different designs. Obviously, the PA images acquired using the coaxial catheter had better SNR at long distances compared to those from the non-coaxial design in Figure 2.10a. Although the overall SNR of US images from the coaxial catheter appeared lower than that of the non-coaxial one, both designs had high SNR levels of over 30 dB along the distance.

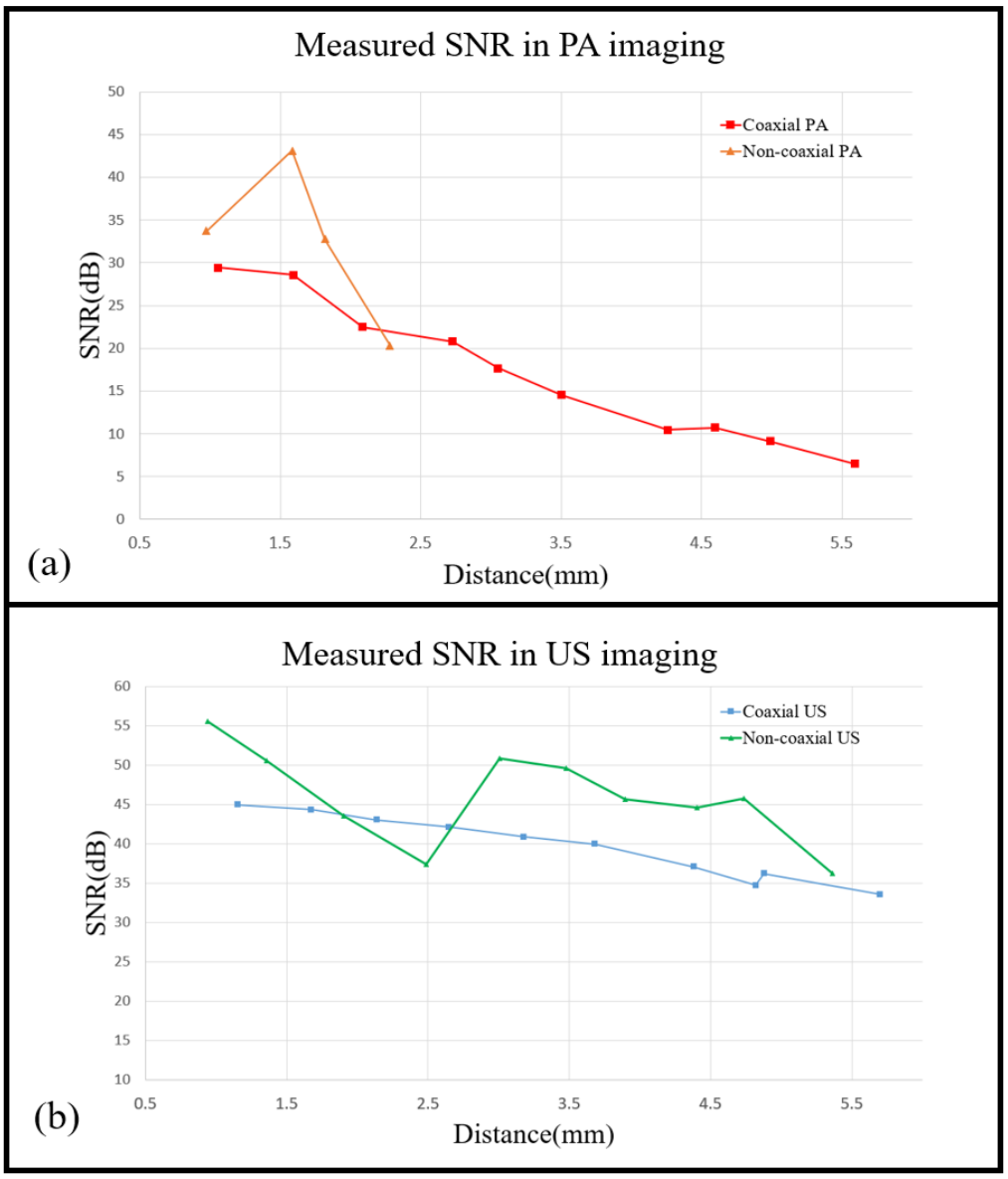

Figure 2.10 Comparison of image SNR based on Figure 2.8. (a) Measured SNR in PA imaging; (b) Measured SNR in US imaging.

Figure 2.11 presents the imaging resolutions measured using the wire phantom (shown in Figure 2.8). All curves have a similar trend after the distance of 1.5 mm. Specifically, the PA resolution of a non-coaxial catheter has the highest resolution of ~220 μm at the depth of ~1 mm. The PA/US resolution curves of the coaxial catheter align closely, almost overlapping each other.

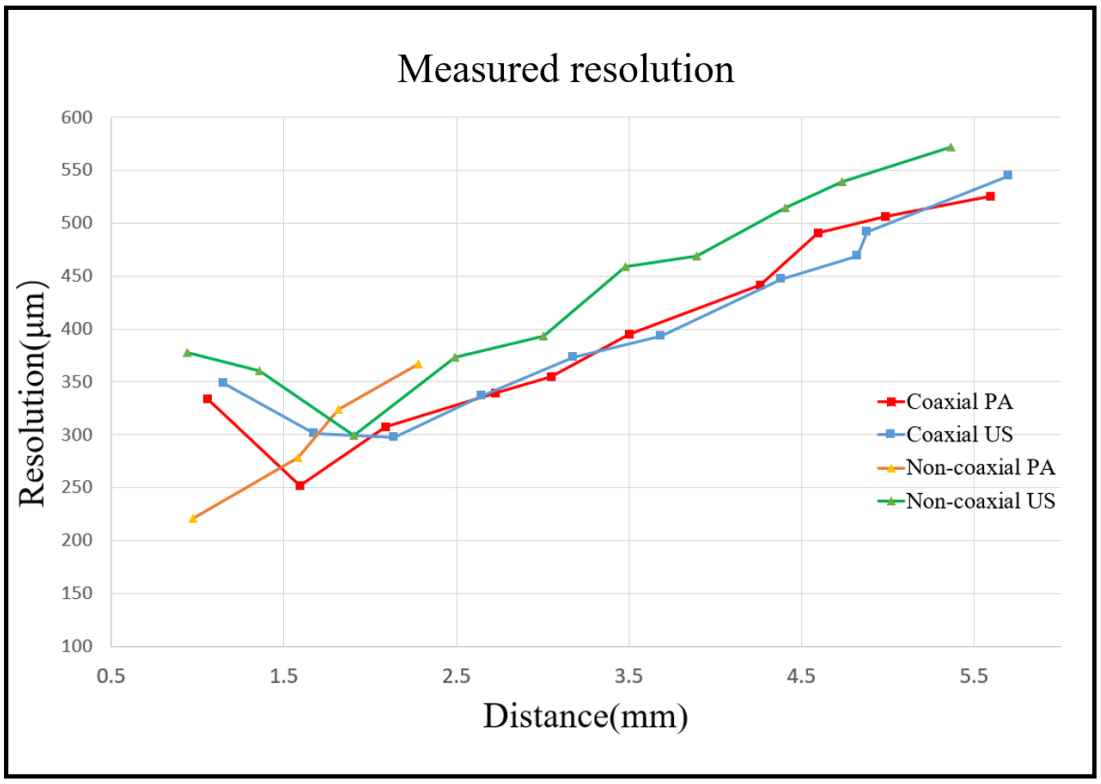

Figure 2.11 Comparison of measured PA/US resolutions.

2.3.3 *Ex-vivo* Experiment

2.3.3.1 *Ex-vivo* Phantom Preparation

To further confirm the advantages of the coaxial design, *an ex-vivo* imaging experiment was conducted using a porcine heart. Figure 2.12(a) is a photo of a fresh porcine heart obtained from a local slaughterhouse. The porcine tissue with a coronary artery was cut and fixed in agar for the imaging experiment (shown in Figure 2.12(b)), which was soaked in the formalin for 24 hours for fixation.

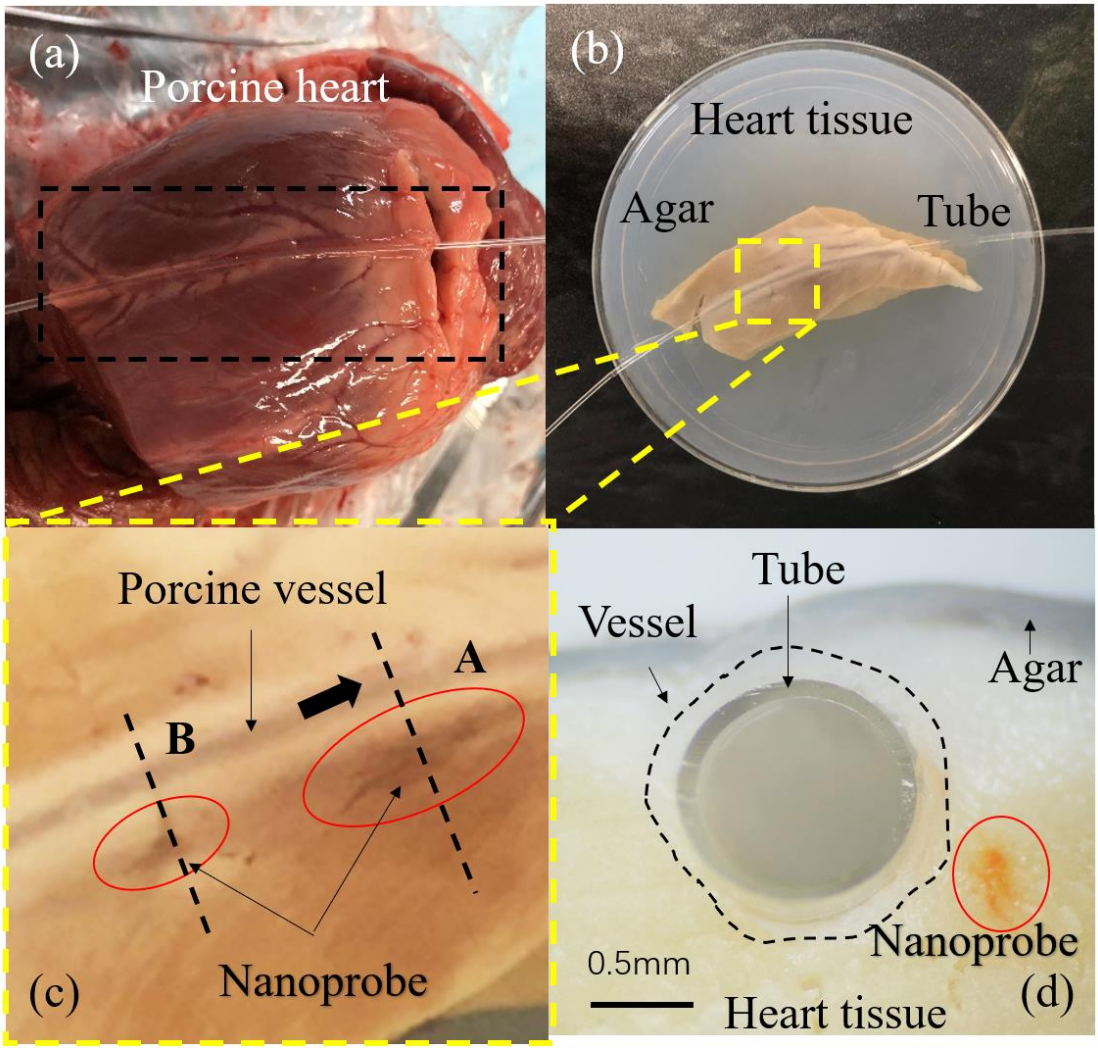

Figure 2.12 Photos of porcine heart tissue. (a) Photo of fresh porcine heart; (b) Photo of the *ex-vivo* porcine heart tissue fixed in agar; (c) Zoom-in image of (b), indicating the imaging Sections and the position of injected nanoprobes; (d) Cross-sectional image in the viewing angle of black arrow in (c). Red circle indicates the position of injected nanoprobes. Black dash lines show the scanning sections. A black dash circle shows the profile of the porcine vessel.

Generally, inflammation cells could not be detected by PAI directly in atherosclerosis due to their weak optical absorption. To address the issue, exogenous nanoprobes are usually employed for targeted detection of inflammation cells. In this work, 1 mL solution of 1064-nm PA nanoprobes was injected into the tissue near the artery wall (shown in Figure 2.12(c)) to mimic the targeted cells in the adventitia. To prevent the potential evaporation or outflow of nanoprobes from fresh tissue after immersed in

water, porcine heart tissue was preprocessed in formalin and then fixed in agar to ensure the retention of the nanoprobes. At the beginning of imaging, both catheters were individually inserted into the tube. Following the experiments, the coronary artery was incised. Its cross-section is shown in Figure 2.12(d), highlighted by a red circle.

2.3.3.2 Nanoprobes Preparation

In the *ex-vivo* experiment, nanoprobes were used to mimic inflammation. The laser wavelength was 1064 nm for irradiation. To develop the NIR-II-absorbing nanoprobe, the water-insoluble NIR-II small molecule dye IR1048 was employed as the optical absorber. To facilitate the dissolution of IR1048 in water, F127, a surfactant, was used. In brief, IR-1048 and F127 were mixed and dissolved in dichloromethane with a mass ratio of 1:50. The mixture was then placed in a US bath (VCX150, SONICS, USA) for 30 minutes. Subsequently, the mixture was evaporated using a rotary evaporator to remove the dichloromethane. With ultrasonication, the resultant thin film was dispersed in distilled water for 30 mins to form the final nanoprobes solution. Before injecting nanoprobes into tissue, the solution was diluted to 50 g/mL.

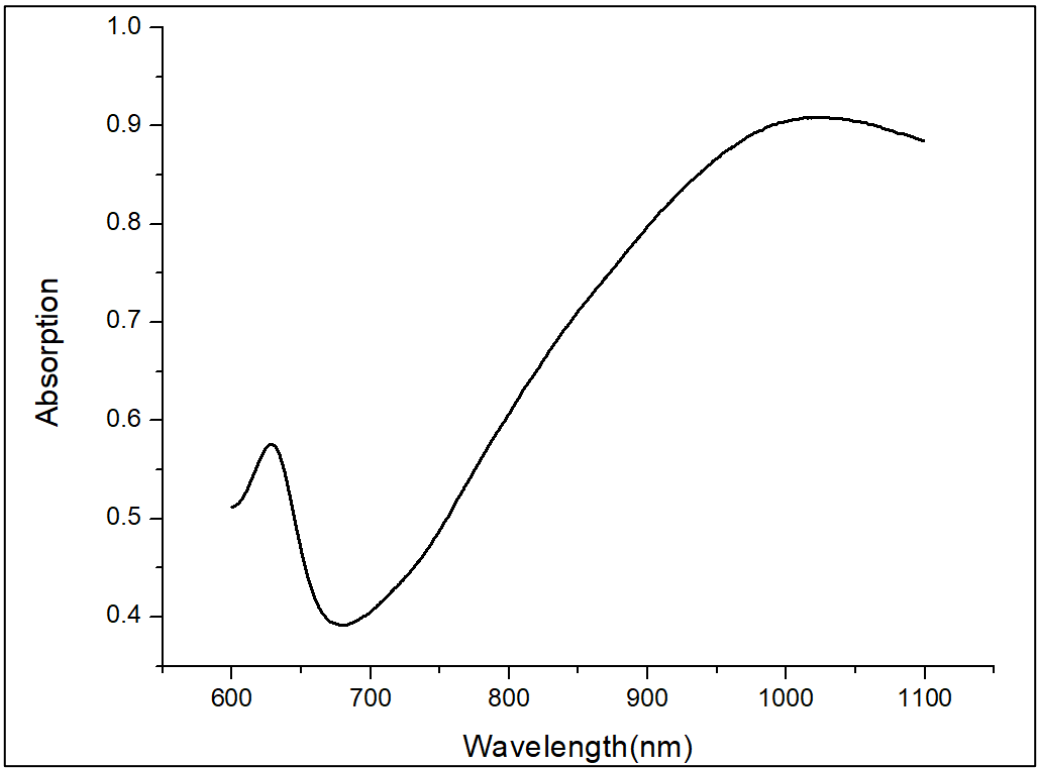

Figure 2.13 Measured optical absorption of nanoprobes.

To demonstrate the performance, the optical absorption spectrum of the nanoprobe solution was analyzed. As shown in Figure 2.11, the absorption of the nanoprobes at 1064 nm was ~0.9 with a cuvette length of 1 cm. According to the formula:

$$Absorption = absorption\ coefficient * concentration * absorption\ length \quad (2.1)$$

The absorption coefficient of the nanoprobes was calculated as 18 $L/g \cdot cm^{-1}$, which has high sensitivity for PAI.

2.3.3.3 *Ex-vivo* Imaging Results

The catheter was inserted into a protective tube to enter the porcine coronary artery for

PAI. The imaging results are demonstrated in Figure 2.13.

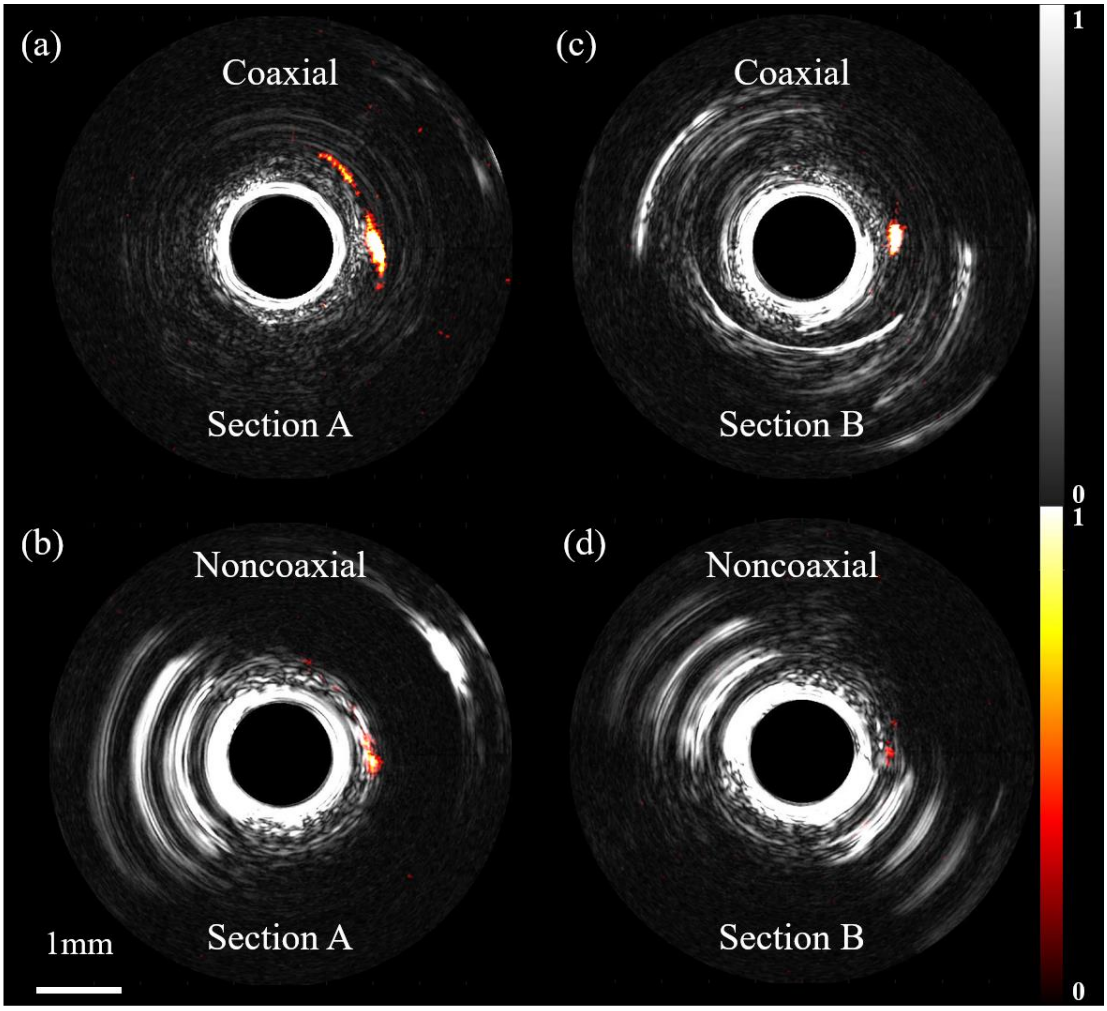

Figure 2.14 *Ex-vivo* imaging results acquired by the coaxial and non-coaxial catheters. Fused B-scan images of PA/US images of (a, b.) Section A and (c, d.) Section B. The PA/US images are exhibited with the same normalized range, respectively.

Figure 2.13 shows the B-scan results of two designs, comprising combined PA/US images of Sections A and B (Figure 2.12(c)) of the coronary artery. Figures 2.13(a) and (c) are PA/US fused images acquired by the coaxial catheter, in which the PA signal of the proposed NIR-II nanoprobes can be imaged in the 2-mm depth. For the images acquired from the non-coaxial catheter (shown in Figures 2.13b and d), US signals reflected from the tube were very strong due to the high sensitivity of the commercial acoustic stack. All the images are displayed with a normalized range. The imaging

results demonstrated the superior imaging quality and depth capabilities of the coaxial design over the conventional non-coaxial design.

2.4 Discussion

Atherosclerotic plaque and inflammation are the key features in the diagnosis of acute heart disease, typically spanning from the layers of intima to adventitia. To reach deeper imaging depths and meet the clinical operation standard, it is necessary to simultaneously maximize the light-sound overlap area and minimize the catheter dimensions. Though previous works have addressed the fabrication of hollow UST, the bulky acoustic stack impedes its insertion into a ~1 mm-diameter artery for IVPA imaging. Coaxial PA catheters using 3D-printed models have been reported to collect reflected signals from a big optical fiber core, but the design fails to cover the imaging window, resulting in an apparent loss of signal.

To access the coronary artery, the IV-PAE catheter should be limited to 1 mm in diameter, thereby restricting the size of the UST. Miniature ring-shaped USTs play a crucial role in coaxially combining the optical and acoustic areas, which is more important than simply reducing the stack size. Several considerations are important in the design and fabrication: (1) An orifice diameter should be carefully designed to balance between the dimensions of the optical fiber and the detecting area. (2) Due to the big NA of the micromachining laser beam, the thickness of PZT stack should not

exceed 0.5 mm to compensate for the micromachining errors between the front and back of the center orifice, thereby minimizing the area mismatching in each layer. (3) The Parylene coating must be performed after the UST fixation but before the fiber installation in the housing. This sequencing avoids damage caused by the high-power laser during micro processing. All these factors should be taken into account during the fabrication process of coaxial catheters to ensure the performance and functionality.

UST performance and optical fluence significantly impact the SNR in PAI. The aforementioned factors are closely related to the properties of the acoustic stack, while the latter one relates to the laser energy and optical focusing. As shown in Figure 2.4, due to laser beam focusing by the GRIN lens, the non-coaxial catheter provided better optical fluence than the coaxial configuration. Nevertheless, the coaxial catheter presented a better depth performance for both PA/US imaging (shown in Figures 2.5) due to its larger light-sound overlap area. Signal fluctuations observed in the non-coaxial US curve in Figure 2.5(b) were attributed to tungsten wire distortion.

When the US detection area is smaller than the laser spot, both PA/US imaging resolutions depend on the acoustic resolution. In Figure 2.10, all the PA/US resolutions had a similar trend, progressively increasing with imaging distance. The PA resolution of the non-coaxial catheter was measured as ~220 μm at a depth of ~1 mm due to the focusing laser beam formed by the GRIN lens. This result is consistent with the

simulation results (see Table 2.2), where the laser spot at the depth of ~1 mm was ~440 μm, nearly encompassing the full width of the resolution.

The coaxial catheter offered better PAI depth than the non-coaxial one in both phantom and *ex-vivo* porcine artery experiments. The PAI depth of tungsten wires acquired by the coaxial catheter reached over 5 mm (Figure 2.8(a)). Besides, the nanoprobes in the adventitia and the structural features of porcine artery can be imaged with high sensitivity (Figures 2.13(a) and (c)). Though both the optical fluence of the non-coaxial catheter and the sensitivity of the commercial acoustic stack were higher, the nanoprobes could not be fully imaged because of the limited optical-acoustic overlap area in the non-coaxial catheter configuration (Figures 2.13(b) and (d)). All the results suggest the superiority of the coaxial design in acquiring more information compared to the conventional non-coaxial design. The imaging range of the coaxial design spans from the intima to the adventitia of the atherosclerotic artery.

Strong reflections are seen in Figures 2.13(b) and (d), which are attributed to the non-coaxial configuration. In the coaxial design, the UST sat closely with the surface of the protective tube surface, easily reflecting the US signal from the inner surface during imaging scanning. Moreover, the high sensitivity of commercial acoustic stack amplifies the reflected signals.

While this study demonstrated the potential of the coaxial catheter design, there remains room for further improving the catheter performance and the potential for clinical applications. For example, the utilization of better piezoelectric materials such as PMN-PT single crystal or corresponding 1-3 composite may improve the imaging performance. Besides, the optimization of laser beam using miniature optical components could increase the optical fluence and improve the resolution of system. Finally, to further strength the biomedical imaging capability, integrating multiple imaging modalities into the coaxial catheter, such as OCT, could further enhance diagnostic efficacy.

2.5 Conclusion

In summary, this work presents the development of an IV-PAE catheter featuring coaxial excitation and detection. The miniature ring-shaped UST is successfully fabricated using laser micromachining. The detecting area of the UST could fully cover the imaging window, effectively capturing most PA/US signals reflected from a rod mirror. The imaging results of the tungsten wire phantom suggest that the proposed coaxial catheter is capable of detecting the targets over a longer range of distance, despite exhibiting the lower optical fluence in comparison to non-coaxial designs. The conclusion is supported by *ex-vivo* imaging results, demonstrating superior imaging depth of the coaxial catheter. The improved performance and reduced size of the coaxial IV-PAE catheter benefit both plaque evaluation and molecular imaging applications,

which bring us closer to clinical implementation.

In this chapter, the conventional piezoelectric material (PZT ceramic) is used to fabricate the ring-shaped UST, which is a critical component in developing the coaxial IV-PAE catheter. This method can also be applied on developing the coaxial PAE catheter. However, it is worth noting that the miniature center orifice of the ring-shaped UST poses limitations on some applications that require big optical apertures, such as the Bessel beam. Expanding the dimensions of center orifice may compromise UST sensitivity. In the subsequent chapter, a novel UST based on transparent piezoelectric material will be developed, which serves a key component in the fabrication of GI-PAE catheter.

Chapter 3 Transparent Photoacoustic (PA) Probe

The performance of ring-shaped UST has been demonstrated in the last chapter. However, its miniature center orifice presents limitations for some applications requiring big optical apertures, such as the Bessel beam. Before proceeding with the development of the coaxial GI-PAE catheter, a novel transparent ultrasound transducer (TUST) will be investigated and tested.

The TUST is an innovative approach[93, 94] in PAI based on transparent piezoelectric materials to enhance optical efficiency for laser beam transmission, facilitating the structures of imaging system and probe. To verify the imaging performance, a TUST fabricated using lithium niobate (LN) single crystal will be studied and fabricated in this chapter.

3.1 Development of Transparent Ultrasound Transducer (TUST)

3.1.1 Recent Research of TUST in Photoacoustic imaging (PAI)

In recent years, some TUSTs have been developed to combine the US and optical beams coaxially[94], offering flexible solutions on the PAM, including the quadruple modalities[95]. Among transparent piezoelectric single crystals[44], LN[93, 95-97] has commonly been selected for TUST fabrication. However, challenges still exist in the

development of miniature PA probes: (1) The outer diameters of most reported PA probes were ~1 cm. A conductive glue was needed to connect the electrical wires to the LN wafer, which adversely affects the transparency of TUST. High-frequency USTs, with a smaller aperture, allow less space for electrical connections, making fabrication more difficult. (2) Transparent electrodes of TUTs is commonly indium tin oxide (ITO), coating on LN wafers. While thinner ITO coatings provide better transparency, they also exhibit higher electrical resistance, resulting in inefficient operation. (3) In the reported work, laser focusing lenses were separated from the TUST, requiring an external mount for coaxial fixation and adjustment. Consequently, this setup leads to bulky PA probes, limiting their applications, especially those requiring compact and portable setups, such as *in-vivo* PA flow cytometry and wearable PAM.

3.1.2 Fabrication of Transparent Ultrasound Transducer (TUST)

A 10 mm × 10 mm LN wafer (Shanghai Bontek Optoelectronic Technology Development Co. Ltd, China) was ordered and polished to 75 μm. 150 nm-thick ITO coating was then applied on both surfaces of LN wafer as electrodes. As the piezoelectric layer of the TUST, the ITO-coated LN wafer was cut into small pieces with dimensions of 2 mm × 2 mm. Figure 3.1 shows the schematic and photo of the TUST. The TUST only weighs 0.295 g, which is very tiny and light, shown in Figure 3.1c.

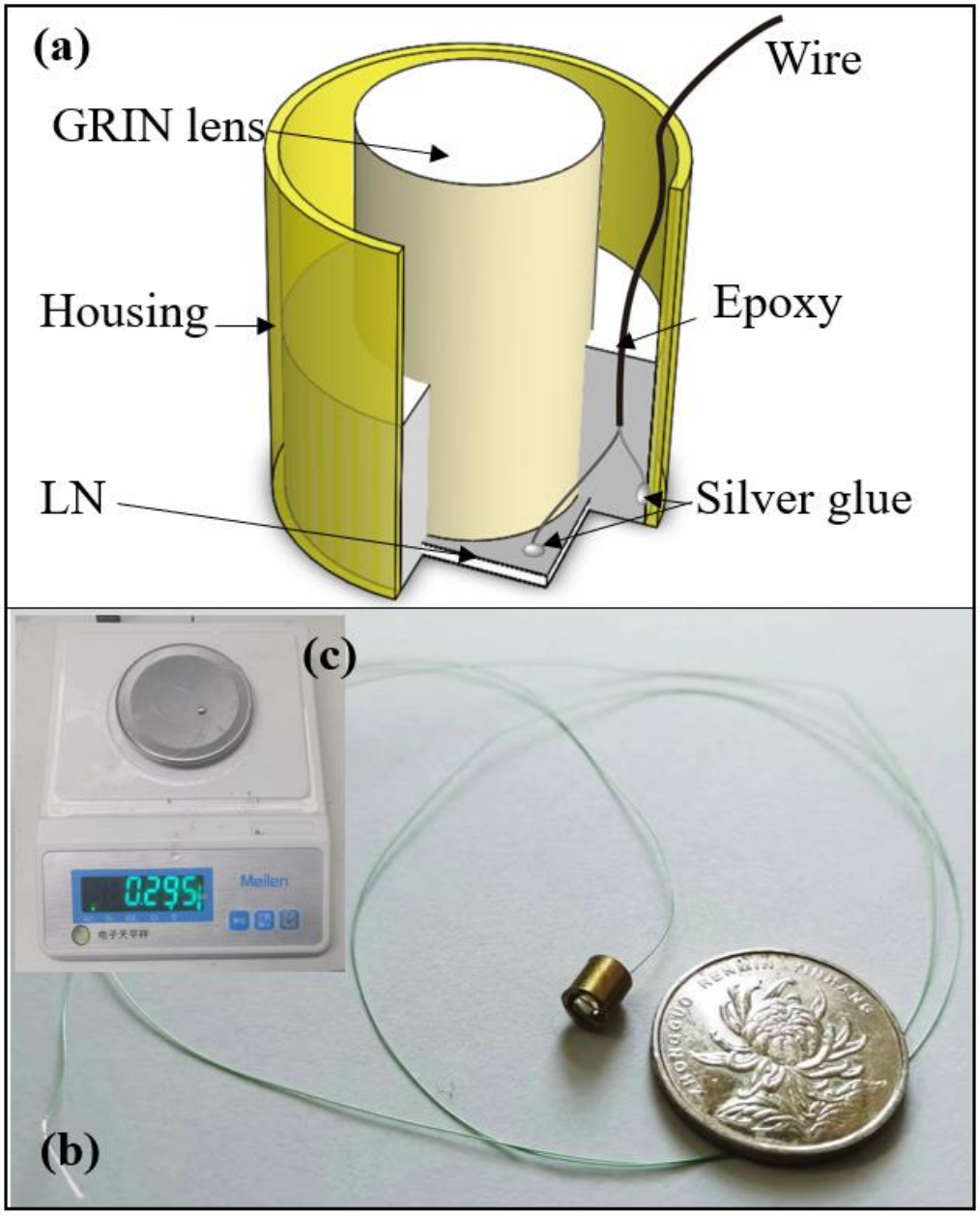

Figure 3.1 Schematic and photo of the TUST based on LN wafer and GRIN Lens as a backing layer. (a) Structure of the TUST. (b) Photo of the TUST comparing with a coin. (c) The TUST measured on the scale.

To fabricate the TUST, first of all, the LN wafer and the brass housing were aligned coaxially on a glass substrate using wax. A GRIN lens (GRIN2906, Thorlabs, USA) was adhered with the LN wafer using epoxy (301, Epoxy Technology Inc., USA), to serve as both a backing layer and an optical lens for proving the transducer's sensitivity

and laser beam quality simultaneously. Secondly, silver glue was used to attach the positive electrode to the backside of the LN wafer, while the negative electrode was attached to the inner wall of the housing. All the movable components were then fixed in place using epoxy. Finally, after the epoxy was cured, the silver glue was applied to electrically connect the front side of the LN wafer with the housing. Figure 1(b) illustrates the size of the TUST compared with a coin.

3.1.3 Optical Transmission Efficiency

The optical transmission efficiency serves as a key parameter to evaluate a transparent ultrasonic transducer, which can be calculated by the ratio of output laser energy to input laser energy. To investigate the performance of the LN wafer, a pulsed OPO laser (EKSPLA, NT242, Lithuania) was employed to offer energy in the experiment measuring optical transmission efficiency. A laser power meter (PE9-C, Ophir, Israel) was applied to measure both incident and transmitted laser spots at the wavelength interval of 25 nm. As shown in Figure 3.2, the optical transmission of the LN wafer employed in the TUST exceeds 60% across the wavelength range from 450 nm to 1200 nm, which makes it adaptable for various applications using multi-wavelengths.

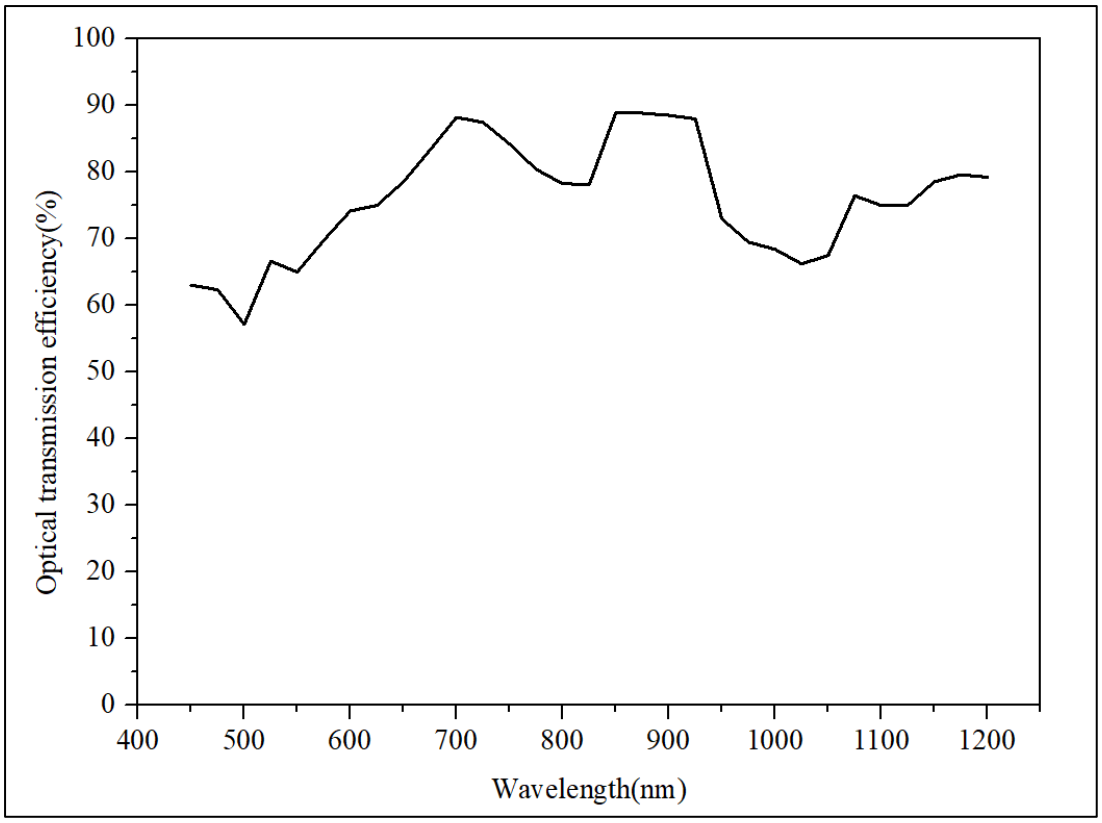

Figure 3.2 Optical transmission efficiency of a LN wafer tested by the laser in the range of 450 – 1200 nm.

3.1.4 Pulse-echo Test

The pulse-echo test was conducted to show the sensitivity and frequency range of the TUST. The US signals were received by the pulser/receiver (5073PR, Olympus, Japan) and then displayed on a digital oscilloscope (DSOX2012A, Keysight, USA). An impedance analyzer (4294A, Agilent Tech., USA) was applied for dielectric and electrical impedance measurements at room temperature. Figure 3.3 shows the pulse-echo and fast Fourier transformation (FFT) results of the TUST without gain, indicating that the measured center frequency of the TUST was ~46.9 MHz with a -6 dB bandwidth of 29.4%.

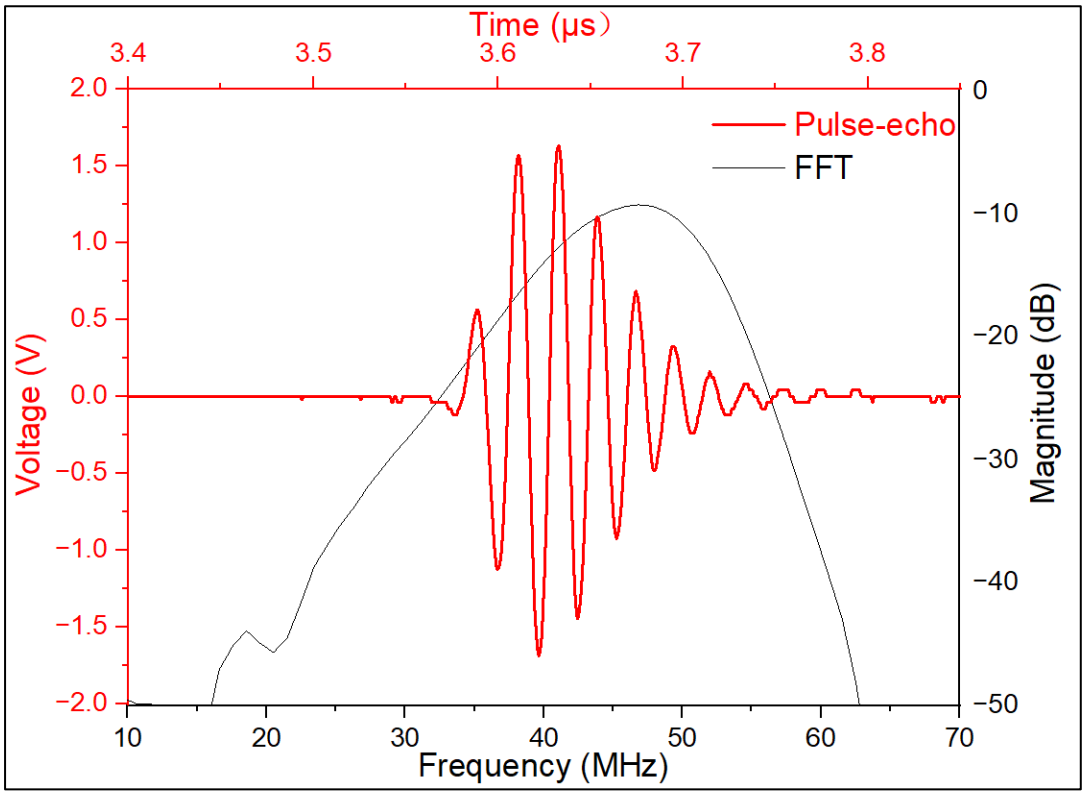

Figure 3.3 Pulse-echo result and FFT spectra of the TUST.

As shown in Figure 3.4, the developed TUST exhibits a resonant mode even after incorporating the GRIN lens to load the piezoelectric layer. The resonant frequency (f_r) was measured as ~41.3 MHz with an electrical impedance of 78 Ω, which was close to the desired electrical impedance (50 Ω). The slightly higher electrical impedance may be caused by the imperfect electrical behavior of ITO electrodes.

With the anti-resonant frequency (f_a) of 47.2 MHz, the effective electromechanical coupling coefficient (k_{eff}) can be calculated by the following equation:

$$k_{\text{eff}} = \sqrt{1 - \frac{f_r^2}{f_a^2}} \tag{3.1}$$

The k_{eff} of the TUST was calculated to be ~0.48, which is comparable to that of the reported TUST[93] fabricated using the LN wafer as the piezoelectric material.

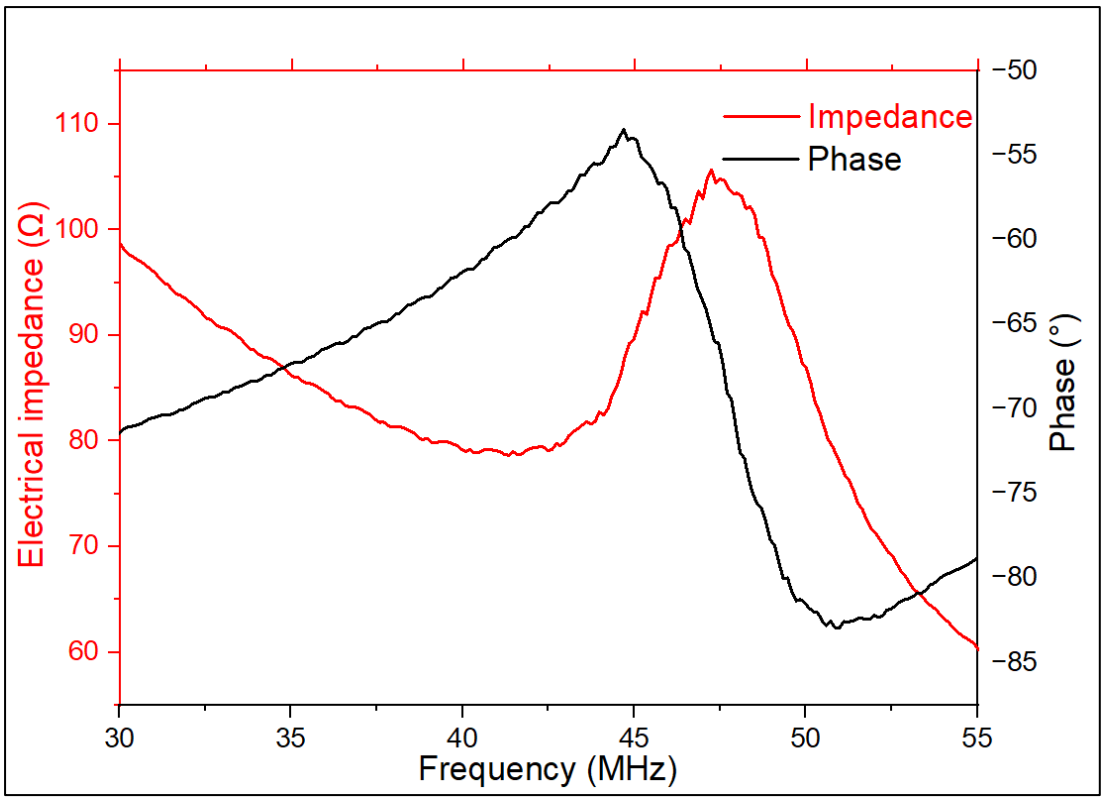

Figure 3.4 Impedance/phase frequency spectra of a TUST with a GRIN lens as a backing layer.

3.2 Performance Test in Different Applications

3.2.1 Resolution Test

The PAI resolution depends on the dimensions of the laser spot, which is much smaller than the US detection region. In this work, the blade-edge method, widely used as a standard method for Gaussian laser beam characterization, was used to measure the dimensions of the laser beam. A sharp blade edge was employed and imaged by the PA probe equipped with the proposed TUST. When the laser spot from the probe scanned across the blade edge, variations of PA signals were recorded that was attributed to the changes in energy density. These variations allowed for the characterization of the beam profile based on the PA signals.

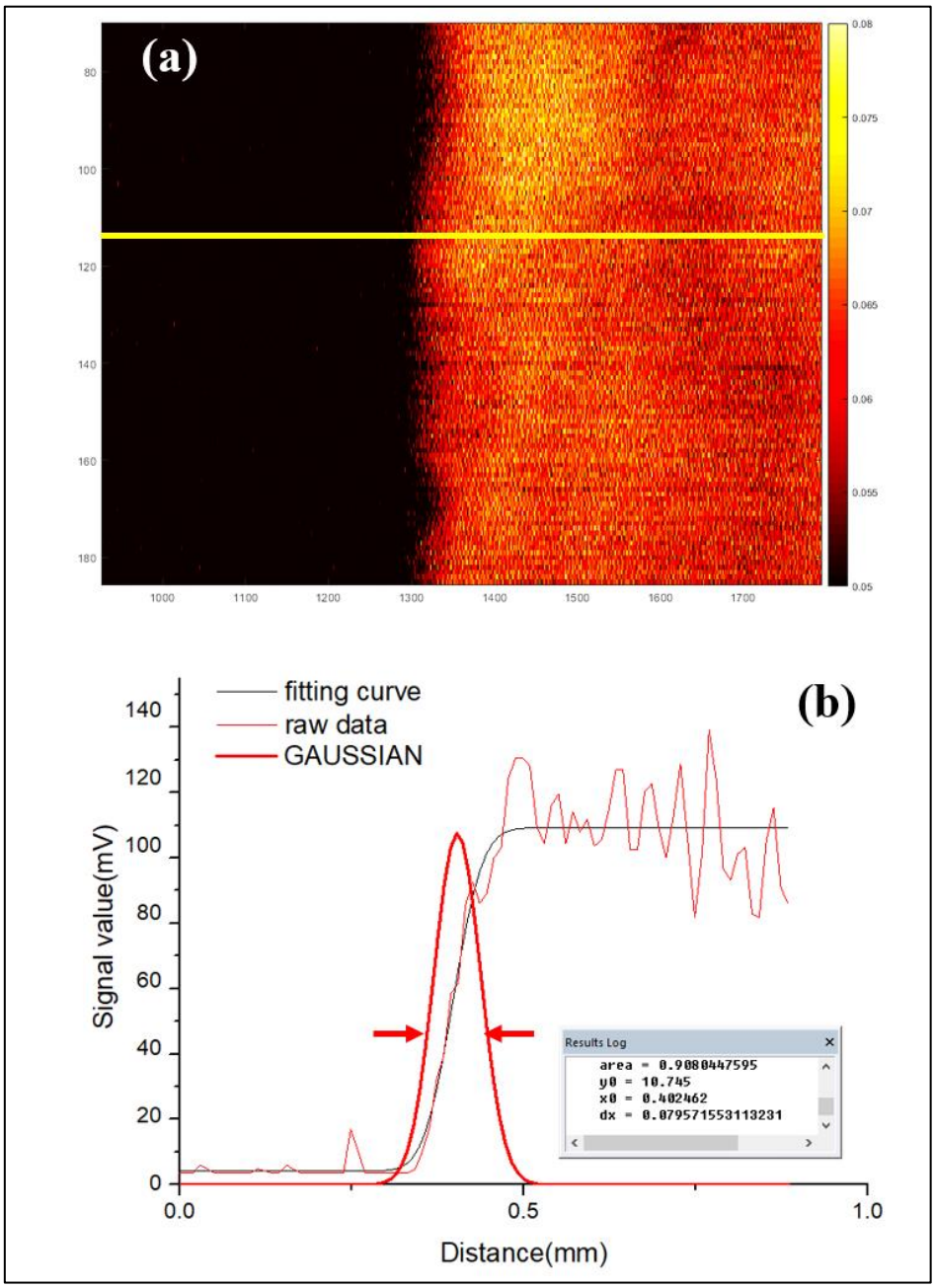

Figure 3.5 Results of resolution test. (a) PAI of the blade edge. (b) PA signal along the yellow line in (a) and the measured resolution.

Figure 3.5 displays the resolution results. Figure 3.5(a) is the PAI of the blade edge and Figure 3.5(b) shows the raw PA data along the yellow line shown in Figure 3.5(a). The fitting curve is the edge spread function (ESF) of the raw data. The Gaussian-like curve corresponds to the line spread function (LSF) in the scanning direction, derived from

the first-order derivative of the ESF. The calculated data in the box, automatically generated using software (Origin2021), shows that the full width at half maximum (FWHM) resolution was ~80 μm.

3.2.2 Imaging Setup

A 532-nm pulsed laser (Medical Technology Co., Ltd, Shenzhen, China) was employed to deliver the irradiation energy. The laser beam travelled through an iris (ID8, Thorlabs, USA) and a beam expander (EX-532-2X-A, Sanke, China), was coupled into a single-mode fiber using an objective (PLAN 4X, Shangguang, China). The single-mode fiber (SMPF0106, Thorlabs, USA) with a pigtailed ferrule was applied for laser delivery. The laser energy offered from the TUST was ~1 μJ. A ferrule sleeve (51-2800-1800, Thorlabs, USA) was then used to align the GRIN lens and the pigtailed ferrule of the fiber coaxially. The PA signals from phantoms were detected by the TUST and then sent to the US pulser/receiver, finally digitized, and processed by a DAQ board (ATS9371, Alazar Tech, Canada) in the computer. The schematics of the PA system, TUST and experiment setups for performance evaluation are exhibited in Figure 3.6.

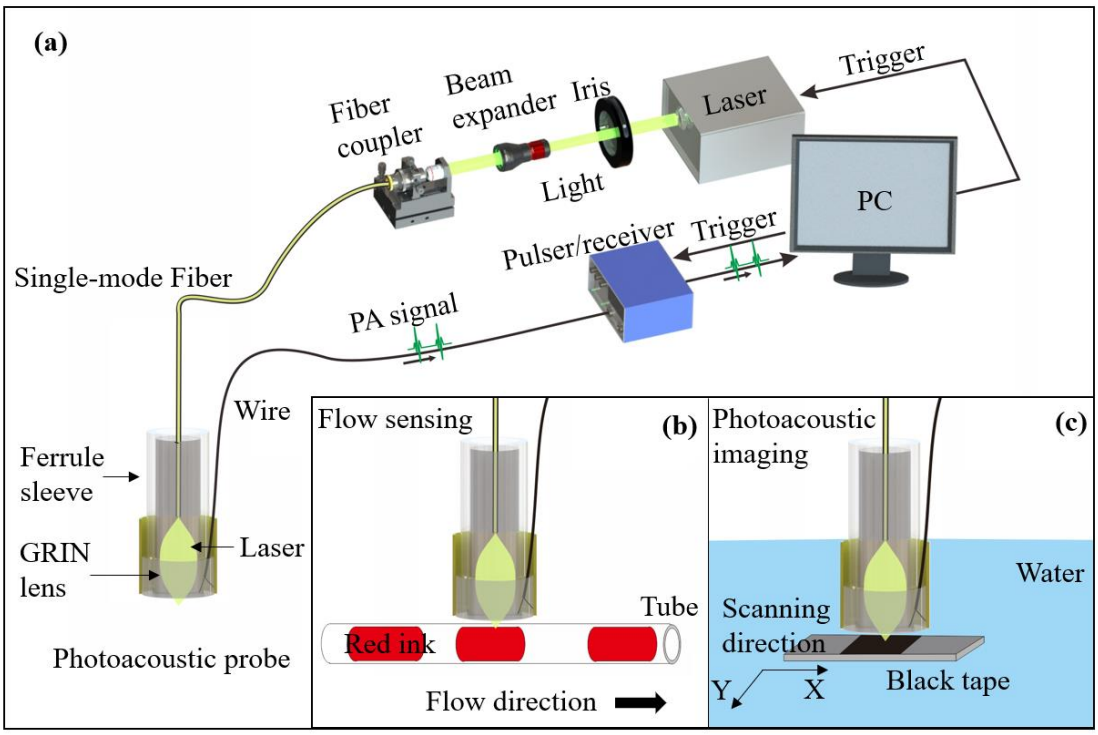

Figure 3. 6 Schematics of a PA system with a TUST and experimental setups. (a) A system with the PA probe; (b) Setup for flow sensing; (c) Setup for PAI.

3.2.3 Coaxial Photoacoustic (PA) Probe for Flow Sensing

3.2.3.1 Phantom Preparation for Flow Sensing

To exam the performance of the coaxial PA probe on single-point detection, flow sensing experiments were conducted using a red ink in a tube, mimicking the blood flow in the vessel. Given that blood has high optical absorption in the visible spectrum, the red ink should show to have high optical absorption at the wavelength of 532 nm to demonstrate the design rationale of the phantom. The absorption coefficient of the red ink was tested using a spectrophotometer (PerkinElmer Lambda 750, USA). As shown in Figure 3.7, the absorption spectrum of the red ink shows an optical absorption peak at 521 nm, closely aligning with the laser wavelength (532 nm) employed in the present work.

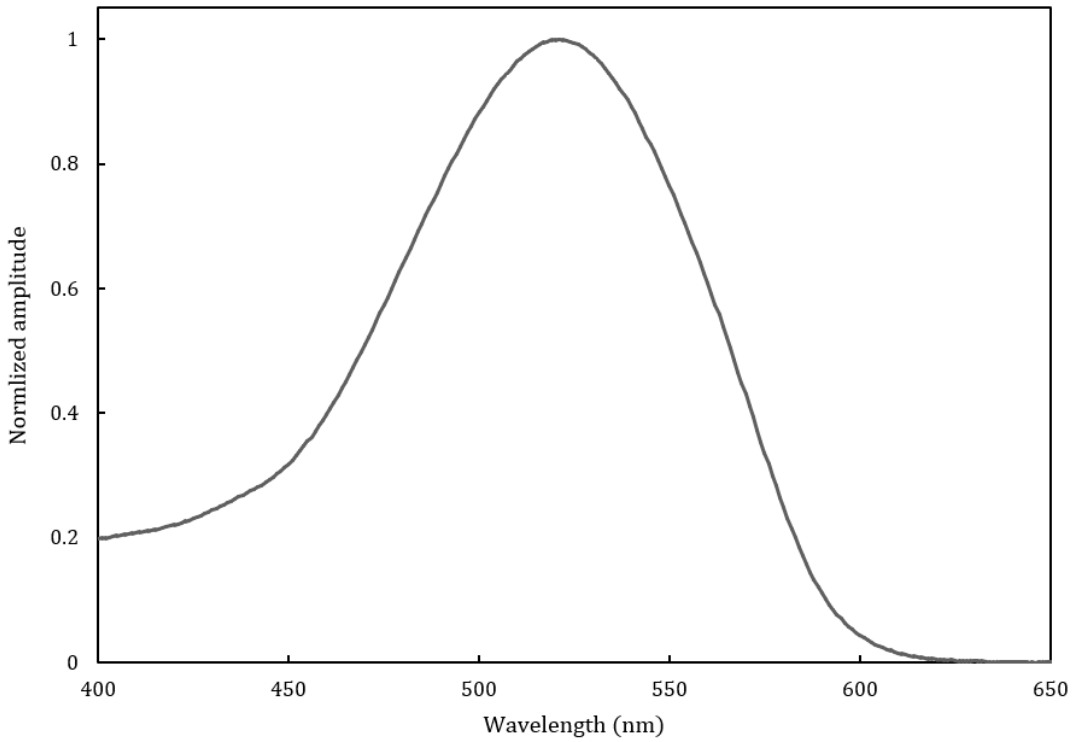

Figure 3.7 Absorption spectrum of the red ink used for flow sensing test.

3.2.3.2 Flow Sensing Test

Figure 3.8 shows the sensing performance of the coaxial PA probe. Figures 3.8(a) and (b) are the photos of the experiment setup and phantoms including red ink in a polyethylene (PE) tube. Figure 3.8(c) shows the B-scan PA signals captured from the flowing red ink over time, containing a dataset spanning 14 seconds (3500 A-lines). The red curve represents the signal amplitude profile at the white dashed line. The signal fluctuation is caused by the laser energy shift. To match the flow speed (20 mm/s) of the red ink, the laser repetition rate was set to 250 Hz based on the PA lateral resolution (~80 μm) of the probe. The results indicate the capability of the coaxial PA probe to distinguish between the air gap and the continuous flow of red ink.

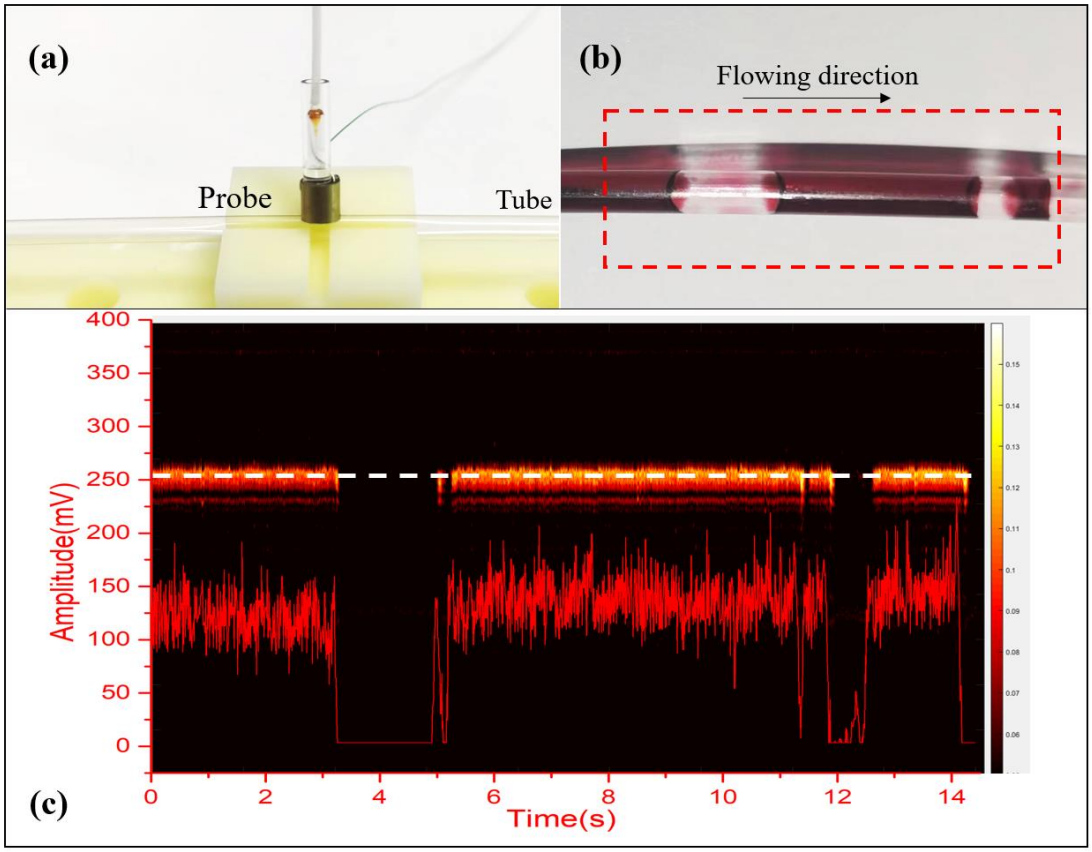

Figure 3.8 Photos and PA sensing/imaging results of phantoms. (a) Photo of an experiment setup; (b) photo of flowing red ink in a PE tube; (c) PA signals and the signal amplitude profile captured from the flowing red ink in a tube. The red curve represents the PA signal amplitude profile at the white dashed line.

3.2.3.3 Long-term Stability Test

Flow sensing is commonly employed for the continuous monitoring of circulating tumor cells (CTC), which requires long-term detection capabilities. To evaluate the long-term stability of the coaxial PA probe, a test was conducted using flow sensing. Red ink in a PE tube was employed again to mimic the blood flow conditions.

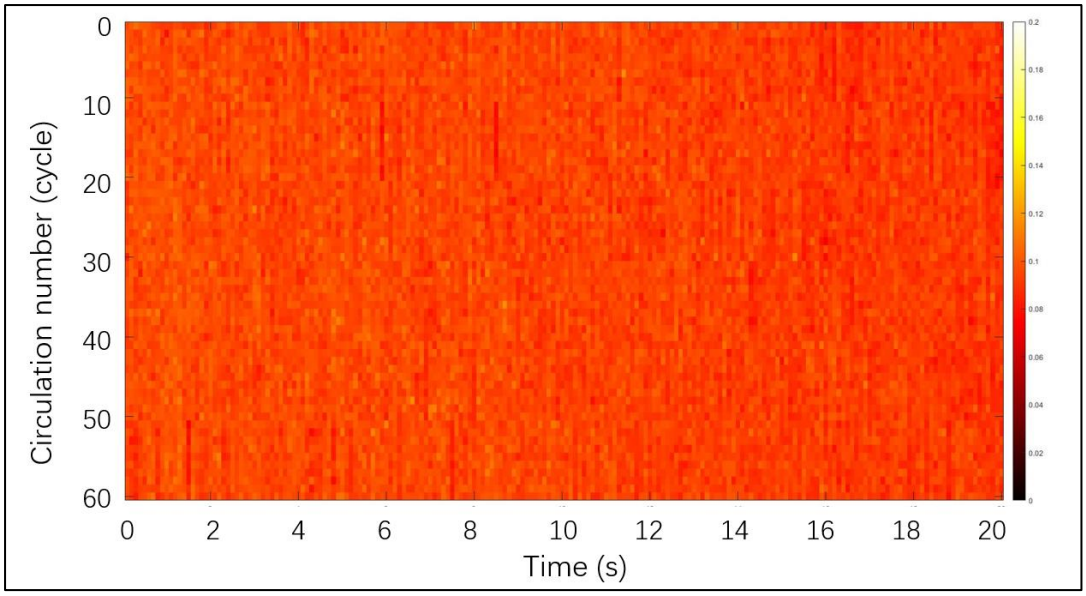

Figure 3.9 Result of long-term flow sensing.

Considering the blood circulation time in the human body that is ~20 seconds, a 20-minute detection period of red ink flow was conducted to mimic the surveillance of ~60 cycles of blood circulation. The irradiation laser operated at a wavelength of 532 nm, with a repetition rate of 10 Hz and an energy output of 1 μJ. Subsequently, the PA signal generated from the flowing red ink was processed. Figure 3.9 shows the maximum amplitude of each A-line signal in every cycle, displaying the signal fluctuation detection mainly caused by the variations of laser energy. The data average was calculated as ~0.0941, with the standard deviation of ~0.0054. According to the equation:

$$C_v = \frac{\sigma}{\mu} \tag{3.2}$$

where C_v is the coefficient of variation, σ is standard deviation, and σ is average number. The coefficient of variation is calculated as ~5.7%, showing a good long-term detection stability of the proposed probe.

3.2.4 Coaxial Transparent Photoacoustic Probe for Imaging

Figure 3.10 exhibits the imaging results acquired by the PA probe. Figures 3.10(a) and (c) are the photos of a black tape and graphite rods placed on a glass slide. Figures 3.10(b) and (d) demonstrate the maximal amplitude projection (MAP) image of both targets. The phantom experiments suggest that the proposed transparent PA probe is applicable for dynamic imaging on clinical research.

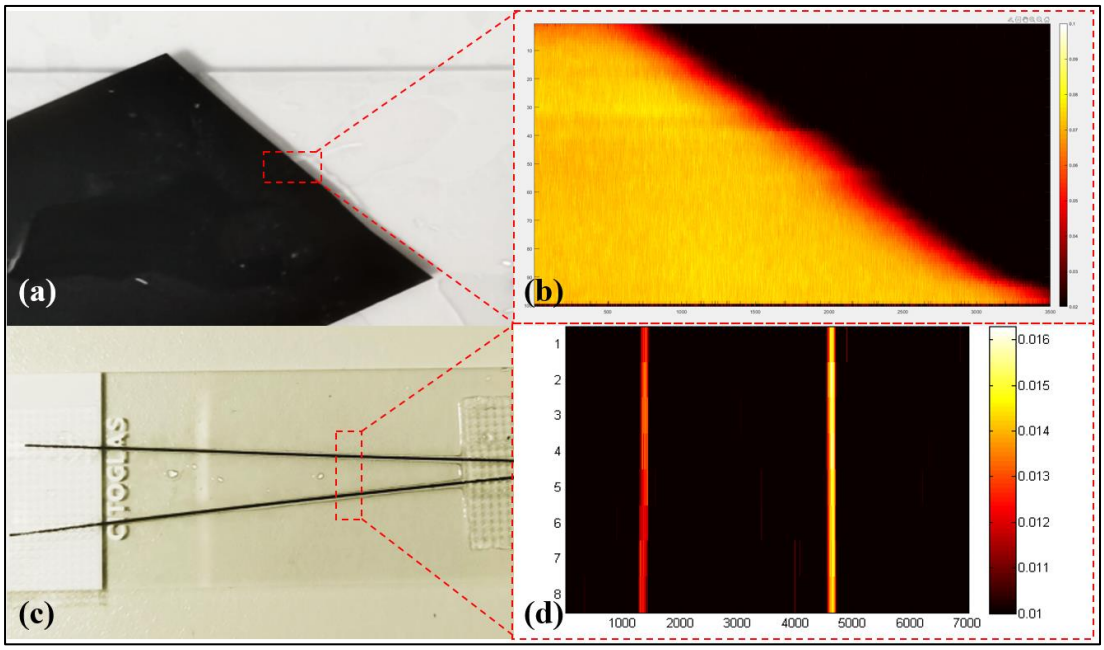

Figure 3.10 Photos and PAI results of phantoms. (a, c) Photos of a black tape and graphite rods. (b) PA MAP image of a black tape. (d) PA MAP image of the graphite rods.

3.3 Discussion

The miniaturization and simplification of imaging devices are conducive to clinical implementation. The transparent PA probes reported in literature were mostly with centimeter-scale dimensions, which limited their applications in confined spaces. However, reducing the aperture size of the LN wafer could probably degrade the TUST

performance, such as sensitivity. The research gap can only be filled by modifying the probe design and the fabrication process of UST.

Here we also compare the performance of the proposed TUST with the previous works using the same piezoelectric material (LN) in Table 3.1, showing its strengths in material dimensions, maximal diameter, and center frequency. Its bandwidth (BW) and optical transmission efficiency are also comparable to values reported in previous studies.

Table 3.1 Comparison of TUST parameters in different studies.

Material	***Wafer size (mm)***	***Probe diameter (mm)***	***Optical transmission efficiency (%)***	***Center frequency (MHz)***	***-6 dB bandwidth (%)***	***Reference***
LN	2.5 × 2.5 & 10 × 10	N/A	~80 (690 – 970 nm)	14.5	30	[96]
LN	10 × 10	15	90 (Visible range)	36.9	33.9	[93]
LN	7 × 7	14	66 (690 – 910 nm)	11.2	23	[97]
LN	Φ9	9	74 (630 nm)	7.5, 31.5	N/A	[95]
LN	**2 × 2**	**4**	**57 – 89** (450 – 1200 nm)	**46.9**	**29.4**	**This Section**

To achieve the balance between optical transmission efficiency and electrical resistance, the ITO thickness should be designed and optimized. After several tests, different thicknesses of ITO were studied in terms of electrical properties with 150 nm as the optimal thickness. It should be noted that, to reach the desired relatively low sheet resistance (~40 ohm cm), low power was applied for a long period during the sputtering

of ITO.

To further minimize the probe dimensions, the GRIN lens and the LN wafer were combined as a whole. The GRIN lens is an essential optical element for beam shaping. Epoxy (301) was employed as adhesion between the GRIN lens and the LN wafer. The air trapped in the epoxy could be removed by a vacuum machine or by gently pressing the lens on the LN wafer before the epoxy curing process.

Two major types of fiber are commonly applied for laser delivery: the single-mode fiber offers a smaller spot, while the multi-mode fiber offers higher laser energy. Both share the same packaging. Thus, we chose the single-mode fiber to demonstrate the design. Equipped with a pigtailed ferrule, the fiber facilitated aligning with the GRIN lens coaxially using a ferrule sleeve. This design allows for the ease substitution of the optical fiber to meet various requirements of imaging applications.

The miniature transparent PA probe was designed for various applications, especially in limited spaces such as a flow cytometer. An ideal flow cytometer should be portable, allowing placement on tissue to detect blood and target cells in the subcutaneous vessels. Consequently, the required probe should be compact and lightweight enough to be easily attached on hand or arm. To evaluate the performance of the probe as a flow sensor, red ink and tube were applied to mimic blood and vessels, respectively. The PA

signals generated by red ink and air bubbles could be easily identified (Figure 3.8(c)). While for dynamic imaging, the proposed probe could effectively image the graphite rods and the edge of black tape as PAM. All the imaging results suggested that the transparent PA probe was capable of performing various functions such as flow cytometer and PAI.

Although the results present the feasibility and potential of the transparent PA probe, there is still some room to further improve the performance. Firstly, as a miniature TUST, the narrow bandwidth remains a common issue due to the limited selection of transparent materials for backing and matching layers. To retain the optical transmission efficiency of the TUST, parylene was not deposited in this work. However, the multi-matching layer scheme should be studied and implemented to improve the bandwidth. Secondly, the GRIN lens could not absorb the US wave from the back of the LN wafer, such that the acoustic echo signals and corresponding images would be adversely affected by US reflections. A GRIN lens with an extended length could mitigate the issue by shifting unwanted acoustic reflections out of the US imaging range. Last but not least, the mechanical scanning speed limits the potential of the proposed probe especially for the application of PAM. Optical scanning method, such as fiber bundle or galvo scanning system, could speed up the imaging, which should be studied in the future.

3.4 Conclusion

To sum up, a miniature PA probe based on a 4-mm diameter TUST was successfully designed and fabricated, with dimensions smaller than the previous LN-based TUSTs in the reported work. For the first time, the innovative application of a GRIN lens as the backing layer of the TUST effectively shrank the entire probe size. The proposed probe featured a high center frequency of 46.9 MHz and a -6 dB bandwidth of 29.4%. Experiments were further performed on the phantoms to demonstrate the potentials in fluid flow sensing and PA imaging applications.

In this chapter, the novel TUST is investigated and fabricated, which is an important component for the development of coaxial PAE catheter. In the next chapter, a new coaxial GI-PAE catheter based on the proposed TUST and Bessel beam will be studied and developed.

Chapter 4 Coaxial Gastrointestinal Photoacoustic Endoscopy (GI-PAE) Based on Bessel Beam

To reach a high resolution, the laser emitted from the GI-PAE catheter is generally designed as a Gaussian-like focused beam that has a short depth-of-field (DOF). However, this kind of laser beam is difficult to adapt to the irregular surface within the GI tracts of animals, not to mention about the human proportions. Therefore, it is necessary to develop a novel GI-PAE catheter equipped with a long DOF laser beam. In this chapter, a type of diffraction-free laser beam, Bessel beam, will be introduced and applied in the coaxial GI-PAE catheter.

4.1 Fabrication of Coaxial Photoacoustic Endoscopic Catheter

4.1.1 Design of Bessel Beam

As a non-diffracting beam, a Bessel beam (shown in Figure 4.1) can propagate indefinitely without changing its cross-sectional intensity profile, which follows the square of a zero-order Bessel function of the first kind[98, 99]. In a zero-order beam, a central bright spot (Figure 4.1(a)) is evident, while in a high-order beam, a central dark area is observed (Figure 4.1(b))[100]. As shown in Figure 4, the white lines indicate the energy distribution. Leveraging the unique property of the zero-order Bessel beam, our approach is to design a GI-PAE catheter with an extended DOF.

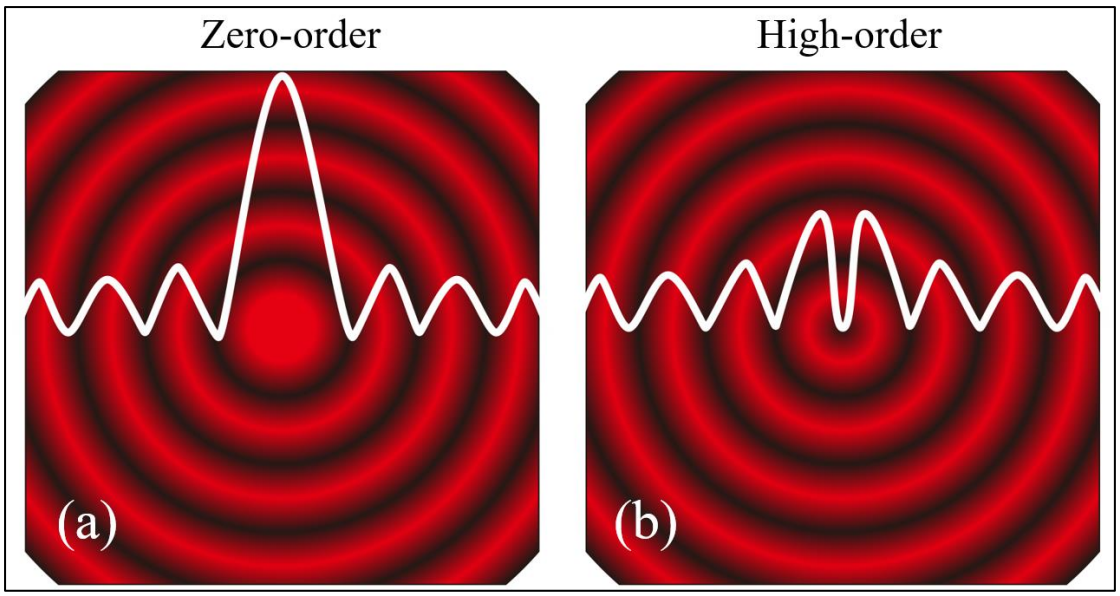

Figure 4.1 Schematic diagrams of Bessel beam. (a) Zero-order Bessel beam; (b) High-order Bessel beam. White lines represent the energy distribution.

A GRIN lens and an axicon lens (Femto Technology Co, Ltd, Xi'an, China) are both custom-made to form the Bessel beam. The GRIN lens serves to collimate the laser beam emitted from the fiber, and the axicon lens generates the Bessel pattern. Simulations are done based on the actual dimensions, taking into account the considerations of processing difficulty and precision. The software ZEMAX is utilized to simulate the laser beam travelling through the lens, resulting in the formation of a Bessel beam in both air and water. Figure 4.2 presents the simulation results, showing that the Bessel beam has focus lengths of ~15 mm in air and ~25 mm in water. The designed Bessel beam features a small center spot across a wide range from the lens.

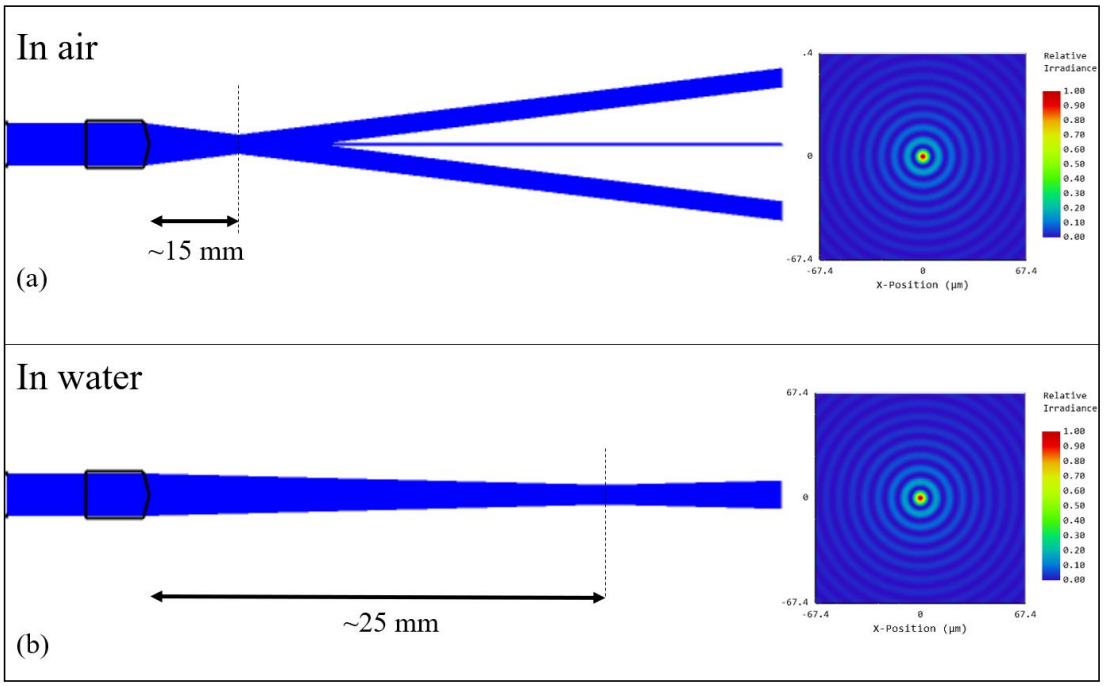

Figure 4.2 Simulation results of Bessel beam travelling in different media. (a) Simulation in air; (b) Simulation in water.

To further evaluate the Bessel pattern, a charge-coupled device (CCD) camera is applied to detect the laser beam at various distances in air. The distinct Bessel beam is clearly visible as shown in Figure 4.3. Figures 4.3(a), (b) and (c) illustrate the appearance of the laser beam at different distances from the cone lens to the CCD camera. As the distance increases, more ripples emerge, distributing the laser energy from the center spot. To confirm the energy loss, the laser beam is monitored by a laser power meter (PE9-C, Ophir, Israel), showing stable energy across a large distance from 1 mm to 15 mm, as presented in Figure 4.3(d). This result is consistent with the simulated results, confirming the efficacy of the designed Bessel beam.

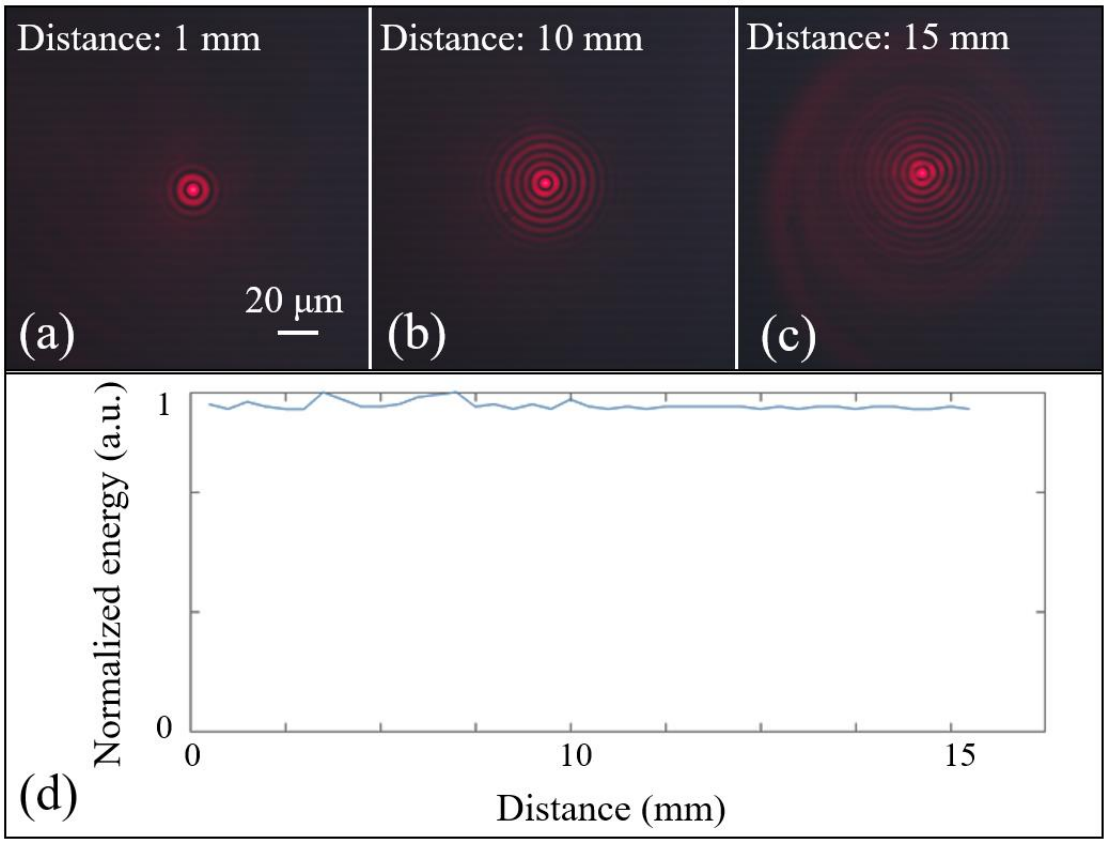

Figure 4.3 Energy evaluation of Bessel beam in air. (a – c) Photos of Bessel beam imaged by a CCD camera with a scalebar of 20 μm; (d) Energy test from 0 mm to 15 mm.

4.1.2 Structure of Gastrointestinal Photoacoustic Endoscopic Catheter

The coaxial GI-PAE catheter, as exhibited in Figure 4.4, incorporating the LN-based TUST is developed to detect both PA and US signals reflected from a mirror. A single-mode fiber (P1-SMF28Y-FC, Thorlabs, USA) with a 9-μm fiber core is applied to deliver the 532-nm laser. A GRIN lens and an axicon lens are custom-made to form the Bessel beam. All the components are aligned in a stainless-steel housing. The laser beam and UST detection area are coaxially arranged to maximize the optical-acoustic overlapped area.

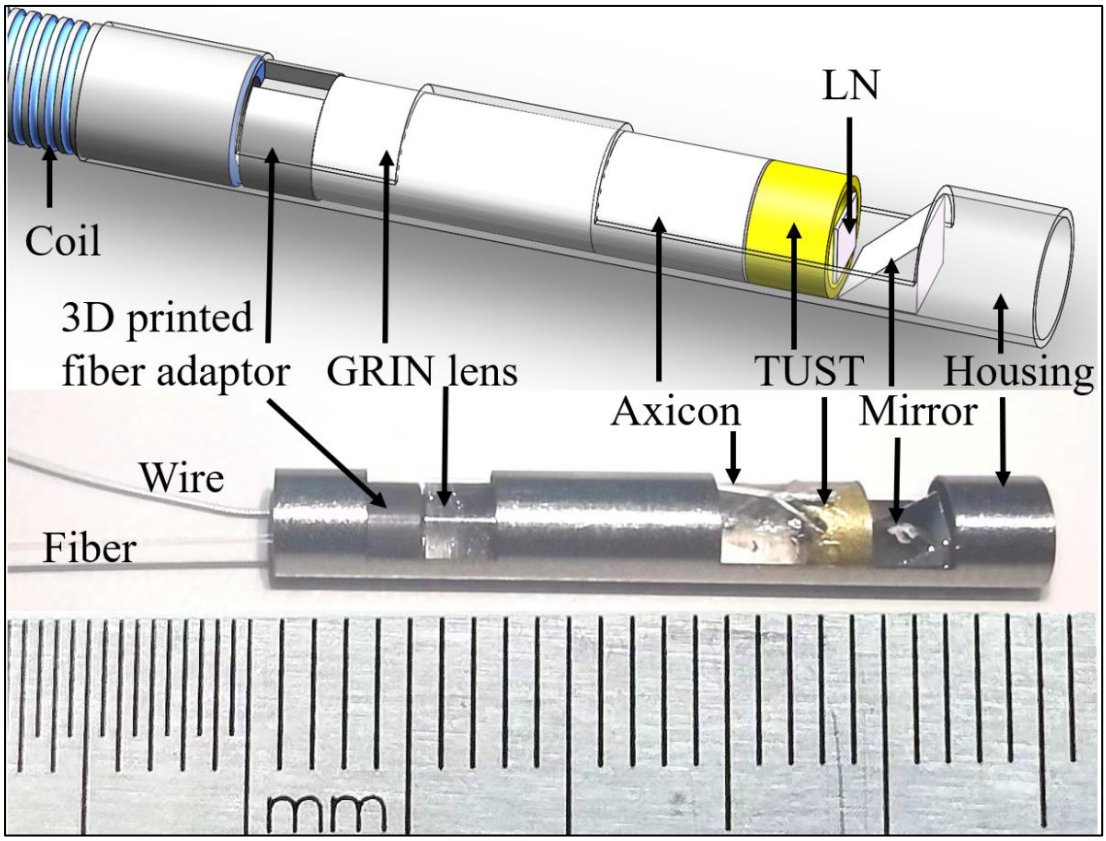

Figure 4.4 Schematic and photo of a GI-PAE catheter. The housing of the catheter is 25 mm, measured by a ruler.

4.2 Performance of the Coaxial Catheter

4.2.1 Pulse-echo Test of Transparent Ultrasound Transducer (TUST)

To evaluate the TUST performance, pulse-echo tests were conducted on the LN-based transducers. An LN wafer, with dimensions of 1.6 mm × 1.6 mm and a thickness of 150 μm, was employed to fabricate the TUST. Both surfaces of the LN wafer were coated with 50 nm-thick ITO layers. Generally, the UST consists of a matching layer, piezoelectric layer and backing layer. In TUST, the backing layer is usually made of transparent epoxy (301, Epoxy Technology Inc., Billerica, MA, USA), which would generate microbubbles during curing, affecting the light delivery. The matching layer

of TUST was made of Parylene coating, which reduces the transparency of the TUST. In light of maximizing the laser energy, the TUST used for GI-PAE was fabricated without backing layer and matching layer to keep the optical transmittance. Figure 4.5 demonstrates the pulse-echo and FFT spectra of the proposed TUST. The center frequency of the TUST was 20.5 MHz, while its bandwidth was ~12% due to the absence of matching and backing layers.

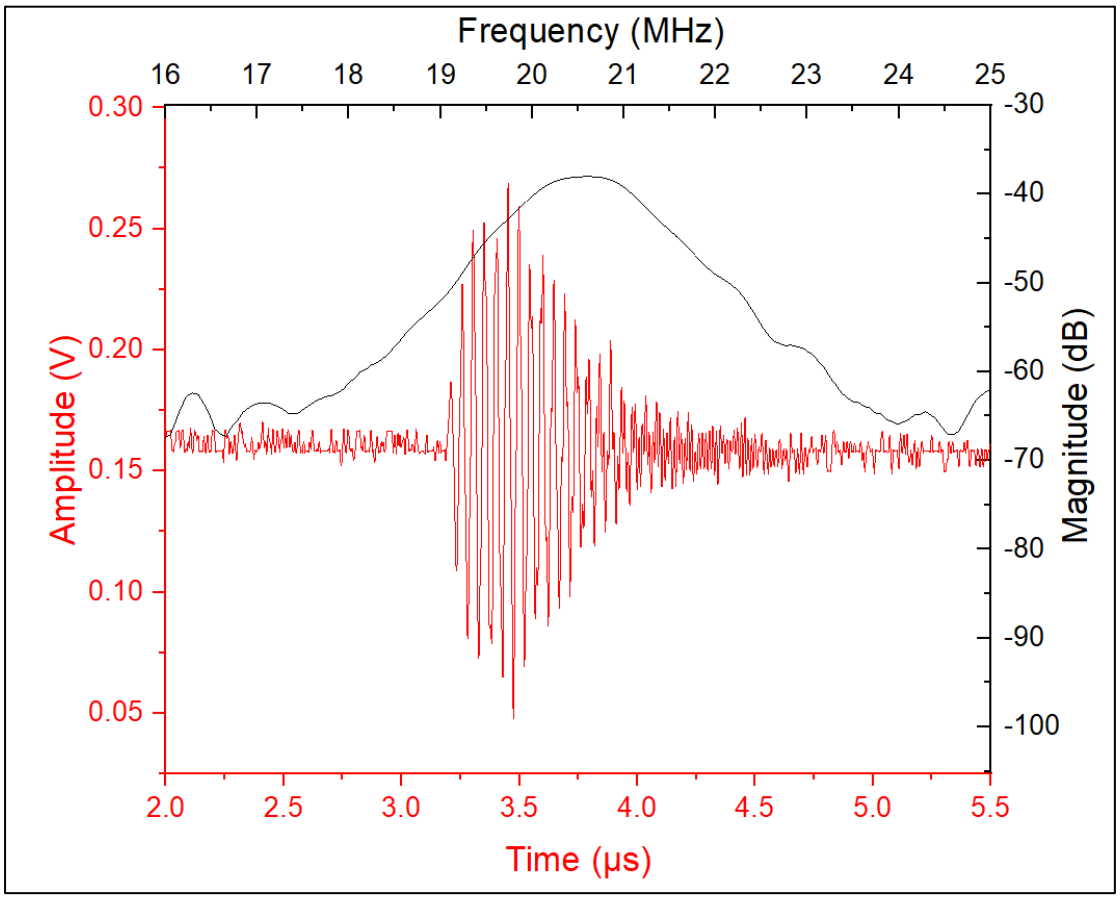

Figure 4.5 Pulse-echo and FFT spectra of a TUST without backing and matching layers. The bandwidth is ~12%.

4.2.2 Resolution Test of Coaxial Gastrointestinal Photoacoustic Endoscopic (GI-PAE) Catheter

In the actual detection, the laser beam travels through the LN wafer of the TUST, being reflected by the mirror. Considering the distance from the TUST surface to the imaging window is ~2.25 mm, the resolution test starts at 2.5 mm. Figure 4.6 exhibits the configuration of the resolution test. To enhance the performance evaluation of the Bessel beam, the mirror was removed during phantom imaging. As shown in Figure 4.6(c), the laser beam propagates with a good Bessel pattern in water.

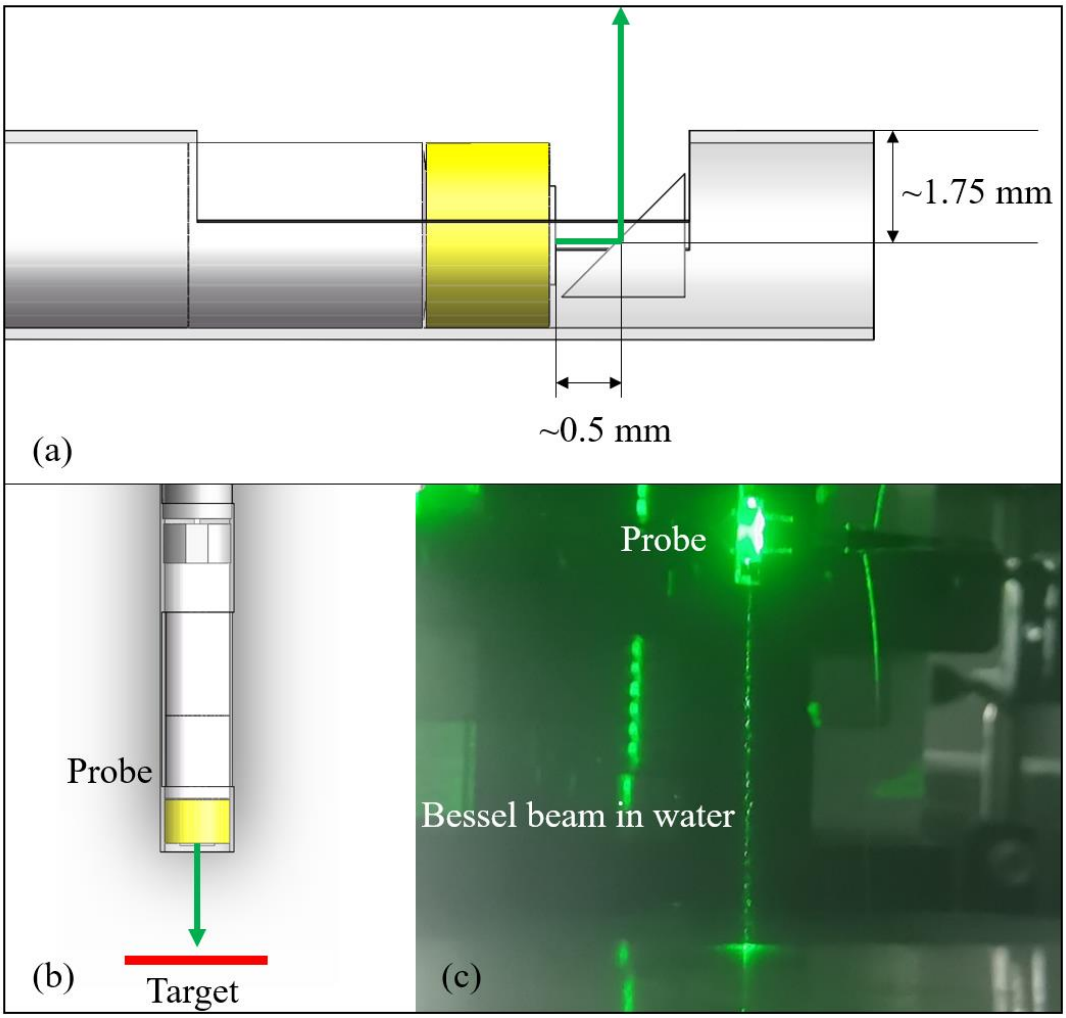

Figure 4.6 Configurations of the resolution test. (a) Schematic of the laser beam in the catheter; (b) Schematic of the imaging probe without a mirror; (c) Photo of the probe and Bessel beam in a water tank.

The PA signals almost originate from the center spot of the Bessel beam, where distributes most of the energy. The resolution of the coaxial GI-PAE catheter is evaluated by the blade-edge method at different depths, presented in Figure 4.7. Raw data is fit by the function of Boltzmann Fitting to generate the ESF, which is differentiated to obtain the LSF. The FWHM of the curve is calculated automatically using the software (Origin 2021). Considering a scanning step of 2 μm, the lateral PA resolution varies from 29.8 μm to 18.1 μm (shown in Table 4.1) across imaging depths from 2.5 mm to 4.5 mm. However, the resolution deteriorates to 136.2 μm at the depth of 5 mm due to weak PA signals mixing with the noise. This is attributed to the degraded sensitivity of the TUST in long distances, coupled with the signal attenuation over long distances.

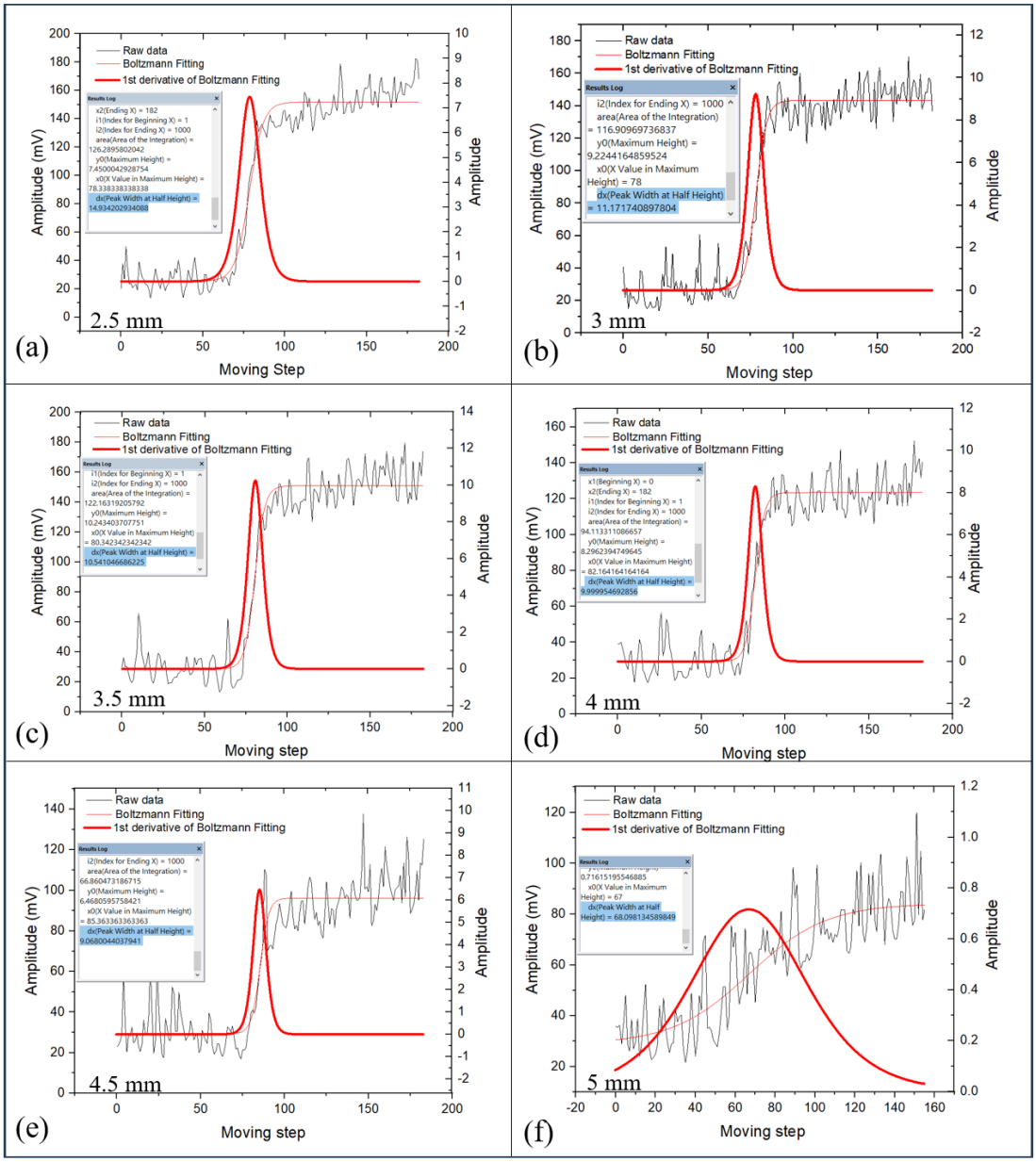

Figure 4.7 Resolution results of the probe at different depths, including the raw data and LPF and the calculated FWHM.

Table 4.1 Resolution results of GI-PAE catheter at different depths.

Imaging depth (mm)	2.5	3	3.5	4	4.5	5
Resolution (μm)	29.8	22.3	21.1	20.0	18.1	136.2

4.2.3 Imaging Result

A stainless-steel bookmark coated with red paint is applied as the phantom for

evaluating the imaging performance of the coaxial GI-PAE catheter. A laser with a wavelength of 532 nm and an energy output of 2 μJ is utilized to generate PA signals. The signals are amplified (39 dB) in the pulser/receiver (5073PR, Olympus, Japan) and then digitized with a DAQ board (ATS9371, Alazar Tech, Canada). The imaging system is similar to that of IV-PAE, as shown in Figure 2.7.

Figures 4.8(a), (b) and (c) display the PA images of the bookmark at different depths. Figure 4.8(a) shows the highest amplitude of the PA signal. As the depth increases, the PA signal diminished gradually. Figure 4.8(c) is processed by 10 times averaging for denization. The blue arrows point out the shadows in the images, which is attributed to the rough surface of the bookmark. All the images are seen with a similar resolution within the same field of view, showing the good performance of the Bessel beam emitted from the coaxial GI-PAE catheter.

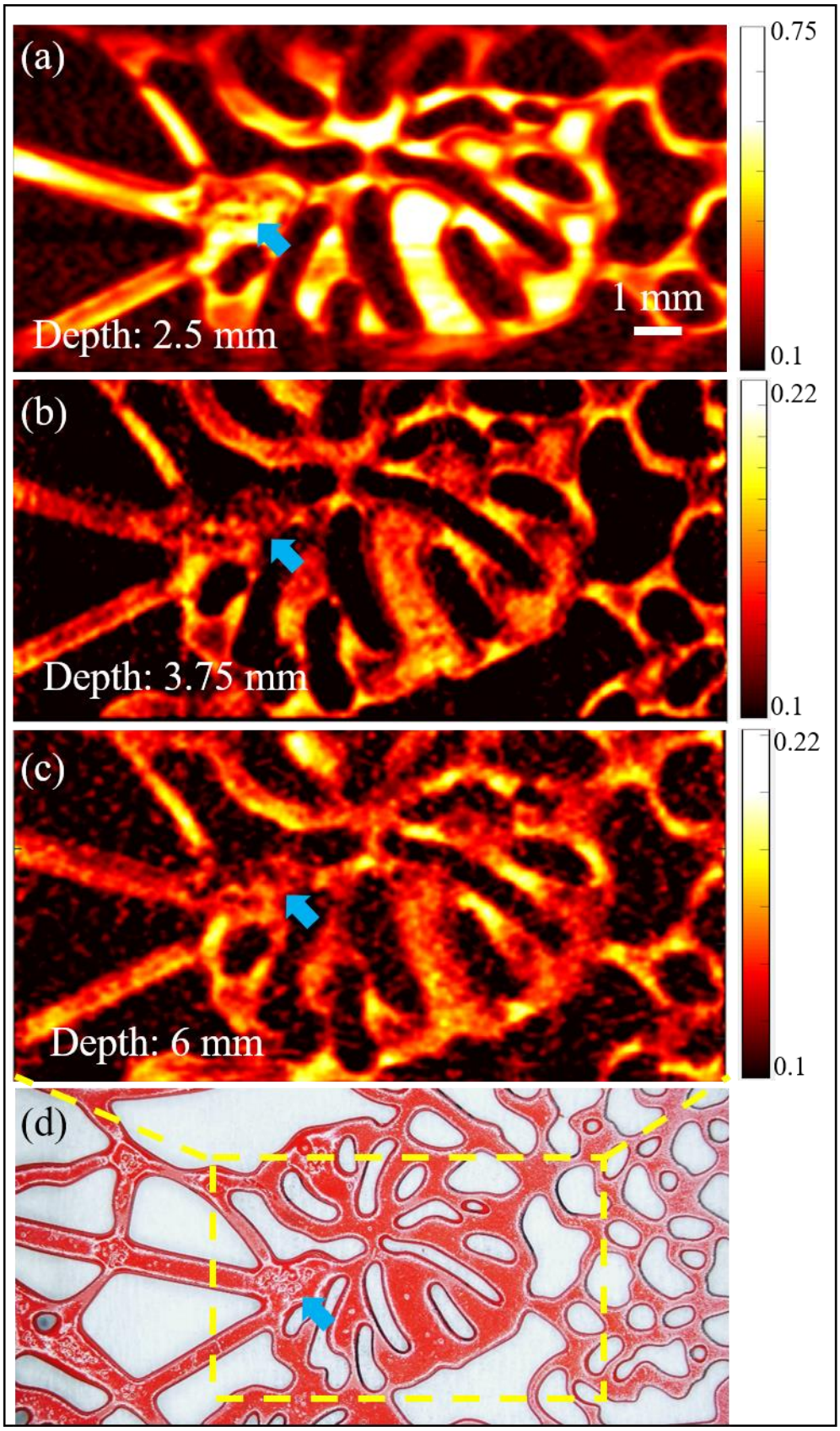

Figure 4.8 PA images and photo of a stainless-steel bookmark. (a, b, c) PA images of the bookmark at different imaging depths, respectively. The unit of the color bar is milli-volt (mV); (d) Photo of the bookmark. The blue arrows indicate the irregular surface of the bookmark.

To further demonstrate the imaging extent and rotation capability of the coaxial GI-PAE catheter, 20 μm-diameter tungsten wires were used for imaging. The tungsten wires were bonded on a self-designed 3D-printed holder distributing at 1mm depth intervals.

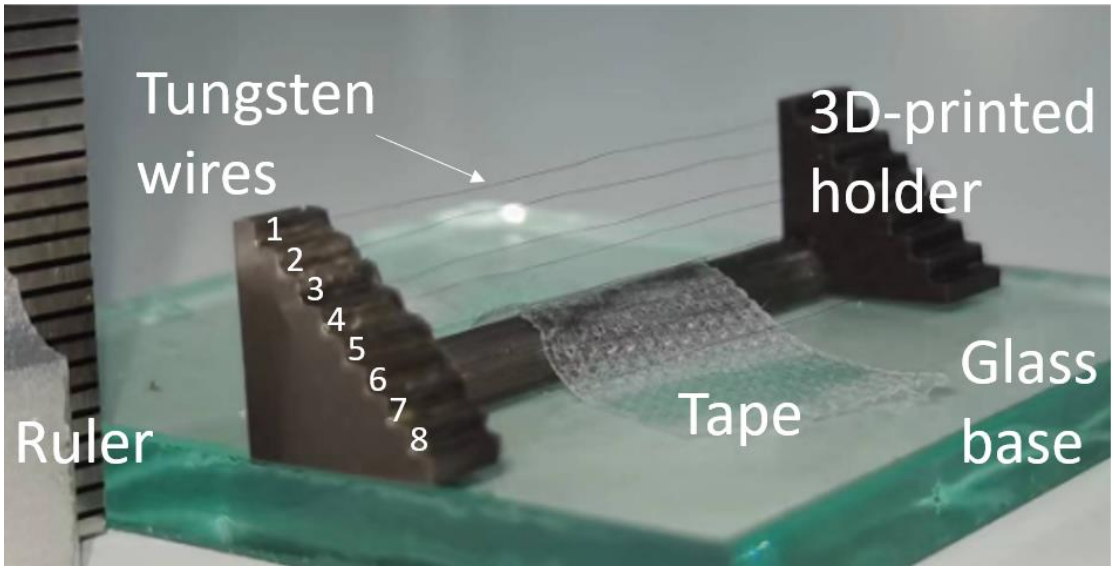

Figure 4.9 The 20 μm-diameter tungsten wires were distributed on the 3D-printed holder.

The imaging experiment was conducted in a water tank. Figure 4.10(a) shows the Bessel beam path irradiated by the catheter in water. The non-diffracting beam can be clear seen from the spot on the wall of the water tank. Figure 4.10(b) presents the photo of the experiment setup with a phantom attached with tungsten wires at different positions. Figure 4.10(c) exhibits the PA imaging result of tungsten wires, verifying an imaging extent of ~6 mm. The PA signal of the second wire is weak due to the distortion of the wire.

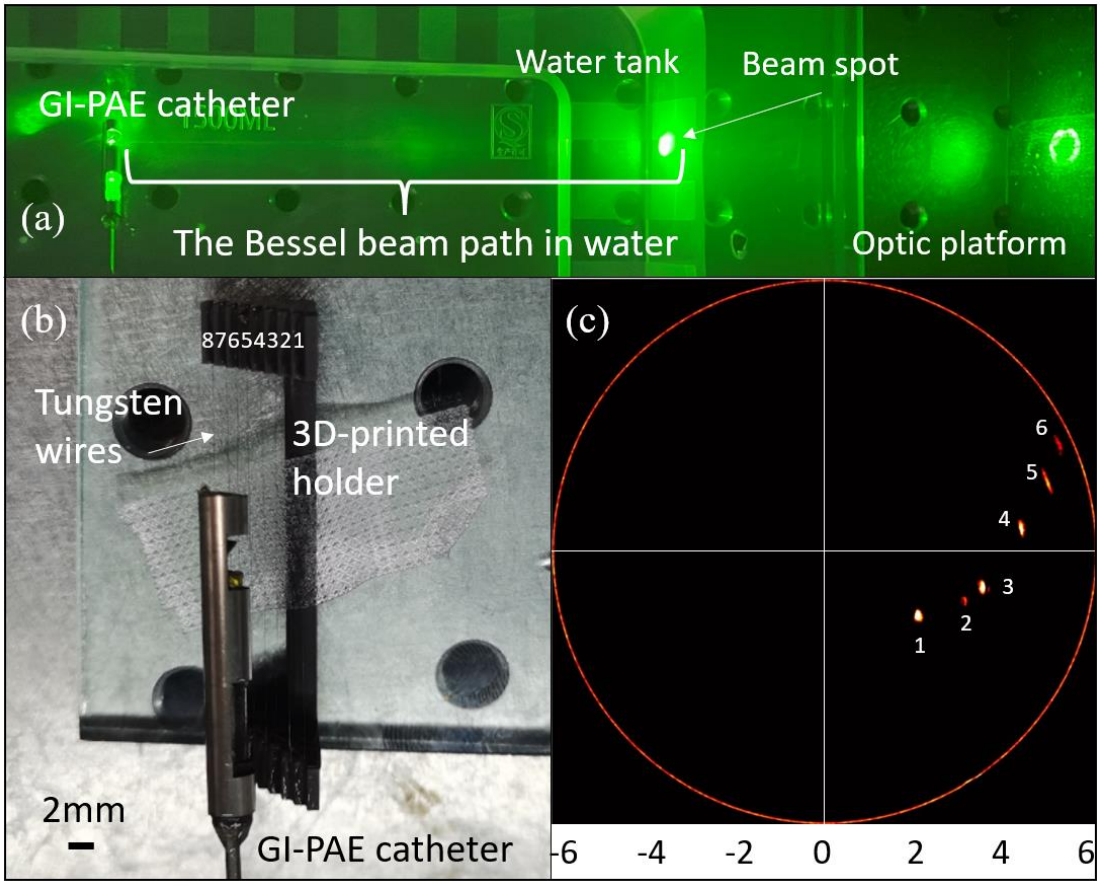

Figure 4. 10 Photos and imaging results of wire phantom. (a) Photo of a GI-PAE catheter with a long diffraction-free laser beam; (b) Photo of tungsten wires attached on a 3D-printed holder; (c) PA images of tungsten wires by the GI-PAE catheter.

4.3 Discussions and Conclusion

In recent years, PAE catheters have shown the potential for imaging the vascular morphology with high resolution in the GI tract, offering invaluable information for early diagnosis of tumor development. However, most of the designs used the Gaussian-like laser beams, which has a limited imaging DOF. In this work, we propose a novel coaxial GI-PAE catheter based on TUST and Bessel beam, offering an extended DOF with a miniature dimension.

Chapter 2 presents a PZT-based ring-shaped UST, demonstrating its performance in the coaxial PAE catheter. However, this kind of opaque USTs cannot be applied to the GI-PAE catheter. The long imaging DOF achieved by the GI-PAE catheter is attributed to the utilization of Bessel beams. The Bessel beam requires a large optical window to maintain its characteristic patten. The tiny orifice of the ring-shaped UST would hinder the transmission of the Bessel beam ripple, changing the Bessel beam patten.

The blade-edge method is conducted to test the imaging resolution as shown in Figure 4.6, showing the results in Figure 4.7. It should be noted that the Bessel beam has a long non-diffraction patten over a large distance in both simulation (Figure 4.2) and practical spot test (Figure 4.3). However, the PA resolution deteriorates to 136.2 μm at the depth of 5 mm due to the signal attenuation with distance. In addition, to ensure the optical transmission efficiency, the TUST was designed without matching and backing layers, which certainly compromises its ultrasound collection performance.

We compared the performance of the proposed GI-PAE with previous works as summarized in Table 4.2. The comparisons show the strengths of the proposed GI-PAE catheter in terms of maximal diameter, flexibility, resolution, and range of DOF. In addition, the LN wafer is a lead-free material, which has higher biocompatibility compared to the conventional piezoelectric materials such as PZT.

Table 4.2 Comparison of GI-PAE parameters in different works.

Application	***Outer diameter* (mm)**	***Flexible***	***Best PA Resolution* (μm)**	***DOF* (mm)**	**Enter instrument channel**	***UST material***	***Reference***
GI tract	8.0	No	~40	8.6	No	PZT	[84]
GI tract	3.38	Yes	~13	< 0.5	Yes	PZT	[19]
GI tract	3.5	Yes	~18.1	> 4.5	Yes	LN	This work

This study demonstrates the long DOF of the coaxial GI-PAE catheter design, but there is still room to further enhance the performance. First of all, the sensitivity of the TUST needs improvement. Utilization of a better piezoelectric material, such as PMN-PT single crystal or ceramic, can improve the sensitivity of the TUST. Besides, exploring transparent materials such as optical glue and parylene for matching layer and backing layer of TUST may also help enhancing its performance. Secondly, to improve the flexibility, the long rigid length of the catheter should be shortened by optimizing the dimensions of the GRIN lens and axicon lens. This can be achieved through upgrading the processing technology on the axicon lens to prepare smaller GRIN lens. Last but not least, *in-vivo* imaging will be conducted to further demonstrate the performance of the proposed catheter.

In conclusion, a novel coaxial GI-PAE catheter based on Bessel beam and a LN-based TUST was developed, offering a long DOF of up to 4.5 mm. With the diameter of 3.5 mm, the proposed catheter enables integration with a 3.7-mm instrumental channel of a conventional clinical optical endoscope. The resolutions of the GI-PAE catheter were ~29.8 μm to ~18.1 μm from 2.5 mm to 4.5 mm, showing its long imaging DOF of ~4.5

mm. The phantom, a stainless-steel bookmark, was imaged at different depths to demonstrate the performance of the GI-PAE catheter in a large imaging range. The catheter scanned the 20 μm-diameter tungsten wires in water, exhibiting its rotation capability and imaging extent as ~6 mm.

Chapter 5 Conclusion and Future Work

5.1 Conclusion

As an emerging technology, PAE has proven its potential in IV and GI imaging, providing high sensitivity and spatial resolution of morphological information. It is crucial to improve the imaging efficiency of PAE catheters. However, most of the reported PAE catheters used oblique detection and side-illumination, or oblique illumination and side-view detection, leading to a limited overlap area for imaging. This study aims to broaden the imaging range of PAE catheters and improve the PAE imaging efficiency, offering innovative coaxial designs for both IV-PAE and GI-PAE, which have great potential for clinical detection capabilities of both atherosclerosis and GI tumors. The main works and contributions are summarized as follows:

Firstly, an IV-PAE catheter with coaxial excitation and detection was developed in this work. Based on the conventional piezoelectric material (PZT), the miniature ring-shaped UST was successfully fabricated using laser micromachining. To integrate the optical and acoustic components coaxially, a fiber was inserted into the center orifice of the ring-shaped UST. The tungsten wire phantom imaging results suggested that the proposed coaxial catheter is capable of detecting the targets in a longer distance, despite experiencing lower optical fluence compared to non-coaxial designs. The *ex-vivo* imaging results further supported the finding, demonstrating the significantly improved imaging depth of the coaxial catheter compared to the non-coaxial counterpart.

Secondly, a TUST was studied and developed for the preparation of designing a coaxial GI-PAE catheter. To investigate the PAI performance of the TUST, a miniature PA probe was successfully designed and fabricated using a 2 mm × 2 mm LN wafer. The dimensions of this PA probe were smaller than the reported LN-based TUSTs. For the first time, a GRIN lens was applied as the backing layer of the TUST, effectively reducing the overall probe size. The proposed probe was with a high center frequency of 46.9 MHz and a -6 dB bandwidth of 29.4%. Experiments were further conducted on phantoms to demonstrate the potential applications in the fluid flow sensing and PA imaging, respectively.

Finally, a coaxial GI-PAE catheter incorporating Bessel beam and TUST was developed. With a non-diffraction Bessel beam formed by a cone lens and a GRIN lens, the catheter offers an extended DOF up to millimeter level. The Bessel beam was evaluated by a CCD camera, showing a steady energy in a long distance. The Bessel beam patten can be seen clearly in the camera screen. A LN-based TUST assembled with a 3 mm-diameter copper tube was applied for ultrasound detection, which allows the coaxial transmission of Bessel beam in the catheter. With a 3.5mm-diameter stainless steel housing, the catheter is flexible and compatible with the 3.7-mm instrumental channel of a clinical optical endoscope. The resolution of the GI-PAE catheter was evaluated by the blade-edge method at different depths, showing its long imaging DOF of ~4.5 mm. The phantoms, including a stainless-steel bookmark and tungsten wires, were both imaged at different depths to demonstrate the performance of the GI-PAE catheter in a

large imaging range of ~6 mm.

In conclusion, this thesis presents the development of novel miniature PAE catheters featuring a coaxial design, significantly expanding the imaging range of PAE beyond previous designs. For the IV-PAE, the proposed catheter based on a ring-shaped UST demonstrates the ability to image nanoprobes in the adventitia of vessels. This novel design enables the detection of inflammation cells from the intima to adventitia of the cardio artery, which is unachievable with the previous designs.

In the context of coaxial miniature PA probe based on the LN single crystal-based TUST, it has the smallest dimensions and highest ultrasound frequency compared to the current research. The proposed PA probe demonstrates its performance in both fluid flow sensing detection and phantom imaging, which has great potential for wearable devices and portable setups.

The novel GI-PAE catheter, designed based on the TUST and Bessel beam, offering a millimeter-lever imaging range with high resolution. Comparing with peer technologies, this coaxial catheter excels in maximal diameter, flexibility, resolution, and range of DOF simultaneously.

Both coaxial PAE catheters in this study have shown their excellent performance in large imaging ranges on both IV and GI applications, getting closer to clinical

implementation.

5.2 Future Work

5.2.1 A Forward-looking Coaxial Catheter Based on Ring-shaped Ultrasound Transducer (UST)

In this study, a ring-shaped UST is developed and applied in the coaxial IV-PAE catheter, offering a large imaging range up to the vessel adventitia. Almost all the reported works focus on the detection of atherosclerosis plaque in the artery wall, providing a side-view imaging. As the plaque grows, it causes serious stenosis in the artery, leading to heart disease. When the plaque ruptures, the thrombus is formed in the artery. If the thrombus does not completely obstruct blood flow in the artery at once, it gradually enlarges and leads to the development of chronic total occlusion (CTO). The current side-view PAE catheter cannot detect the plaque in the serious stenosis or the CTO because the lesional area is in front of the catheter. To overcome the limitation, a forward-looking PAE catheter (shown in Figure 5.1) will be designed and fabricated using the ring-shaped UST. The detection angle would be carefully investigated to confirm the optimal imaging area, providing more useful information regarding the vessel and its pathology.

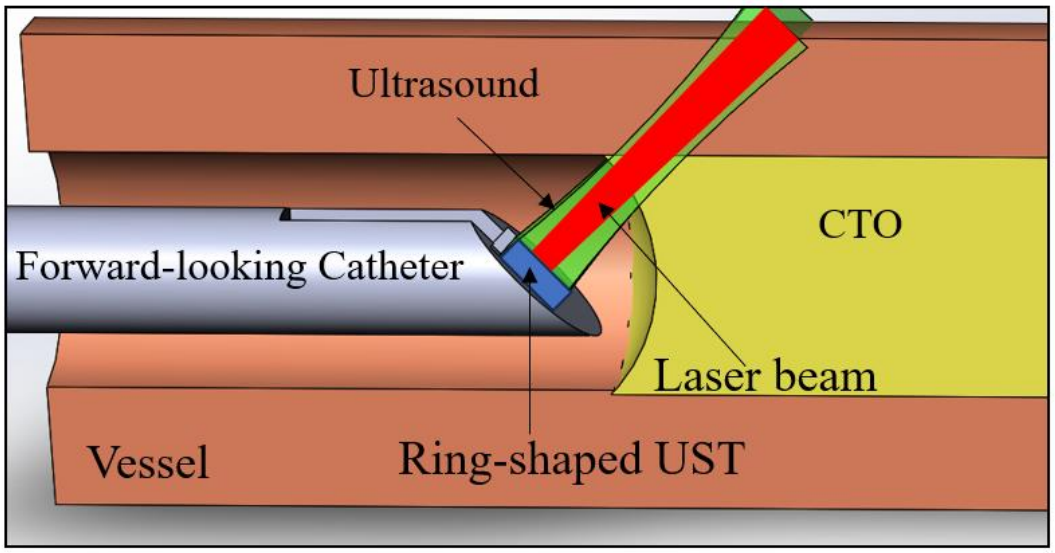

Figure 5.1 Schematic of potential design of a forward-looking catheter fabricated using ring-shaped UST.

5.2.2 A Forward-looking Catheter Based on Fiber Bundle and Transparent ultrasound transducer (TUST)

Unlike the esophagus and colorectum, the special shape of stomach poses challenges for imaging using the current PAE catheters. Those catheters often provides side-view and single-point detection with 360° rotation scanning, which cannot effectively detect all the inner wall of the stomach. A forward-looking catheter is a promising solution to overcome this challenge.

In this study, a miniature PA probe based on TUST and single-mode fiber is designed for multi-functional applications. However, its imaging speed of this probe is limited by the single fiber configuration. To upgrade the imaging rate, a fiber bundle (shown in Figure 5.2) could be implemented to offer optical scanning, greatly speeding up the endoscopic imaging process. The TUST based on LN is used to detect PA/US signals.

In addition, the probe is assembled as a flexible catheter, which is easy to operate and directly contact with the surface of the stomach for imaging.

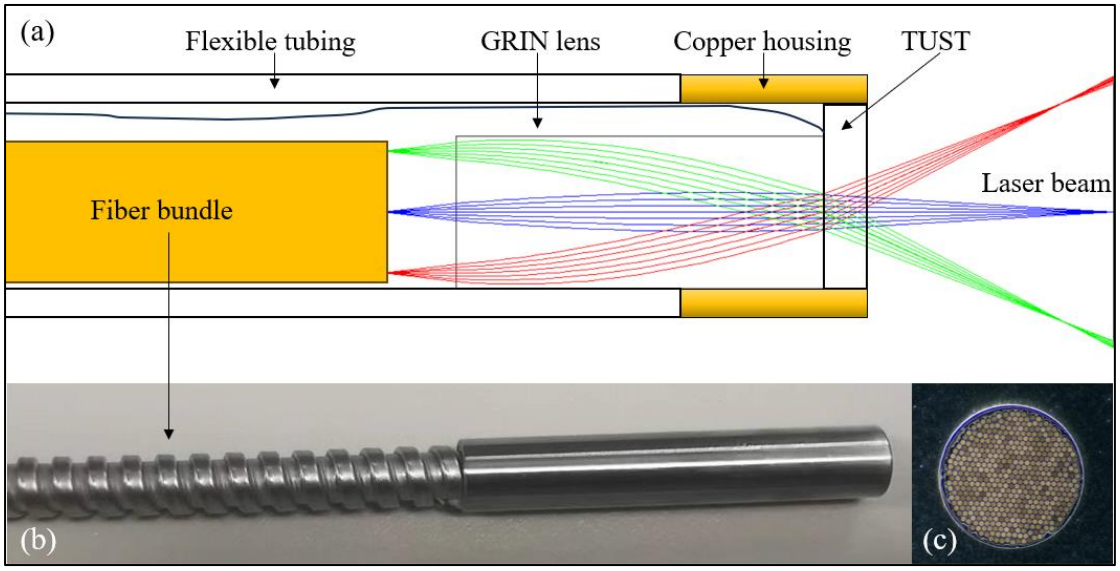

Figure 5.2 A Forward-looking catheter based on the fiber bundle. (a) Schematic of the catheter design; (b) Photo of the fiber bundle; (c) Top view of the fiber bundle.

5.2.3 A Forward-looking Catheter Based on 2D-PZT Scanning

In this study, the coaxial catheters are designed for IV or GI endoscopic applications. To expand the applications, the PA catheters would be used to examine the intrauterine mucosa vessel. While the miniature side-view PA catheter is able to detect the cervix within the endocervical canal, challenges persist in detecting the mucosa of the fundus. In the future, a forward-looking PA catheter (presented in Figure 5.3) will be designed based on the 2D PZT bender and TUST to address the issue. The 2D PZT bender facilitates the movement control of a bare fiber, providing a fast scanning in a miniature housing. With a ball lens at the tip, the bare fiber delivers and focuses the laser beam. The laser beam travels through a TUST to irradiate the tissue in the front of probe.

Subsequently, the TUST collects all the PA signals for image reconstruction. The entire catheter is compact enough to access the uterus and image the vessel at the fundus.

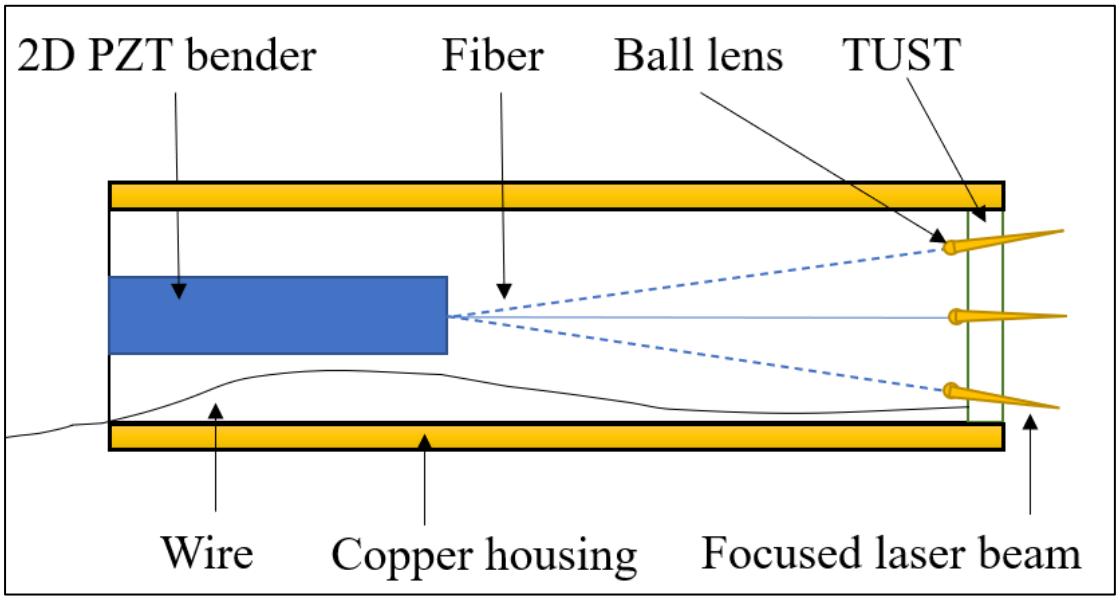

Figure 5.3 Schematic of potential design of a forward-looking catheter based on 2D PZT bender scanning.

References

1. Berci G, Forde KA. History of endoscopy: what lessons have we learned from the past? **Surg Endosc 2000**, 14(1)**:** 5-15.
2. Valdastri P, Simi M, Webster RJ, 3rd. Advanced technologies for gastrointestinal endoscopy. **Annu Rev Biomed Eng 2012**, 14**:** 397-429.
3. Nissen SE, Yock P. Intravascular ultrasound: novel pathophysiological insights and current clinical applications. **Circulation 2001**, 103(4)**:** 604-616.
4. Tao G, Xing-Hua L, Ai-Ming Y, Wei-Xun Z, Fang Y, Xi W*, et al.* Enhanced magnifying endoscopy for differential diagnosis of superficial gastric lesions identified with white-light endoscopy. **Gastric Cancer 2014**, 17(1)**:** 122-129.
5. Barbeiro S, Libanio D, Castro R, Dinis-Ribeiro M, Pimentel-Nunes P. Narrow-Band Imaging: Clinical Application in Gastrointestinal Endoscopy. **GE Port J Gastroenterol 2018**, 26(1)**:** 40-53.
6. Stepp H, Sroka R, Baumgartner R. Fluorescence endoscopy of gastrointestinal diseases: basic principles, techniques, and clinical experience. **Endoscopy 1998**, 30(4)**:** 379-386.
7. Mavadia-Shukla J, Fathi P, Liang WX, Wu SG, Sears C, Li XD. High-speed, ultrahigh-resolution distal scanning OCT endoscopy at 800 nm for in vivo imaging of colon tumorigenesis on murine models. **Biomedical optics express 2018**, 9(8)**:** 3731-3739.
8. Rösch T, Lorenz R, Braig C, Feuerbach S, Siewert JR, Schusdziarra V*, et al.*

Endoscopic ultrasound in pancreatic tumor diagnosis. **1991**, 37(3)**:** 347-352.

9. Byrne MF, Jowell PS. Gastrointestinal imaging: endoscopic ultrasound. **Gastroenterology 2002**, 122(6)**:** 1631-1648.

10. Liu M, Chen Z, Zabihian B, Sinz C, Zhang E, Beard PC*, et al.* Combined multi-modal photoacoustic tomography, optical coherence tomography (OCT) and OCT angiography system with an articulated probe for in vivo human skin structure and vasculature imaging. **2016**, 7(9)**:** 3390-3402.

11. Li Y, Lin RQ, Liu CB, Chen JH, Liu HD, Zheng RQ*, et al.* In vivo photoacoustic/ultrasonic dual-modality endoscopy with a miniaturized full field-of-view catheter. **Journal of Biophotonics 2018**, 11(10)**:** e201800034.

12. Kircher MF, de la Zerda A, Jokerst JV, Zavaleta CL, Kempen PJ, Mittra E*, et al.* A brain tumor molecular imaging strategy using a new triple-modality MRI-photoacoustic-Raman nanoparticle. **Nat Med 2012**, 18(5)**:** 829-834.

13. Li Y, Lu G, Zhou Q, Chen Z. Advances in Endoscopic Photoacoustic Imaging. **Photonics 2021**, 8(7).

14. Jansen K, Wu M, van der Steen AF, van Soest G. Lipid detection in atherosclerotic human coronaries by spectroscopic intravascular photoacoustic imaging. **Opt Express 2013**, 21(18)**:** 21472-21484.

15. Jansen K, van Soest G, van der Steen AF. Intravascular photoacoustic imaging: a new tool for vulnerable plaque identification. **Ultrasound Med Biol 2014**, 40(6)**:** 1037-1048.

16. Jansen K, Wu M, van der Steen AF, van Soest G. Photoacoustic imaging of

human coronary atherosclerosis in two spectral bands. **Photoacoustics 2014**, 2(1)**:** 12-20.

17. Yang JM, Favazza C, Chen R, Yao J, Cai X, Maslov K*, et al.* Simultaneous functional photoacoustic and ultrasonic endoscopy of internal organs in vivo. **Nat Med 2012**, 18(8)**:** 1297-1302.

18. Yang JM, Li C, Chen R, Rao B, Yao J, Yeh CH*, et al.* Optical-resolution photoacoustic endomicroscopy in vivo. **Biomedical optics express 2015**, 6(3)**:** 918-932.

19. Kim M, Lee KW, Kim K, Gulenko O, Lee C, Keum B*, et al.* Intra-instrument channel workable, optical-resolution photoacoustic and ultrasonic mini-probe system for gastrointestinal endoscopy. **Photoacoustics 2022**, 26**:** 100346.

20. Bai XS, Gong XJ, Hau W, Lin RQ, Zheng JX, Liu CB*, et al.* Intravascular Optical-Resolution Photoacoustic Tomography with a 1.1 mm Diameter Catheter. **Plos One 2014**, 9(3)**:** e92463.

21. Piao Z, Ma T, Li J, Wiedmann MT, Huang S, Yu M*, et al.* High speed intravascular photoacoustic imaging with fast optical parametric oscillator laser at 1.7 μm. **2015**, 107(8).

22. Beard P. Biomedical photoacoustic imaging. **Interface Focus 2011**, 1(4)**:** 602-631.

23. Wang LV, Yao J. A practical guide to photoacoustic tomography in the life sciences. **Nat Methods 2016**, 13(8)**:** 627-638.

24. Xia J, Yao J, Wang LV. Photoacoustic tomography: principles and advances.

Electromagn Waves (Camb) 2014, 147**:** 1-22.

25. Xu MH, Wang LHV. Photoacoustic imaging in biomedicine. **Review of Scientific Instruments 2006**, 77(4).

26. Zhang C, Maslov K, Hu S, Chen R, Zhou Q, Shung KK*, et al.* Reflection-mode submicron-resolution in vivo photoacoustic microscopy. **J Biomed Opt 2012**, 17(2)**:** 020501.

27. Wang LV. Multiscale photoacoustic microscopy and computed tomography. **Nat Photonics 2009**, 3(9)**:** 503-509.

28. Yang X, Stein EW, Ashkenazi S, Wang LV. Nanoparticles for photoacoustic imaging. **Wiley Interdiscip Rev Nanomed Nanobiotechnol 2009**, 1(4)**:** 360-368.

29. Xia J, Wang LV. Small-animal whole-body photoacoustic tomography: a review. **IEEE Trans Biomed Eng 2014**, 61(5)**:** 1380-1389.

30. Zhou YY, Liang SY, Li MS, Liu CB, Lai PX, Wang LD. Optical-resolution photoacoustic microscopy with ultrafast dual-wavelength excitation. **Journal of Biophotonics 2020**, 13(6)**:** e201960229.

31. Wang P, Ma T, Slipchenko MN, Liang S, Hui J, Shung KK*, et al.* High-speed intravascular photoacoustic imaging of lipid-laden atherosclerotic plaque enabled by a 2-kHz barium nitrite raman laser. **Scientific reports 2014**, 4(1)**:** 6889.

32. Choi SSS, Mandelis A. Review of the state of the art in cardiovascular endoscopy imaging of atherosclerosis using photoacoustic techniques with

pulsed and continuous-wave optical excitations. **J Biomed Opt 2019**, 24(8)**:** 1-15.

33. Zhang HF, Maslov K, Sivaramakrishnan M, Stoica G, Wang LHV. Imaging of hemoglobin oxygen saturation variations in single vessels in vivo using photoacoustic microscopy. **Applied Physics Letters 2007**, 90(5).

34. Hu S, Maslov K, Wang LV. Second-generation optical-resolution photoacoustic microscopy with improved sensitivity and speed. **Opt Lett 2011**, 36(7)**:** 1134-1136.

35. Li M, Chen J, Wang L. High acoustic numerical aperture photoacoustic microscopy with improved sensitivity. **Opt Lett 2020**, 45(3)**:** 628-631.

36. Wang L, Zhang C, Wang LV. Grueneisen relaxation photoacoustic microscopy. **Phys Rev Lett 2014**, 113(17)**:** 174301.

37. Lai P, Wang L, Tay JW, Wang LV. Photoacoustically guided wavefront shaping for enhanced optical focusing in scattering media. **Nat Photonics 2015**, 9(2)**:** 126-132.

38. Shi J, Wong TTW, He Y, Li L, Zhang R, Yung CS*, et al.* High-resolution, high-contrast mid-infrared imaging of fresh biological samples with ultraviolet-localized photoacoustic microscopy. **Nat Photonics 2019**, 13**:** 609-615.

39. Li Y, Lu G, Chen JJ, Jing JC, Huo T, Chen R*, et al.* PMN-PT/Epoxy 1-3 composite based ultrasonic transducer for dual-modality photoacoustic and ultrasound endoscopy. **Photoacoustics 2019**, 15**:** 100138.

40. Wang LV, Wu H-i. *Biomedical optics: principles and imaging*. John Wiley &

Sons, **2012**.

41. Vienneau E, Liu W, Yao J. Dual-view acoustic-resolution photoacoustic microscopy with enhanced resolution isotropy. **Opt Lett 2018**, 43(18)**:** 4413-4416.

42. Schwarz M, Buehler A, Ntziachristos V. Isotropic high resolution optoacoustic imaging with linear detector arrays in bi-directional scanning. **Journal of Biophotonics 2015**, 8(1-2)**:** 60-70.

43. Vallet M, Varray F, Boutet J, Dinten JM, Caliano G, Savoia AS*, et al.* Quantitative comparison of PZT and CMUT probes for photoacoustic imaging: Experimental validation. **Photoacoustics 2017**, 8**:** 48-58.

44. Chen H, Mirg S, Osman M, Agrawal S, Cai J, Biskowitz R*, et al.* A High Sensitivity Transparent Ultrasound Transducer based on PMN-PT for Ultrasound and Photoacoustic Imaging. **IEEE Sens Lett 2021**, 5(11)**:** 1-4.

45. Fatima A, Kratkiewicz K, Manwar R, Zafar M, Zhang R, Huang B*, et al.* Review of cost reduction methods in photoacoustic computed tomography. **Photoacoustics 2019**, 15**:** 100137.

46. Lin L, Hu P, Shi J, Appleton CM, Maslov K, Li L*, et al.* Single-breath-hold photoacoustic computed tomography of the breast. **Nat Commun 2018**, 9(1)**:** 2352.

47. Lemaster JE, Jokerst JVJWIRN, Nanobiotechnology. What is new in nanoparticle‐based photoacoustic imaging? **2017**, 9(1)**:** e1404.

48. Pu KY, Shuhendler AJ, Jokerst JV, Mei JG, Gambhir SS, Bao ZN*, et al.*

Semiconducting polymer nanoparticles as photoacoustic molecular imaging probes in living mice. **Nature Nanotechnology 2014**, 9(3)**:** 233-239.

49. Wu C, Zhang Y, Li Z, Li C, Wang QJN. A novel photoacoustic nanoprobe of ICG@ PEG-Ag 2 S for atherosclerosis targeting and imaging in vivo. **2016**, 8(25)**:** 12531-12539.

50. Jing L, Liang X, Deng Z, Feng S, Li X, Huang M*, et al.* Prussian blue coated gold nanoparticles for simultaneous photoacoustic/CT bimodal imaging and photothermal ablation of cancer. **Biomaterials 2014**, 35(22)**:** 5814-5821.

51. Kim T, Lemaster JE, Chen F, Li J, Jokerst JVJAn. Photoacoustic imaging of human mesenchymal stem cells labeled with Prussian blue–poly (l-lysine) nanocomplexes. **ACS nano 2017**, 11(9)**:** 9022-9032.

52. Yang W, Guo W, Le W, Lv G, Zhang F, Shi L*, et al.* Albumin-Bioinspired Gd:CuS Nanotheranostic Agent for In Vivo Photoacoustic/Magnetic Resonance Imaging-Guided Tumor-Targeted Photothermal Therapy. **ACS Nano 2016**, 10(11)**:** 10245-10257.

53. Zhang Q, Iwakuma N, Sharma P, Moudgil BM, Wu C, McNeill J*, et al.* Gold nanoparticles as a contrast agent for in vivo tumor imaging with photoacoustic tomography. **Nanotechnology 2009**, 20(39)**:** 395102.

54. Duan T, Peng X, Chen M, Zhang D, Gao F, Yao J. Detection of weak optical absorption by optical-resolution photoacoustic microscopy. **Photoacoustics 2022**, 25**:** 100335.

55. Yang JM, Maslov K, Yang HC, Zhou Q, Shung KK, Wang LV. Photoacoustic

endoscopy. **Opt Lett 2009**, 34(10)**:** 1591-1593.

56. Rosencwaig A. Photoacoustic spectroscopy. **Annu Rev Biophys Bioeng 1980**, 9(1)**:** 31-54.

57. Cox BT, Arridge SR, Beard PC. Estimating chromophore distributions from multiwavelength photoacoustic images. **J Opt Soc Am A Opt Image Sci Vis 2009**, 26(2)**:** 443-455.

58. Libby P. Inflammation in atherosclerosis. **Arterioscler Thromb Vasc Biol 2012**, 32(9)**:** 2045-2051.

59. Wang B, Karpiouk A, Yeager D, Amirian J, Litovsky S, Smalling R*, et al.* Intravascular photoacoustic imaging of lipid in atherosclerotic plaques in the presence of luminal blood. **Opt Lett 2012**, 37(7)**:** 1244-1246.

60. Wang B, Su JL, Karpiouk AB, Sokolov KV, Smalling RW, Emelianov SYJIJostiQE. Intravascular photoacoustic imaging. **2010**, 16(3)**:** 588-599.

61. Maslov K, Stoica G, Wang LV. In vivo dark-field reflection-mode photoacoustic microscopy. **Opt Lett 2005**, 30(6)**:** 625-627.

62. Maslov K, Zhang HF, Hu S, Wang LVJOl. Optical-resolution photoacoustic microscopy for in vivo imaging of single capillaries. **2008**, 33(9)**:** 929-931.

63. Sun M, Li C, Chen N, Zhao H, Ma L, Liu C*, et al.* Full three-dimensional segmentation and quantification of tumor vessels for photoacoustic images. **Photoacoustics 2020**, 20**:** 100212.

64. Gistera A, Hansson GK. The immunology of atherosclerosis. **Nature Reviews Nephrology 2017**, 13(6)**:** 368-380.

65. Geovanini GR, Libby P. Atherosclerosis and inflammation: overview and updates. **Clin Sci (Lond) 2018**, 132(12)**:** 1243-1252.

66. Bo W, Su JL, Amirian J, Litovsky SH, Emelianov SJOE. Detection of lipid in atherosclerotic vessels using ultrasound-guided spectroscopic intravascular photoacoustic imaging. **2010**, 18(5)**:** 4889-4897.

67. Bom MJ, Van Der Heijden DJ, Kedhi E, Van Der Heyden J, Meuwissen M, Knaapen P*, et al.* Early detection and treatment of the vulnerable coronary plaque: can we prevent acute coronary syndromes? **Circulation: cardiovascular imaging 2017**, 10(5)**:** e005973.

68. Li Y, Chen Z. Multimodal Intravascular Photoacoustic and Ultrasound Imaging. **Biomed Eng Lett 2018**, 8(2)**:** 193-201.

69. Stefanadis C, Antoniou CK, Tsiachris D, Pietri P. Coronary Atherosclerotic Vulnerable Plaque: Current Perspectives. **J Am Heart Assoc 2017**, 6(3)**:** e005543.

70. Liu Y, Liang C, Liu X, Liao B, Pan X, Ren Y*, et al.* AGEs increased migration and inflammatory responses of adventitial fibroblasts via RAGE, MAPK and NF-κB pathways. **2010**, 208(1)**:** 34-42.

71. Milutinovi A, Duan U, Zorc-Pleskovi RJBJoBMS. Pathogenesis of atherosclerosis in the tunica intima, media, and adventitia of coronary arteries: An updated review. **2020**, 20(1).

72. Akhavanpoor M, Gleissner CA, Akhavanpoor H, Lasitschka F, Doesch AO, Katus HA*, et al.* Adventitial tertiary lymphoid organ classification in human

atherosclerosis. **Cardiovasc Pathol 2018**, 32**:** 8-14.

73. Mohanta SK, Peng L, Li Y, Lu S, Sun T, Carnevale L*, et al.* Neuroimmune cardiovascular interfaces control atherosclerosis. **Nature 2022**, 605(7908)**:** 152-159.

74. Cao Y, Kole A, Hui J, Zhang Y, Mai J, Alloosh M*, et al.* Fast assessment of lipid content in arteries in vivo by intravascular photoacoustic tomography. **Scientific reports 2018**, 8(1)**:** 2400.

75. Iskander-Rizk S, Wu M, Springeling G, van Beusekom HMM, Mastik F, Te Lintel Hekkert M*, et al.* In vivo intravascular photoacoustic imaging of plaque lipid in coronary atherosclerosis. **EuroIntervention 2019**, 15(5)**:** 452-456.

76. Wei W, Li X, Zhou Q, Shung KK, Chen Z. Integrated ultrasound and photoacoustic probe for co-registered intravascular imaging. **J Biomed Opt 2011**, 16(10)**:** 106001.

77. Xiao J, Li Y, Jin W, Peng K, Zhu Z, Wang B. Photoacoustic endoscopy with hollow structured lens-focused polyvinylidine fluoride transducer. **Appl Opt 2016**, 55(9)**:** 2301-2305.

78. Hui J, Cao Y, Zhang Y, Kole A, Wang P, Yu G*, et al.* Real-time intravascular photoacoustic-ultrasound imaging of lipid-laden plaque in human coronary artery at 16 frames per second. **Scientific reports 2017**, 7(1)**:** 1417.

79. Cao Y, Hui J, Kole A, Wang P, Yu Q, Chen W*, et al.* High-sensitivity intravascular photoacoustic imaging of lipid–laden plaque with a collinear catheter design. **Scientific reports 2016**, 6**:** 25236.

80. Link A, Treiber G, Peters B, Wex T, Malfertheiner P. Impact of endoscopy-based research on quality of life in healthy volunteers. **World journal of gastroenterology 2010**, 16(4)**:** 467-473.

81. Du W, Frankel TL, Green M, Zou W. IFNgamma signaling integrity in colorectal cancer immunity and immunotherapy. **Cellular & molecular immunology 2022**, 19(1)**:** 23-32.

82. Cartana ET, Gheonea DI, Saftoiu A. Advances in endoscopic ultrasound imaging of colorectal diseases. **World journal of gastroenterology 2016**, 22(5)**:** 1756-1766.

83. Chen LY, Wang L, Ren YX, Pang Z, Liu Y, Sun XD*, et al.* The circular RNA circ-ERBIN promotes growth and metastasis of colorectal cancer by miR-125a-5p and miR-138-5p/4EBP-1 mediated cap-independent HIF-1alpha translation. **Molecular cancer 2020**, 19(1)**:** 164.

84. Li XW, Xiong KD, Yang SH. Large-depth-of-field optical-resolution colorectal photoacoustic endoscope. **Applied Physics Letters 2019**, 114(16).

85. Sun H, Wang W, Zhang ZX, Wang L, Zhang WY, Xiong KD*, et al.* Real-time optical-resolution photoacoustic endoscope. **Applied Physics Express 2021**, 14(4)**:** 042012.

86. Wang L, Lei P, Wen X, Zhang P, Yang S. Tapered fiber-based intravascular photoacoustic endoscopy for high-resolution and deep-penetration imaging of lipid-rich plaque. **Opt Express 2019**, 27(9)**:** 12832-12840.

87. Wen X, Lei P, Huang SX, Chen XY, Yuan YC, Ke D*, et al.* High-fluence relay-

based disposable photoacoustic-ultrasonic endoscopy for in vivo anatomical imaging of gastrointestinal tract. **Photon Res 2023**, 11(1)**:** 55-64.

88. Xiong KD, Wang W, Guo T, Yuan Z, Yang SH. Shape-adapting panoramic photoacoustic endomicroscopy. **Optics Letters 2019**, 44(11)**:** 2681-2684.

89. Xiong K, Yang S, Li X, Xing D. Autofocusing optical-resolution photoacoustic endoscopy. **Opt Lett 2018**, 43(8)**:** 1846-1849.

90. Guo Z, Li Y, Chen SL. Miniature probe for in vivo optical- and acoustic-resolution photoacoustic microscopy. **Opt Lett 2018**, 43(5)**:** 1119-1122.

91. Guo H, Song C, Xie H, Xi L. Photoacoustic endomicroscopy based on a MEMS scanning mirror. **Opt Lett 2017**, 42(22)**:** 4615-4618.

92. MacAlpin RN, Abbasi AS, Grollman JH, Jr., Eber L. Human coronary artery size during life. A cinearteriographic study. **Radiology 1973**, 108(3)**:** 567-576.

93. Chen R, He Y, Shi J, Yung C, Hwang J, Wang LV*, et al.* Transparent high-frequency ultrasonic transducer for photoacoustic microscopy application. **2020**, 67(9)**:** 1848-1853.

94. Ren D, Sun Y, Shi J, Chen R. A review of transparent sensors for photoacoustic imaging applications. Photonics; 2021: MDPI; 2021. p. 324.

95. Park J, Park B, Kim TY, Jung S, Choi WJ, Ahn J*, et al.* Quadruple ultrasound, photoacoustic, optical coherence, and fluorescence fusion imaging with a transparent ultrasound transducer. **2021**, 118(11)**:** e1920879118.

96. Dangi A, Agrawal S, Kothapalli S-RJOl. Lithium niobate-based transparent ultrasound transducers for photoacoustic imaging. **2019**, 44(21)**:** 5326-5329.

97. Park S, Kang S, Chang JHJJoM, Engineering B. Optically transparent focused transducers for combined photoacoustic and ultrasound microscopy. **2020**, 40**:** 707-718.

98. Durnin J. Exact solutions for nondiffracting beams I The scalar theory. **Journal of the Optical Society of America A 1987**, 4(4).

99. Durnin J, Miceli J, Jr., Eberly JH. Diffraction-free beams. **Phys Rev Lett 1987**, 58(15)**:** 1499-1501.

100. Zhu L, Wang J. Arbitrary manipulation of spatial amplitude and phase using phase-only spatial light modulators. **Scientific reports 2014**, 4**:** 7441.